3

A high Galactic latitude HI absorption survey using the GMRT

"Data! Data! Data!" he cried impatiently. "I can’t make bricks without clay."
—Sherlock Holmes, The Adventure of the Copper Beeches

Summary and the main results of chapter 3

Nearby interstellar clouds with larger velocities are identified from optical/UV absorption lines. However, until recently, these features were not detected in HI absorption/emission studies. We have used Giant meterwave radio telescope (GMRT) to measure HI absorption towards 104 extragalactic radio continuum sources located at Galactic latitudes $|b| > 15^{\circ}$. *This is the most sensitive HI absorption survey to date, with an rms of 0.003 in HI optical depth. The primary aim of this survey is to study the kinematics of diffuse interstellar clouds in the solar neighbourhood. The main results are summarized below:*

- ***We detected*** $\sim$***120 absorption features, of these, 13 were at velocities greater than 15 km*** s^{-1}.
- ***We find that the higher velocity absorptions have smaller optical depths.***
- ***The detected HI absorption features do not show pronounced effects of differential Galactic rotation.***
- ***We find the histogram of radial velocities to have two gaussian components, one with a dispersion*** $\sim$***7 km*** s^{-1} ***and the second one with a dispersion*** $\sim$***20 km*** s^{-1}.
- ***While the significance of the wider gaussian component is not clear, it is consistent with the recent discovery of a population of HI clouds in the lower Galactic halo.***

3.1 INTRODUCTION

3.1.1 background

As we discussed in the previous chapter, early optical spectral line observations of Interstellar absorption led to our present understanding of the Interstellar medium. The most famous of such investigations was that by Adams (1949), who obtained the CaII absorption spectra towards 300 O & B stars. This work, as well as the later ones by Münch (1957), Münch & Zirrin (1961), Hobbs (1969), and others, revealed several absorption features in many lines of sight: a group of absorption lines at low velocities ($|v| \lesssim 10$ km s^{-1}) and another at higher velocities ($|v| \gtrsim 10$ km s^{-1}). It was noted that the high velocity components were weaker as compared to the low velocity ones. Blaauw (1952) studied the radial velocity distribution of Interstellar absorption lines from Adams' (1949) data and found evidence for a high velocity tail in the velocity distribution of Interstellar CaII absorption components. Often, stars with calcium lines in their spectra also show neutral sodium in absorption, although they are less in number as compared to the CaII absorption line components. In those cases where the radial velocities of the NaI absorption features coincide with that of the CaII lines, one can assume that they originate in the same cloud. From the observed line strengths one can estimate the NaI or CaII column density along the line of sight, assuming that the lines are unsaturated. An interesting evidence favoring two distinct populations of Interstellar clouds came from Routly & Spitzer (1952). They examined 21 lines of sight towards early type stars and found the ratio of column density of NaI to CaII for a particular cloud to depend on the velocity of the cloud with respect to the local standard of rest. It was found that on an average, clouds with large radial velocities in the LSR frame have lower value for the ratio N$_{NaI}$/N$_{CaII}$. This correlation was later confirmed using a larger sample of 64 stars by Siluk & Silk (1974). The presence of a high velocity tail in the frequency distribution of Interstellar optical absorption line velocities is evident from the data used by Siluk and Silk (Fig. 3.1). Siluk & Silk (1974) explained these large peculiar velocities as associated with supernova remnants in their late phases of evolution. They used a power law fit to the higher velocity part histogram (v $>$ 20 km s^{-1}) of the form:

$$n(v > 20kms^{-1}) = Av^{-\alpha} \tag{3.1}$$

and found the best fit value for α to be 2. For the gas within the supernovae shells, equation 3.1 can be re-written as a function of diameter, D of the expanding shell.

$$n(< D) \propto D^{\beta} \tag{3.2}$$

where n($<$ D) is the number of SNRs with diameter less than D. The number of clouds at velocity above a value "v" was related to the number of SNRs with an expansion velocity greater than "v", which in turn is the number of SNRs younger than age, say "t". In the adiabatic phase of expansion, t $\propto$ D$^{5/2}$. i.e, β = 5/2.

$$N(> V) = N(< D) = N(< t) \tag{3.3}$$

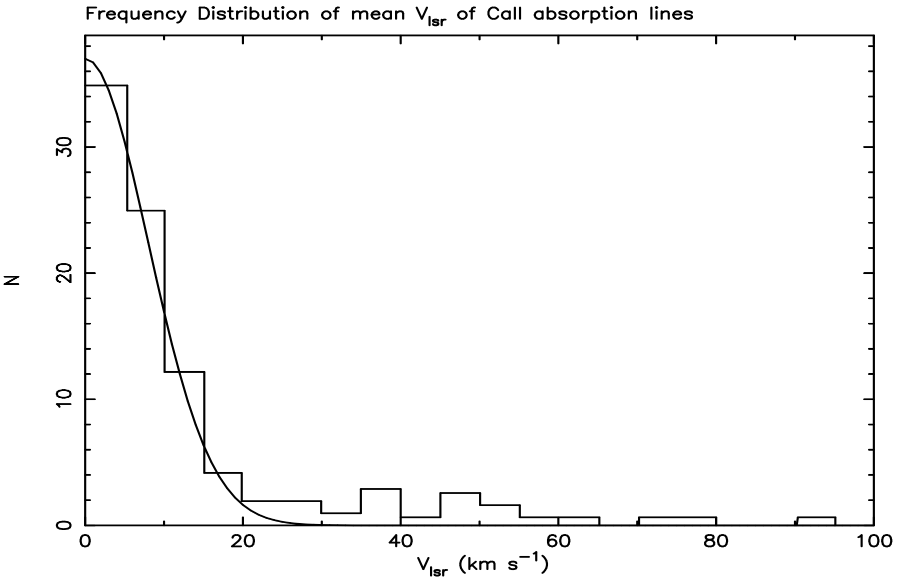

Fig. 3.1 The histogram of radial velocities observed in the direction of 64 stars from the data in Siluk & Silk (1974). The smooth curve is the Gaussian fit to the low velocity features, with σ_v = 8.0 km s^{-1} (from Radhakrishnan & Srinivasan, 1980).

$$N(< t) \propto t \propto D^{5/2} \tag{3.4}$$

In the adiabatic or Sedov phase of expansion, D^{3}V^2 is constant. Hence,

$$V \propto D^{-3/2} \propto D^{1-\beta} \tag{3.5}$$

Using eqns 3.5 and eqn 3.1, one obtains

$$\beta = \frac{\alpha}{\alpha - 1} \tag{3.6}$$

Hence for the best fit value of α, the exponent β = 2. For an adiabatically expanding supernova remnant satisfying Sedov solution, β = 2.5 and a higher value at later phases. However, Siluk & Silk concluded that the fit to their data is satisfactory even for β = 3, *i.e.* α = 3/2 and the distribution of velocities is consistent with the SNR interpretation. Earlier to this work, Spitzer (1956, 1968, 1978) had repeatedly pointed out the importance of supernova explosions in the dynamics of the Interstellar medium. Later, McKee & Ostriker (1977) extended the two-phase model of the Interstellar medium by Field, Goldsmith & Habing (1969) to the three phase model, where the different phases are regulated by supernova explosions.

As we mentioned in the previous chapter, there were several attempts to search for the HI 21cm-line emission from the higher peculiar velocity clouds identified through the optical absorption lines. Interestingly, although the HI emission velocities are clearly correlated with that of optical absorption lines at low random velocities, no HI was detected corresponding to the higher random velocity ($|v| \geq 10$ km s^{-1}) optical absorption lines (Habing 1968, 1969; Goldstein & McDonald, 1969). This seems to be the case in all the directions in the sky. These high random velocity clouds were not detected by the subsequent HI emission surveys either. To explain this discrepancy, Habing (1969) suggested that the fast population of clouds consists of smaller clumps. The relatively larger beam size used for HI emission searches (θ $\approx$ 0.5°) can result in beam dilution to weaken the signal.

However, some radio observations, though controversial, suggests the presence of a population of fast clouds. Radhakrishnan and Sarma (1980) carried out a Gaussian fitting analysis to the HI 21cm-line optical depth profile towards the Galactic Center obtained with the Parkes Interferometer by Radhakrishnan et. al., (1972) and found a wide (σ $\sim$35 km s^{-1}) absorption feature which was attributed to a population of clouds with large velocity dispersion. Support for a high velocity tail also came from an independent study comparing the terminal velocities of HI absorption spectra in the directions of 38 HII regions with their Radio Recombination Line velocities by Anantharamaiah et al. (1984). Kulkarni and Fich (1985) found some evidence for large velocity dispersion HI clouds, but they were more cautious about their filling factor.

Several controversies center around the HI 21cm-line searches for the high velocity tail of the Interstellar cloud population, whose existence is confirmed beyond doubts by the optical studies. Another discrepancy concerns the number of clouds per kiloparsec. The optical estimates for this number always tend to be higher than that inferred from HI studies. Infact, this may be related to the missing HI clouds at higher velocities. **In this context, we would like to mention that our study described in the previous chapter is the first observational evidence for the 21cm line absorption arising in the faster clouds**.

3.1.2 Motivations for the present high latitude survey

It should be clear from the above discussion that the radial velocity distributions of interstellar clouds derived from optical and radio observations are inconsistent with one another. The high velocity tail of the cloud population appears to be absent in the radio surveys. The optical data used by various investigators are mostly towards stars within 1 kpc of the sun. There exists a number of HI emission and a few absorption surveys. The all sky HI emission surveys sample much larger path lengths as compared to the optical absorption studies. Even at higher latitudes, the high velocity cloud complexes and other large scale systematic features in the Galactic halo are sampled by these surveys. Hence, it is not appropriate to compare the radial velocity information from the HI emission surveys with the optical data. For one thing, the cloud distances cannot be estimated from the HI emission data easily. Single dish HI absorption surveys are limited by errors due to the variation of HI emission intensity over angular scales smaller than the telescope beam. Even for the Arecibo telescope, which has the smallest beam of any single dish radio telescope, emission fluctuations dominate the receiver noise as the source of optical depth errors for more than about 10 minutes of integration time at higher Galactic latitudes. In the Galactic plane this effect is much worse because the HI emission has more structure, down to sub arc minute scales, which is clear from the Canadian Galactic plane survey (CGPS - English et. al., 1998; Gibson et al., 2000). Interferometric surveys would appear to be a better alternative. However, very long integration times are required to reach a very low optical depth limits, due to the lack of collecting area of the interferometers. The existing interferometric HI absorption surveys (Radhakrishnan et. al., 1972; Mebold et. al., 1981; Dickey et. al., 1983; and others) are all sensitive only to an extent of detecting optical depth $\gtrsim$ 0.05. Till recently, the VLA used to be the only instrument with a collecting area comparable with large single dish telescopes. The survey by Dickey et al. (1983) using the VLA is limited to lower Galactic latitudes ($|b| < 10°$). Moreover, the detection limits for this survey (HI optical depth) is much higher, $\sim$ 0.1 (3σ).

The directions chosen for the GMRT observations described in chapter 2 had the star (towards which absorption studies were made) and the radio source aligned closer to each other as compared to the earlier attempt (Rajagopal et al., 1998a) and the detections favour a smaller size for these fast clouds. Keeping in mind the explanations for large velocities by Siluk & Silk as originating in the SNRs, one can expect these higher velocity clouds to have less column density as compared to the lower velocity clouds (due to shock heating and evaporation). Therefore, in order to build statistics of HI absorption features and compare them with the existing optical data, one will need higher sensitivity levels and also a survey at higher Galactic latitudes where the lines of sight sample only the nearby clouds as in the optical observations. In addition, the effect of differential Galactic rotation is minimal since we are studying only the gas in the local Interstellar medium.

This brings us to the basic motivation for this chapter. The GMRT which consists of 30 dishes of 45 meter diameter each provides excellent collecting area to achieve very deep sensitivity limits in reasonable integration time. **The principal aim of this chapter is to study the kinematics of Interstellar clouds in the solar neighbourhood**. A lower cutoff for galactic latitude was chosen to be 15°, so that given the scale height of the clouds effects due to Galactic rotation will be minimal. Assuming a gas layer of half thickness $\sim$ 200 pc, the pathlength sampled by lines of sight at b = 15° is 750 pc, which is comparable to the distances towards bright stars.

3.2 THE DIFFERENTIAL ROTATION OF THE GALAXY

The Galaxy rotates differentially, with the inner parts of the disk (within 3 kpc from the center of the Galaxy) in an almost solid body rotation and the outer parts showing an

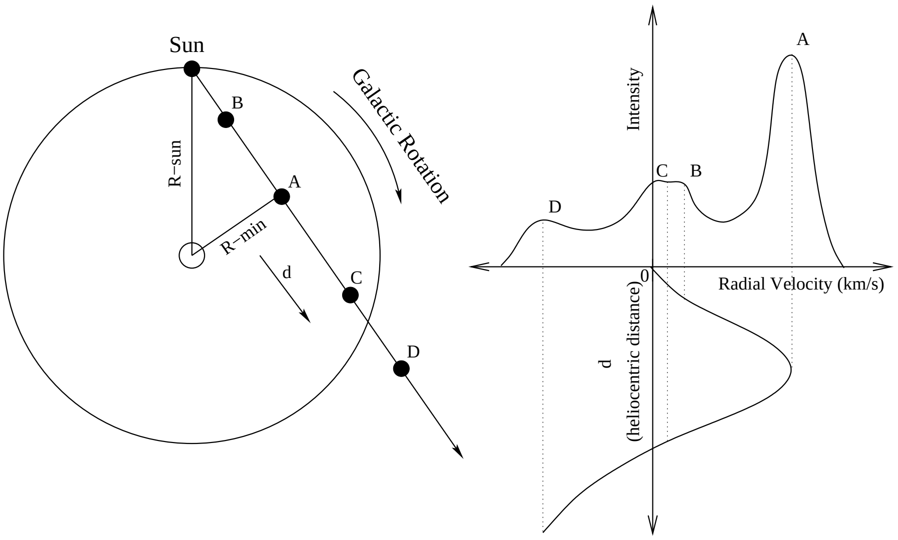

Fig. 3.2 The measured velocity of HI 21cm-line and its relation to the differential Galactic rotation. In the figure, the point "A" corresponds to the minimum Galactocentric distance for the given line of sight and hence is at highest velocity. In addition, due to higher density of HI per velocity bin (velocity crowding near the maxima of the radial velocity curve, eqn 3.7), the measured intensity is also higher. Points "B" and "C" are moving at about the same angular velocity, which is greater than that of the sun. "D" is outside the solar circle, hence it moves slower than the sun, resulting in negative radial velocities.

almost constant rotation velocity, with a slow decline as a function of Galactocentric distance. As a first order approximation, it can be assumed that the motions of the gas about the center of the Galaxy is circular everywhere. Therefore, matter within the radius of sun's orbit ($R_\odot$; the solar circle) in the Galaxy rotates faster compared to us, than the matter outside this radius. Consider any line of sight in the inner Galaxy, along the direction of rotation. As the heliocentric distance increases along this line of sight, the distance of the point from the Galactic center at first decreases. Therefore, the radial component of the differential Galactic rotation increases as a function of distance. However, as the distance increase further, a point along the line of sight is reached which is closest to the Galactic center (for the given direction). Beyond this point the radial component decreases. The value for the radial component reach zero when it reaches a point which is at the same Galactocentric-distance as sun. It drops below zero for still larger distances, since these regions are in the outer Galaxy, beyond the solar circle (See Fig. 3.2).

For a line of sight in the plane of the Galaxy, at a longitude l, the general formula for the radial component of Galactic rotation is:

$$V_r = R_\odot \left[\Omega_R - \Omega_\odot\right] sin\, l \tag{3.7}$$

Where V_r is the radial component of differential Galactic rotation. Ω_R is the angular rotation velocity at a Galactocentric-distance R, $\Omega_\odot$ is the angular rotation velocity of the sun, $R_\odot$ is the radius of solar circle and l is the Galactic longitude of the direction. The direction towards the center of the Galaxy (l = 0°) and towards the anticenter (l = 180°), the Galactic rotation velocity is entirely perpendicular to the line of sight and hence no radial component can be measured.

For the solar neighbourhood, we can rewrite equation 3.7 in terms of the helio centric distance r and the Oort's constant A as

$$V_r = Ar\ sin\ 2l \tag{3.8}$$

The equations 3.7 and 3.8 are based on several approximations. Extensive studies on the distribution of atomic, molecular and ionized hydrogen in the Galaxy have yielded models for the rotation of the Galaxy. The latest such discussion was carried out by Brand & Blitz (1993). They provide an emperical relation of the form

$$\Omega_R = \Omega_\odot \left[\frac{R_\odot}{R}\right]\left[1.00767\left(\frac{R}{R_\odot}\right)^{0.0394} + 0.00712\right] \tag{3.9}$$

We have used equation 3.9 for all relevent discussions in this thesis.

3.3 THE SOURCE SELECTION

In selecting the sources, we have used a lower cutoff in flux density at 1 Jy at 20cm wavelength. This was to ensure that we reach an **rms in HI optical depth $\sim$ 0.003** within an observing time less than an hour. Much of the data was collected during the commissioning stage of the GMRT, hence the estimates for observing time was made for fewer than 30 dishes. In order to make a sample of these bright sources uniformly distributed all over the sky we have used the VLA calibrator manual as the basic finding list. A list of 104 unresolved point sources (for the VLA in the B array configuration) with the Galactic latitude $|b| \geq 15°$ was selected. Figure 3.3 shows the distribution of the program sources in the sky.

To supplement the absorption spectra obtained by us, HI emission profiles were extracted from the Leiden-Dwingeloo all sky survey of Galactic neutral hydrogen (LDS, Hartmann & Burton, 1995). This survey used the 25 meter Dwingeloo telescope to map the sky in HI emission. The half power beam width of the Dwingeloo telescope is $\sim$ 36$'$, as compared to the synthesized beam width of few arc seconds for the GMRT. Hence there are obvious uncertainties in the detailed correspondence between the HI emission and absorption spectra. The geographic latitude of the Dwingeloo telescope is $\sim$ +53° and that of the GMRT is $\sim$ +19°. Therefore some of the lines of sight in the southern hemisphere observed with the GMRT are not accessible for the Dwingeloo

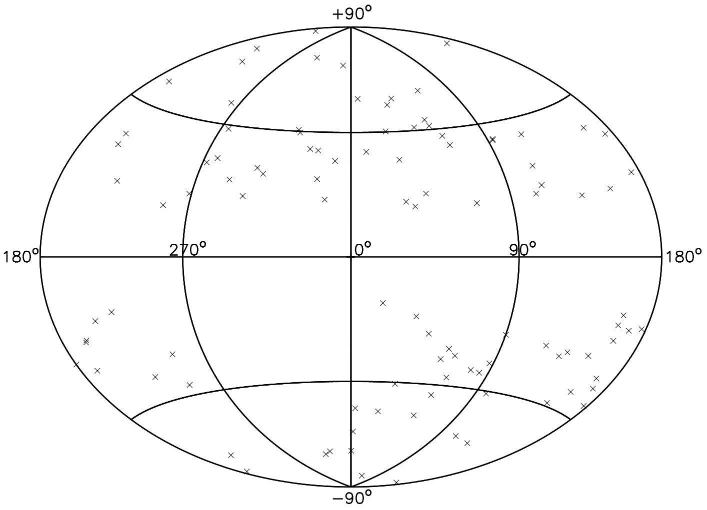

Fig. 3.3 The distribution of program sources in Galactic co-ordinates. The fourth Galactic quadrant (270° $< l <$ 360°) is not sampled well since this region is mainly in the southern equatorial hemisphere and not reachable with the GMRT

telescope and hence the survey data is not available for HI emission.

3.4 OBSERVATIONS

The HI absorption observations were carried out using the GMRT during the period March–April 2000, and April–June 2001. We used a baseband of width 2 MHz, which translates to $\approx$ 422 km s^{-1} in velocity and a resolution of $\sim$ 3.3 km s^{-1}. The center of the band was set at 1420.4 MHz. We used one of the VLA primary flux calibrators (3C48/3C147/3C286) for setting the flux density scale. Since all the program sources were point sources from the VLA calibrator manual, they served as excellent phase calibrators themselves. Bandpass calibration was carried out once every two hours for 10 minutes using 3C286, towards which no HI absorption has been detected down to an optical depth $\tau_{HI} \sim$ 0.002. On source integration time ranged from $\sim$ 10 to 60 minutes, depending on the strength of the background radio source. The rms sensitivity in optical depth varied from 0.002 to 0.008 towards different sources. **We achieved a mean value for the rms sensitivity 0.003 in HI optical depth in this**

Table 3.1 The Observational Setup.

Telescope	GMRT
System temperature	$\sim$ 70 K
Aperture efficiency	$\sim$ 40%
Number of antennas	20
Base band used	2.0 MHz
Number of channels	128
Velocity resolution	3.3 km s^{-1}
On source integration time	$\sim$ 10 to 60 minutes

survey, which makes it the most sensitive HI absorption survey carried out so far. A summary of the observational setup is given in Table 3.1.

The analysis of the data was carried out using the Astronomical Image Processing System (AIPS) developed by the National Radio Astronomy Observatory. The resulting data set consisted of 104 image cubes. On an average, we used $\sim$ 20 antennas for the final analysis. Continuum subtraction was carried out by fitting a second order baseline to the line-free channels in the image cube and subtracting the best fit continuum from all the channels. When the spectral dynamic range is around 500 or more we find that a linear baseline is not a good model for the spectral baseline. However, within the central 50% of the band, a linear fit was adequate. We have used a second order fit in order to get a better fit to the entire 2 MHz bandwidth used for our observations. To study the individual HI absorption components multiple Gaussian profiles were fitted to the absorption line spectra using the Groningen Image Processing System (GIPSY). **Apart from the new HI absorption measurements with the GMRT, we have extracted the HI emission profiles towards these lines of sight (if available) from the Leiden-Dwingeloo sky survey** (Hartmann & Burton, 1995). These profiles were also fitted with multiple Gaussian components using GIPSY. The list of observed sources are listed in table: 5.2

3.5 RESULTS

We have measured the HI absorption towards 104 bright radio continuum sources located at Galactic latitude $|b| > 15^\circ$. We have extracted HI emission profiles in these directions from the Leiden-Dwingeloo sky survey. The emission and absorption data may be combined to give the spin temperature of the gas in the associated HI clouds, using the relation

Table 3.2 The list of sources observed with the GMRT. The last column gives the *rms* optical depth achieved.

		J2000 R.A.			Decl.			l	b	τ_{rms}
	Source	(Hr	m	s)	(^{o}	$'$	$''$)	(deg)	(deg)	
1	J0010–418	0	10	52.52	–41	53	10.8	329.68	–73.07	0.002
2	J0022+002	0	22	25.43	0	14	56.1	107.46	–61.75	0.003
3	J0024–420	0	24	42.99	–42	2	4.0	321.35	–74.12	0.003
4	J0025–260	0	25	49.17	–26	2	12.7	42.27	–84.17	0.003
5	J0029+349	0	29	14.24	34	56	32.2	117.79	–27.71	0.002
6	J0059+001	0	59	5.51	0	6	51.6	127.11	–62.70	0.004
7	J0116–208	1	16	51.40	–20	52	6.8	167.11	–81.47	0.003
8	J0119+321	1	19	35.00	32	10	50.1	129.83	–30.31	0.003
9	J0137+331	1	37	41.30	33	9	35.1	133.96	–28.72	0.003
10	J0204+152	2	4	50.41	15	14	11.0	147.93	–44.04	0.003
11	J0204–170	2	4	57.67	–17	1	19.8	185.99	–70.23	0.003
12	J0237+288	2	37	52.41	28	48	9.0	149.47	–28.53	0.003
13	J0238+166	2	38	38.93	16	36	59.3	156.77	–39.11	0.004
14	J0240–231	2	40	8.17	–23	9	15.7	209.79	–65.13	0.003
15	J0318+164	3	18	57.80	16	28	32.7	166.64	–33.60	0.002
16	J0321+123	3	21	53.10	12	21	14.0	170.59	–36.24	0.002
17	J0323+055	3	23	20.26	5	34	11.9	176.98	–40.84	0.003
18	J0329+279	3	29	57.67	27	56	15.5	160.70	–23.07	0.003
19	J0336+323	3	36	30.11	32	18	29.3	159.00	–18.77	0.004
20	J0348+338	3	48	46.90	33	53	15.0	160.04	–15.91	0.003
21	J0403+260	4	3	5.59	26	0	1.5	168.03	–19.65	0.004
22	J0409+122	4	9	22.01	12	17	39.8	180.12	–27.90	0.003
23	J0410+769	4	10	45.61	76	56	45.3	133.41	18.33	0.002
24	J0424+020	4	24	8.56	2	4	24.9	192.04	–31.10	0.004
25	J0431+206	4	31	3.76	20	37	34.3	176.81	–18.56	0.003
26	J0440–435	4	40	17.18	–43	33	8.6	248.41	–41.57	0.003
27	J0453–281	4	53	14.65	–28	7	37.3	229.09	–37.02	0.004
28	J0459+024	4	59	52.05	2	29	31.2	197.01	–23.34	0.003
29	J0503+020	5	3	21.20	2	3	4.7	197.91	–22.82	0.004
30	J0538–440	5	38	50.36	–44	5	8.9	250.08	–31.09	0.002
31	J0541–056	5	41	38.08	–5	41	49.4	210.05	–18.11	0.004
32	J0609–157	6	9	40.95	–15	42	40.7	222.61	–16.18	0.007
33	J0614+607	6	14	23.87	60	46	21.8	153.60	19.15	0.005
34	J0713+438	7	13	38.16	43	49	17.2	173.79	22.20	0.004
35	J0814+459	8	14	30.31	45	56	39.5	173.90	33.17	0.005
36	J0825+031	8	25	50.34	3	9	24.5	221.22	22.39	0.002
37	J0834+555	8	34	54.90	55	34	21.1	162.23	36.56	0.002
38	J0842+185	8	42	5.09	18	35	41.0	207.28	32.48	0.004

		J2000 R.A.			Decl.			l	b	τ_{rms}
	Source	(Hr	m	s)	(^{o}	$'$	$''$)	(deg)	(deg)	
39	J0854+201	8	54	48.87	20	6	30.6	206.81	35.82	0.002
40	J0921–263	9	21	29.35	–26	18	43.4	255.07	16.48	0.003
41	J0958+324	9	58	20.95	32	24	2.2	194.17	52.32	0.005
42	J1018–317	10	18	9.28	–31	44	14.1	268.61	20.73	0.002
43	J1057–245	10	57	55.42	–24	33	48.9	272.47	31.51	0.004
44	J1111+199	11	11	20.07	19	55	36.0	225.01	66.00	0.003
45	J1119–030	11	19	25.30	–3	2	51.3	263.01	52.54	0.002
46	J1120–251	11	20	9.12	–25	8	7.6	278.09	33.30	0.003
47	J1125+261	11	25	53.71	26	10	20.0	210.92	70.89	0.003
48	J1130–148	11	30	7.05	–14	49	27.4	275.28	43.64	0.002
49	J1146+399	11	46	58.30	39	58	34.3	164.95	71.47	0.009
50	J1154–350	11	54	21.79	–35	5	29.0	289.93	26.34	0.002
51	J1221+282	12	21	31.69	28	13	58.5	201.74	83.29	0.004
52	J1235–418	12	35	41.93	–41	53	18.0	299.80	20.89	0.003
53	J1254+116	12	54	38.26	11	41	5.9	305.87	74.54	0.005
54	J1257–319	12	57	59.06	–31	55	16.9	304.55	30.93	0.003
55	J1316–336	13	16	7.99	–33	38	59.2	308.80	28.94	0.006
56	J1344+141	13	44	23.74	14	9	14.9	349.16	72.09	0.003
57	J1351–148	13	51	52.65	–14	49	14.9	324.03	45.56	0.003
58	J1357–154	13	57	11.24	–15	27	28.8	325.42	44.52	0.015
59	J1432–180	14	32	57.69	–18	1	35.2	334.35	38.57	0.007
60	J1435+760	14	35	47.10	76	5	25.8	115.07	39.40	0.003
61	J1445+099	14	45	16.47	9	58	36.1	5.79	58.17	0.002
62	J1448–163	14	48	15.05	–16	20	24.5	339.45	38.11	0.003
63	J1506+375	15	6	9.53	37	30	51.1	61.65	59.90	0.003
64	J1513+236	15	13	40.19	23	38	35.2	34.77	57.79	0.002
65	J1517–243	15	17	41.81	–24	22	19.5	340.68	27.58	0.004
66	J1520+202	15	20	5.49	20	16	5.6	29.64	55.42	0.003
67	J1526–138	15	26	59.44	–13	51	0.1	350.48	34.29	0.002
68	J1553+129	15	53	32.70	12	56	51.7	23.79	45.22	0.003
69	J1554–270	15	54	2.49	–27	4	40.2	345.68	20.27	0.003
70	J1557–000	15	57	51.43	0	1	50.4	9.58	37.68	0.004
71	J1602+334	16	2	7.26	33	26	53.1	53.73	48.71	0.002
72	J1609+266	16	9	13.32	26	41	29.0	44.17	46.20	0.003
73	J1613+342	16	13	41.06	34	12	47.9	55.15	46.38	0.001
74	J1634+627	16	34	33.80	62	45	35.9	93.61	39.38	0.002
75	J1635+381	16	35	15.49	38	8	4.5	61.09	42.34	0.002
76	J1638+625	16	38	28.21	62	34	44.3	93.22	39.01	0.003

		J2000 R.A.			Decl.			l	b	τ_{rms}
	Source	(Hr	m	s)	(^{o}	$'$	$''$)	(deg)	(deg)	
77	J1640+123	16	40	47.93	12	20	2.1	29.43	34.51	0.003
78	J1653+397	16	53	52.22	39	45	36.6	63.60	38.86	0.003
79	J1737+063	17	37	13.73	6	21	3.5	30.15	19.38	0.005
80	J1745+173	17	45	35.21	17	20	1.4	41.74	22.12	0.004
81	J1751+096	17	51	32.82	9	39	0.7	34.92	17.65	0.002
82	J1800+784	18	0	45.68	78	28	4.0	110.04	29.07	0.002
83	J1845+401	18	45	11.12	40	7	51.5	69.36	18.21	0.003
84	J1923–210	19	23	32.19	–21	4	33.3	17.18	–16.25	0.003
85	J2005+778	20	5	31.00	77	52	43.2	110.46	22.73	0.003
86	J2009+724	20	9	52.30	72	29	19.4	105.36	20.18	0.003
87	J2011–067	20	11	14.22	–6	44	3.6	36.01	–20.80	0.002
88	J2047–026	20	47	10.35	–2	36	22.2	44.56	–26.80	0.002
89	J2130+050	21	30	32.88	5	2	17.5	58.65	–31.81	0.002
90	J2136+006	21	36	38.59	0	41	54.2	55.47	–35.58	0.002
91	J2137–207	21	37	50.00	–20	42	31.8	30.35	–45.56	0.002
92	J2148+069	21	48	5.46	6	57	38.6	63.66	–34.07	0.002
93	J2212+018	22	12	37.98	1	52	51.2	63.68	–42.02	0.001
94	J2214–385	22	14	38.57	–38	35	45.0	3.47	–55.44	0.002
95	J2219–279	22	19	40.94	–27	56	26.9	22.57	–56.48	0.003
96	J2225–049	22	25	47.26	–4	57	1.4	58.96	–48.84	0.003
97	J2232+117	22	32	36.41	11	43	50.9	77.44	–38.58	0.003
98	J2236+284	22	36	22.47	28	28	57.4	90.12	–25.65	0.004
99	J2246–121	22	46	18.23	–12	6	51.3	53.87	–57.07	0.003
100	J2250+143	22	50	25.54	14	19	50.6	83.89	–39.20	0.002
101	J2251+188	22	51	34.74	18	48	40.1	87.35	–35.65	0.002
102	J2302–373	23	2	23.89	–37	18	6.8	2.16	–64.91	0.002
103	J2340+135	23	40	33.22	13	33	0.9	97.80	–45.83	0.002
104	J2341–351	23	41	45.89	–35	6	22.1	0.45	–73.12	0.004

$$T_B = T_S(1 - e^{-\tau_\nu}) \tag{3.10}$$

Knowing the line brightness temperature T$_B$, and the optical depth τ, one can estimate the spin temperature T$_S$. Any line of sight is expected to have HI gas that absorbs, as well as emits, (the cold clouds) and also the warm intercloud gas in which absorption will be extremely low. Deriving the spin temperature is complicated by the contribution of these two phases to emission. Difficulties arise because the observable quantities, optical depth

$$\tau \propto \frac{\int ndl}{T_S} \tag{3.11}$$

here, n is the volume density of H atoms, T$_S$ is the spin temperature and L is the total pathlength.

Therefore, for a given pathlength L, The line brightness temperature,

$$\begin{aligned} T_B &\propto \int ndl \qquad\qquad (\tau \ll 1) \\ T_B &\propto T \qquad\qquad (\tau \gg 1) \end{aligned}$$

Hence, absorption profiles are dominated by cold HI gas along the line of sight, while warm gas is prominent in emission profiles. A faithful separation of both the contributions to the emission profile is required; otherwise the derived spin temperature of the cold gas will be higher. This bias become more apparent at low optical depths. We have used Gaussian fitting to the spectra to separate the profiles into discrete Gaussian components. An HI emission component with the same central velocity as the absorption component can be assumed to arise from the same cloud. **However, there exists a possibility of chance coincidence when the HI emission lines arising from the Intercloud medium is at the velocity of the narrow HI absorption line**. The emission lines from the Intercloud medium are always wider ($\sigma_\nu \geq 8$ km s^{-1}) since the gas is warmer. **To avoid such coincidences we have imposed a restriction that only those lines with $\sigma_\nu < 8$ km s^{-1} are used for spin temperature calculations**. Lower limits for the spin temperature of the Intercloud medium was estimated separately.

In the following subsections, we briefly explain the spectra and the statistical properties derived from it.

3.5.1 The spectra

Figure 3.4 is a sample spectrum of HI optical depth and HI emission profiles. The figure is displayed in the following way: The first panel shows the HI brightness temperature profile from the Leiden-Dwingeloo Survey. The HI optical depth profile from our observations using the GMRT is shown in the second panel. The lower panel for each figure is the approximate Galactic rotation curve for the respective line of sight, obtained from Brand & Blitz (1993). For the lower panel, the left side of the box show the heliocentric distance and the right side is marked with vertical height above the plane. The rest of the spectra are listed in Appendix A and the summary of the Gaussian fitting analysis is given in Appendix B. **In all we have obtained 126 spectral components in HI absorption and derived 486 components in HI emission from the LDS survey. The fitted parameters for the discrete components in HI absorption and emission were used to derive the spin temperature of the respective feature**.

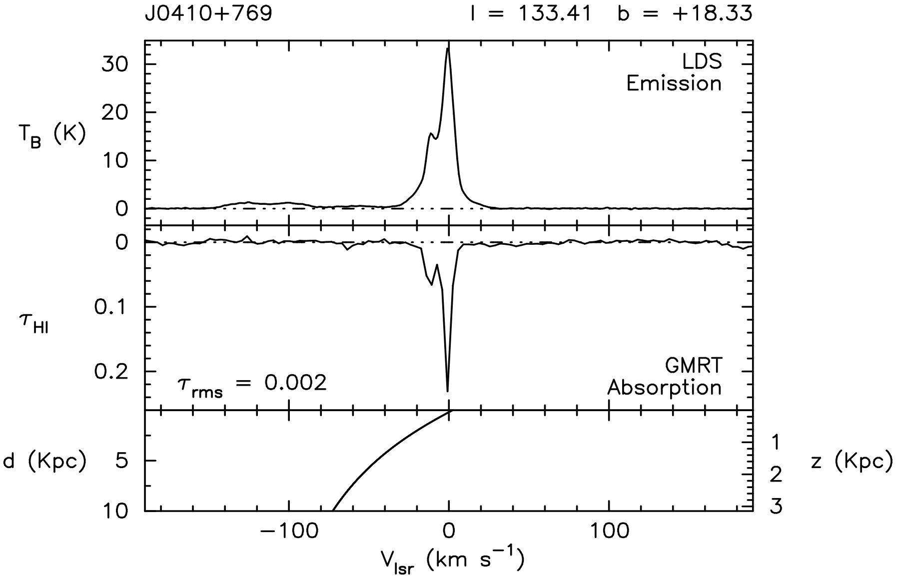

Fig. 3.4 The HI optical depth spectrum from the GMRT towards one of the 104 sources (middle panel) and the HI brightness temperature profile along the respective line of sight from the Leiden-Dwingeloo survey (top panel). The bottom panel shows the approximate variation of radial component of Galactic differential rotation along the line of sight, as a function of distance (the scale along the left side) and as a function of vertical height (scale on the right side).

3.5.2 The frequency distribution of HI emission line parameters

The frequency distribution of the mean LSR velocities of the HI emission line components are displayed in figure 3.5. As we mentioned earlier, the HI emission data contains information about the gas in the disk, as well as the gas in the Galactic halo. The velocity range between 50 and 100 km s^{-1} contains contributions from intermediate velocity clouds located in the Galactic halo also. The features seen near

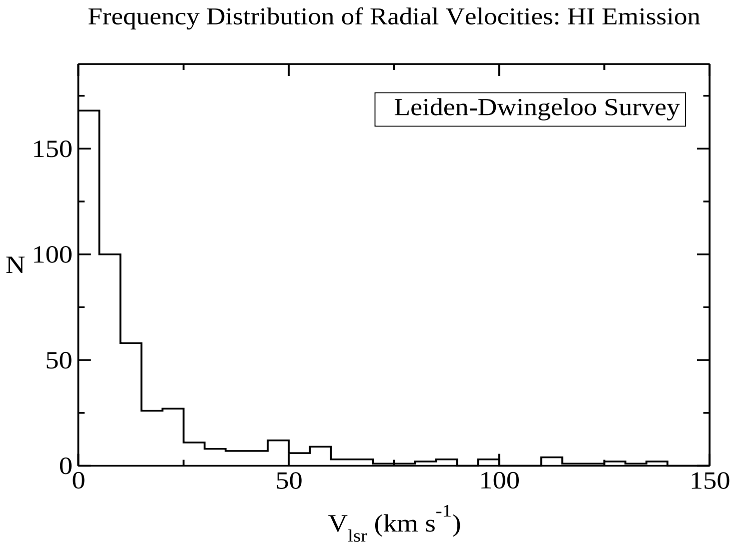
Frequency Distribution of Radial Velocities: HI Emission

Fig. 3.5 The frequency distribution of central V_{lsr} of the HI emission line components, in 5 km s^{-1} bins. The higher velocity features, located at $v > 90$ km s^{-1} are originating in the HVCs. At lower velocities, there is contribution from the IVCs also.

and above 100 km s^{-1} are from the high velocity clouds and cloud complexes in the Galactic halo or beyond. Both these are not a part of the interstellar medium. The spread in the peak HI brightness temperature as a function of $|V_{lsr}|$ is shown in figure 3.6. **Notice the sharp drop in the peak T_B near $V_{lsr} \sim 15$ km s^{-1}. No spectral features at velocities above 15 km s^{-1} has a peak T_B above $\sim$ 2.0K**.

The frequency distribution of the half power velocity widths of the emission components identified from the Gaussian fitting analysis are displayed in Fig. 3.7. The dataset used here is the Leiden-Dwingeloo sky survey (LDS), spectra towards those lines of sight probed by the HI absorption survey using the GMRT. The HI emission data consists of a variety of features. The smaller velocity widths, $v < 15$ km s^{-1} are from the cold clouds. The histogram extends Up to about 60 km s^{-1}, with the HI emission features arising in the warm neutral medium and also the high velocity clouds. Beyond $\sim$ 70 km $s-1$ lie the large velocity dispersion (LVD) features found in the Galactic halo, discussed in detail by Kalberla et al., (1998). These features shows a very low peak brightness temperature in HI ($T_B \sim$ 0.1K) and is clearly seen in the Dwingeloo spectra averaged over several degrees. However, there are several lines of sight where the individual spectra shows clear signs of the LVD features (fig 3.7). The smallest value for the FWHM among the HI emission features is 2.2 km s^{-1}, which implies a Doppler temperature of 106K.

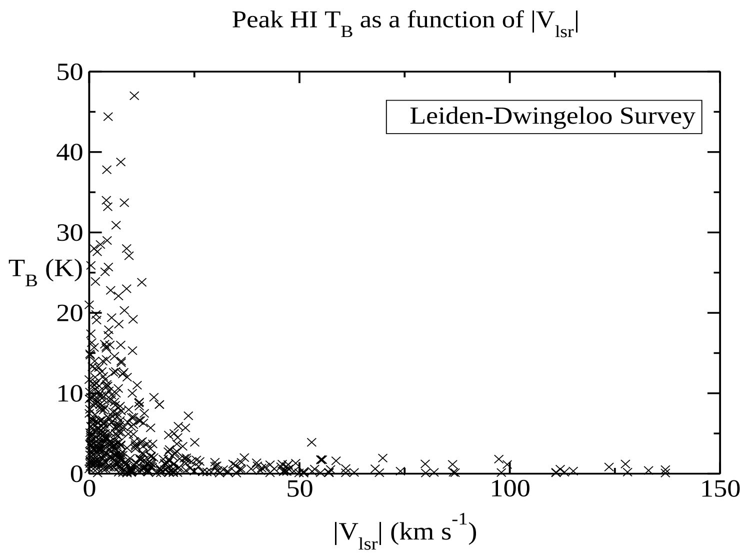

Fig. 3.6 The observed peak brightness temperature of the HI emission components as a function of $|V_{lsr}|$

3.5.3 The frequency distribution of HI absorption line parameters

We now turn to our absorption studies with the GMRT. The frequency distribution of the mean LSR velocities of the HI absorption line components are displayed in figure 3.8. The spread in the peak optical depth as a function of $|V_{lsr}|$ is shown in figure 3.9. The peak τ_{HI} drops sharply near $V_{lsr} \sim 10$ km s^{-1}. No spectral features at velocities above 10 km s^{-1} has a peak optical depth above $\sim$ 0.1; a hint of which was provided by the investigations discussed in the previous chapter. The frequency distribution of the half power velocity widths of the absorption components identified from the Gaussian fitting analysis are displayed in Fig. 3.10. The smallest fitted value for the FWHM in the HI absorption data is 1.5 km s^{-1}. Assuming this width is due to pure thermal broadening, the corresponding Doppler temperature is 40K. The half power velocity width of the absorbing features are below $\sim$ 15 km s^{-1}. All of the features detected in absorption in this survey arise in the cold HI clouds. The velocity widths of the absorption lines that arise in the Intercloud medium is much larger, (FWHM $>$ 20 km s^{-1}; we shall discuss this in Chapter 5).

At lower latitudes, it has been noticed that the number of larger optical depth features are higher (See for eg. Mebold et al., 1982). This apparent excess of large optical depth features at in the Galactic plane has been attributed to superposition of absorbing clouds along the line of sight. However, the frequency distribution of peak optical depth of the features identified in the present survey shows a different

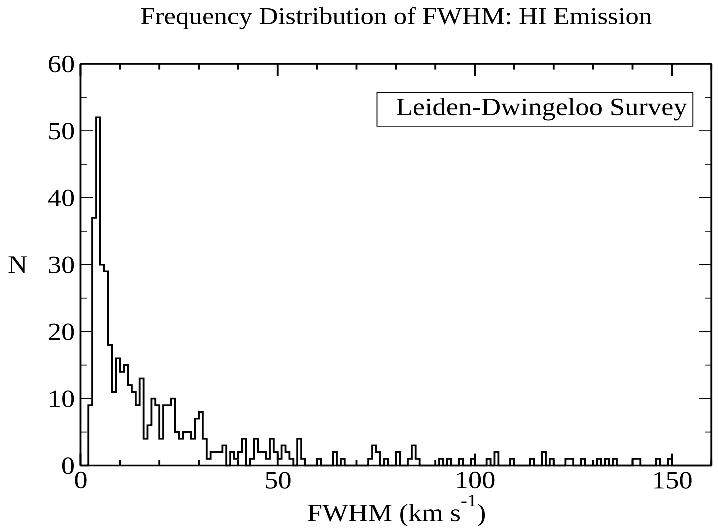

Fig. 3.7 The Frequency distribution of the half power velocity widths of HI emission features identified from the LDS, towards the lines of sight probed by the present survey. The cold clouds are within 20 km s^{-1}. The distribution continues to the Intercloud medium and HVCs up to about 50 km s^{-1}. Beyond that, the very wide features are those known as the LVD features, discussed by Kalberla et al., (1998).

trend. There are only seven features in our survey with peak optical depth above 0.5 (Fig. 3.11). We take this as an evidence that in the present dataset the superposition of more than one HI absorption feature along the line of sight is minimal. Majority of the HI absorption features are seen with a peak optical depth below 0.1. This is consistent with absorption from individual clouds, which is to be expected since we are sampling relatively small path lengths through the gas layer at higher Galactic latitudes.

3.6 DISCUSSION

3.6.1 Comparison of our HI absorption data with the previous HI surveys

Seven of the sources observed by us had been studied previously in other surveys (Table 3.6.1). However, since in all the previous studies the limiting optical depth was much larger, we have limited the comparison to the frequency distribution of the velocities of HI absorption components. In addition, we have only used those lines

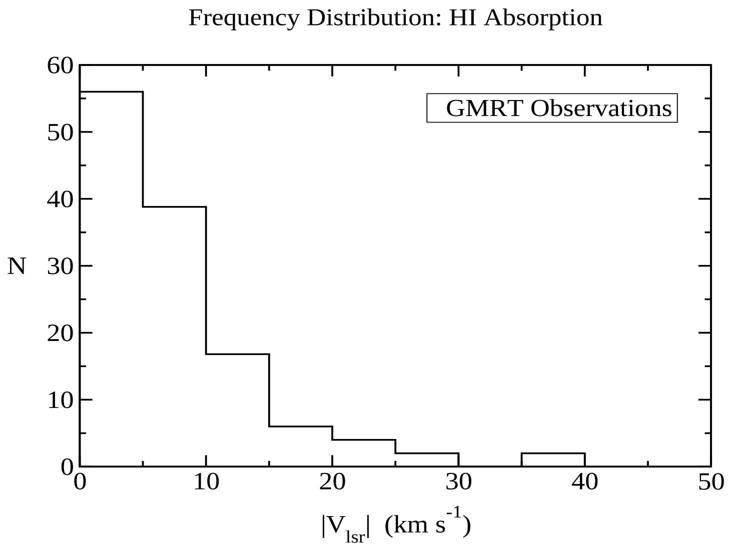

Fig. 3.8 The frequency distribution of central V_{lsr} of the HI absorption components, in 5 km s^{-1} bins.

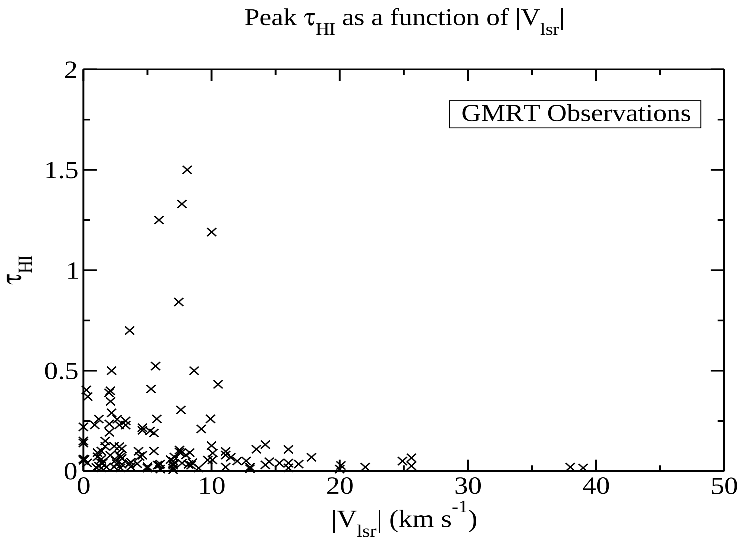

Fig. 3.9 The observed peak optical depth of the HI absorption components as a function of $|V_{lsr}|$

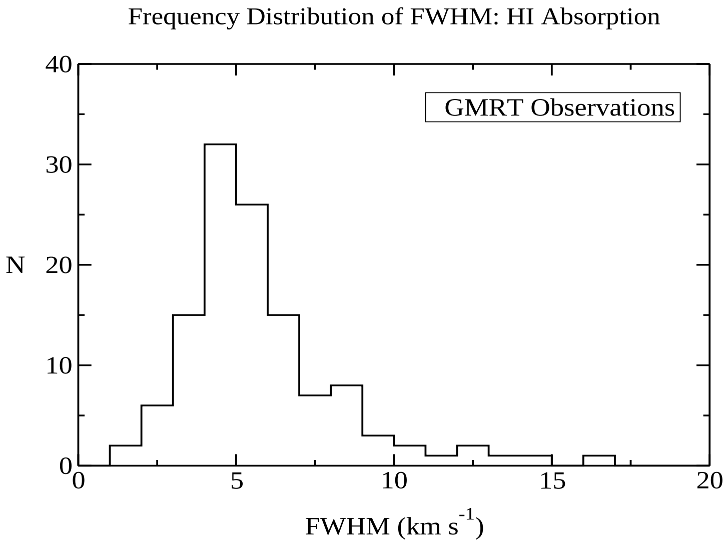

Fig. 3.10 The Frequency distribution of the half power velocity widths of HI absorption features identified from the present survey

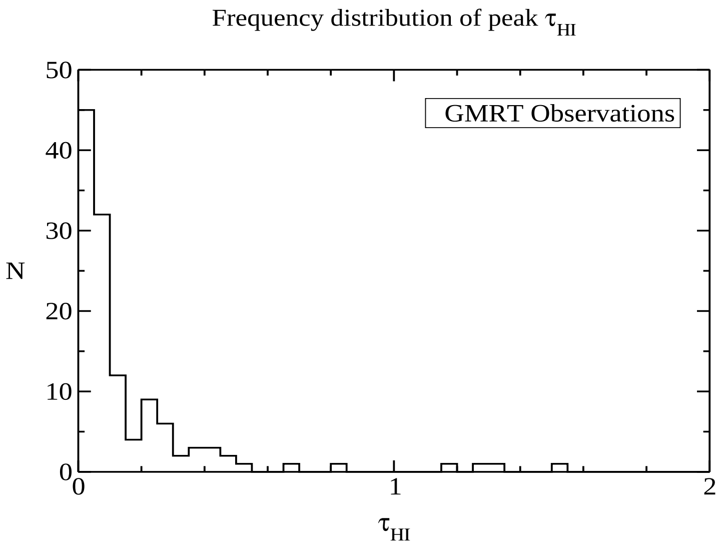

Fig. 3.11 The Frequency distribution of the peak optical depths of HI absorption features identified from the present survey

Table 3.3 The sources observed in the present survey which were observed earlier in other surveys and the limiting optical depths. In the first column, DST78 stands for the Arecibo HI absorption survey by Dickey et al., 1978 and EGS82 stands for the Effelsberg-Greenbank HI absorption survey by Mebold et al., 1982. There are no sources common with the HI absorption survey using the Parkes Interferometer by Radhakrishnan et al., 1972. For easy reference, we have given the names of these sources used in the earlier surveys.

Source	Survey	τ_{rms}	GMRT: τ_{rms}
J0318+164/CTA 21	EG82	0.017	0.002
J0834+555/OA 251	EG82	0.025	0.002
J1154–350/1151-34	EG82	0.020	0.002
J2136+006/2134+00	EG82	0.050	0.002
J2232+117/CTA 102	EG82	0.017	0.003
J0137+331/3C 48	DST78	0.004	0.003
J0318+164/CTA 21	DST78	0.004	0.002

of sight from the previous surveys which are above the lower $|b|$ cut off of 15° used in the present observations. At this juncture, we have not made any attempt to correct for the effects of differential galactic rotation.

Figure 3.12 Shows the frequency distribution of radial velocities of HI absorption features from the present survey along with that of 22 HI absorption features from the Parkes Interferometer survey by Radhakrishnan et al (1972). No features at radial velocities larger than 15 km s^{-1} was detected in the Parkes survey. The comparison with the 37 discrete HI absorption features from the Arecibo measurements by Dickey, Salpeter & Terzian (1978) is shown in figure 3.13. The Arecibo HI absorption survey by Dickey et al. (1978) had an rms sensitivity comparable to the present survey. Although the number of absorption features from their survey is smaller, the spread in the radial velocities are found to be similar. The Effelsberg-Greenbank HI absorption survey by Mebold et al (1982) lists 69 lines of sight. Some of the sources listed in their survey was observed only with the Effelsberg 100m telescope. The single dish absorption spectra in their paper and the derived values for absorption line parameters were found to have serious discrepancies with other published data and hence was not used in this comparison. Figure 3.14 shows a comparison of radial velocity histogram from the present survey to that by Mebold et al. We have used only the Interferometric measurements from Mebold et al. It is evident from the figure that except for the single absorption feature at $\sim$–35 km s^{-1}, towards 3C 274, with a peak optical depth of 0.009, rest of the features are at velocities below $\sim$ 20 km s^{-1}. This source was not covered by the GMRT observations.

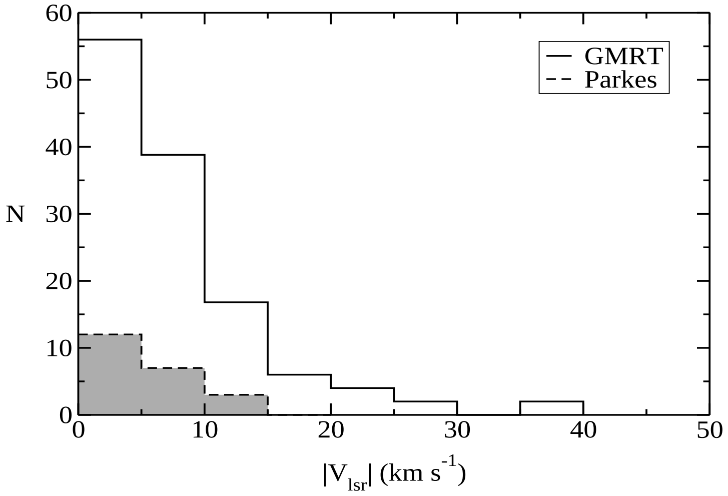

Fig. 3.12 The frequency distribution of mean LSR velocities of the HI absorption features identified from the present survey (solid line) along with that of 22 HI absorption features from the Radhakrishnan et al (1972) survey using the Parkes Interferometer.

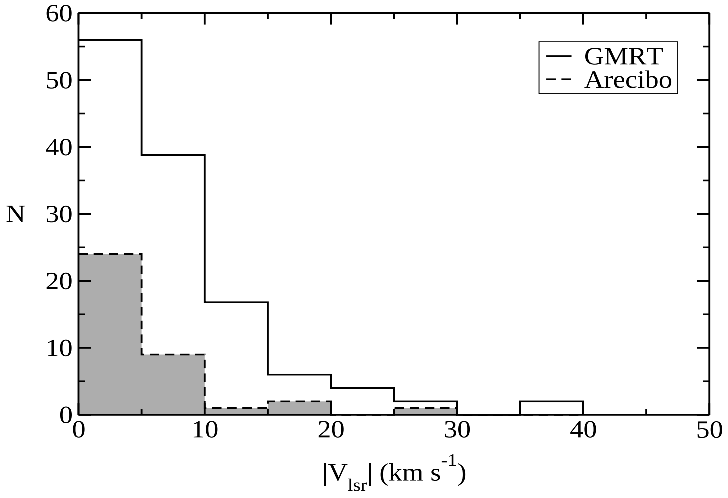

Fig. 3.13 The frequency distribution of mean LSR velocities of the HI absorption features identified from the present survey (solid line) along with that of 37 HI absorption features from the Dickey, Salpeter & Terzian (1978) study using the Arecibo telescope.

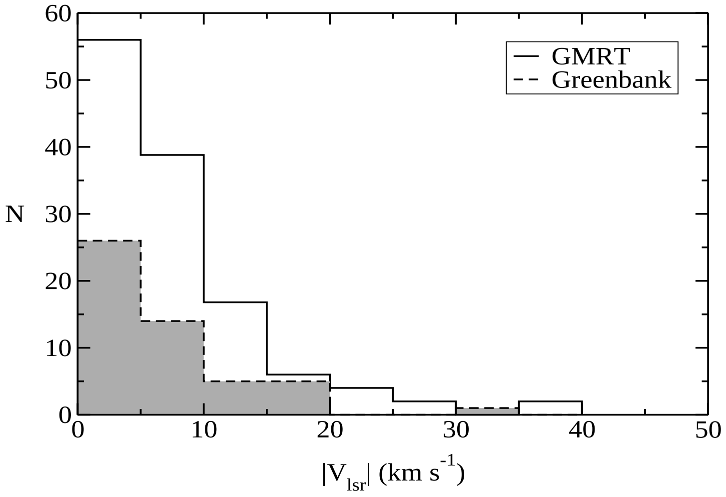

Fig. 3.14 The frequency distribution of mean LSR velocities of the HI absorption features from the present survey (solid line) along with 51 HI absorption features from Mebold et al (1983), using the Green Bank Interferometer

It is clear from the figures 3.12, 3.13 and 3.14, that the present dataset has not only detected more absorbing clouds, but also more higher velocity clouds. The peak optical depth of these features at higher velocities are found to be lower as compared to the rest of the clouds (See Figure 3.9). The importance of these features become clear once we compare our data with the optical absorption line studies.

3.6.2 Comparison of HI Absorption data with the Optical surveys

The CaII and NaI absorption studies of Adams, Blaauw, Münch, Münch & Zirrin and others revealed two set of absorption features, one at lower and the other at higher radial velocities. The attempts at arriving at a better understanding of the kinematics and structure of the ISM through optical absorption line studies continued. High resolution spectra of NaI lines (eg. Welty et al, 1994) and CaII lines (Welty et al, 1996) have been obtained towards a number of stars. The velocities and line widths of these atoms have been studied to explore their nature. In this section, we compare the present dataset of HI emission (From the Leiden-Dwingeloo survey) and absorption line velocities from the GMRT survey with that of optical lines from various surveys, starting from Blaauw's (1952) study.

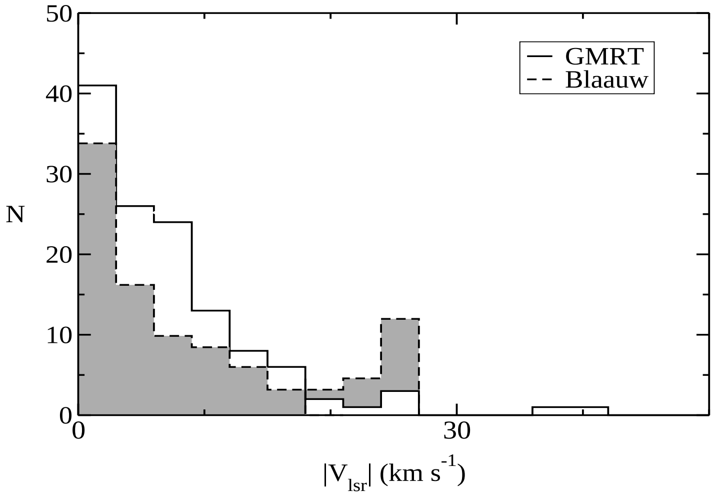

Fig. 3.15 The frequency distribution of the radial velocities of HI absorption features identified from the present survey along with that of optical absorption lines from Blaauw, 1952 (dashed line). The secondary peak at high velocity in Blaauw's histogram is an artifact of the binning used by Blaauw. All the features with radial velocity $V_{lsr} \geq 21$ km s^{-1} were counted in a single bin.

Figure 3.15 shows the frequency distribution of the velocities of the HI absorption features from the present survey with that from Blaauw's study. In the figure, we have binned our data to match the bin size used by Blaauw (3 km s^{-1}). This is the reason why our histogram looks different from figs. 3.12, 3.13 and 3.14. Also, the secondary peak at high velocity in Blaauw's histogram is an artifact of the binning used by Blaauw. All the features with radial velocity $V_{lsr} \geq 21$ km s^{-1} were counted in a single bin. It is evident that both the distributions agree well. Recall that the previous HI absorption surveys had a sharp cutoff for the radial velocity distribution at $\sim$ 15 km s^{-1}.

Figure 3.16 shows the frequency distribution of the central V_{lsr} of the HI absorption features from the present survey along that from the data used by Siluk & Silk (1974). A first look at this figure would seem to imply that a major part of the high velocity tail seen in the optical absorption line velocities, extending all the way up to $\sim$ 100 km s^{-1} is missing in the HI absorption data. *Figure 3.17, which compares the normalized histograms from the HI emission data obtained from the Leiden-Dwingeloo survey to that from the same optical absorption line data reveals a different story.* There is a good correspondence between the HI emission feature velocities and the optical absorption features, in all the velocity ranges. Recall that the HI emission

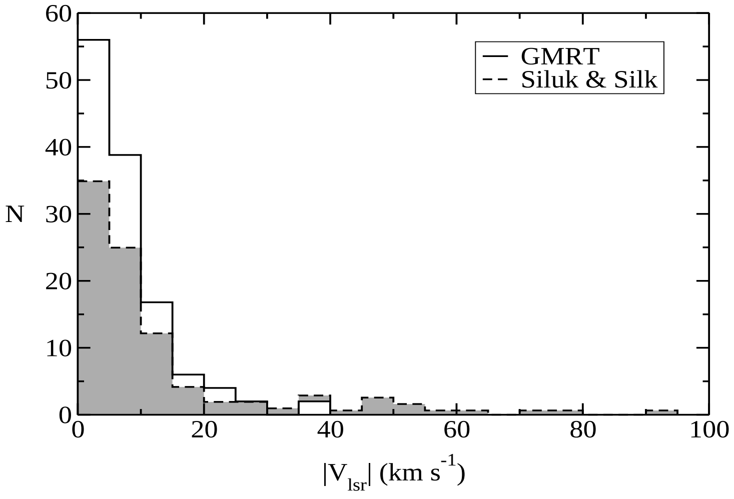

Fig. 3.16 The frequency distribution of the radial velocities of HI absorption features identified from the present survey along with that of optical absorption line data used by Siluk & Silk, 1974 (dashed line).

data consists of large scale features like the so called "*High Velocity Clouds*" in the Galactic halo. The dataset used by Siluk & Silk is towards bright stars as distant as 2 kpc. The question is can this dataset therefore include the "High Velocity Clouds" and other large scale systematic motions of the spiral arms? This is important and needs to be examined. Hence we have re-analyzed the lines of sight probed by Siluk & Silk (1974) to search for any large scale systematic features in addition to random motions.

There are 18 CaII absorption features at velocities greater than 25 km s^{-1} in the data used by Siluk and Silk. A quick look at the co-ordinates of the stars and the velocities of the optical absorption features in their spectra reveal that the stars HD14134, HD14143, HD14818, HD190429, HD216411and HD225094 are located at a distance $\sim$ 2000 pc. The Galactic longitudes of these stars are from $\sim$ 75° to 135°. All of them within a latitude range, b $\sim$ –4° - +3°. Therefore, all these stars could be in the Perseus spiral arm of the Galaxy. The radial velocity of the gas in this spiral arm is known to be up to $\sim$ 50 km s^{-1}. Hence we wish to point out that the high velocity optical absorption lines seen in the spectra towards these stars may not represent true peculiar motion, but rather a *systematic motion*. For the case of the star HD193322, the high velocity CaII absorption line at $\sim$ 26 km s^{-1} (V_{lsr}) is originating in a large scale feature in the Galactic disk, evident from the longitude-velocity diagram.

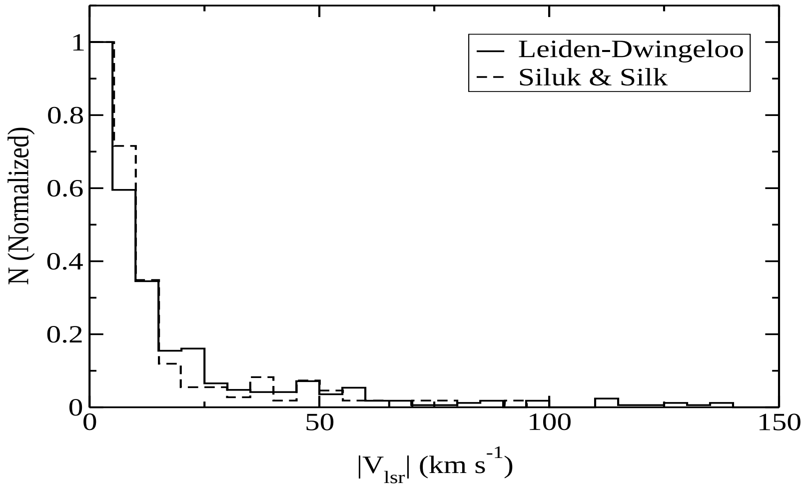

Fig. 3.17 The normalized frequency distribution of the radial velocities of HI emission features identified from the Leiden-Dwingeloo survey along with that of optical absorption line data from Siluk & Silk, 1974 (dashed line).

The star HD169454 is at a distance of 1000 pc and shows CaII absorption line at a large velocity of V$_{lsr}$ = +94.5 km s^{-1}. The co-ordinates of this star (l = 18°, b = $-1°$) is close to the HVC 282 in the catalog of Wakker and VanWoerden (1991). This is an extended cloud with a surface area of 165.6 deg^2, and intercepts the line of sight to the star. The HI emission from this cloud complex shows overlapping multiple features extending in velocity from $\sim$ 90 to 150 km s^{-1}. The centroid of this emission is at +116 km s^{-1} and the co-ordinates corresponding to this centroid are l = 20.3° and b = +1.8°. Given the wide emission feature, it is conceivable that the CaII absorption line originates in this cloud complex. If this is true, then this indirectly provides an upper limit of 1000 pc for the distance to this HVC.

The star HD 175754, is at a distance of 2000 pc and the CaII absorption line in the line of sight to the star is at V$_{lsr}$= –74.6 km s^{-1}. There is an HVC complex known as GCN in this direction. Again, the HI emission from cloud 261 of this complex (in the catalog of Wakker and VanWoerden) extends over a velocity range –50 to –85 km s^{-1}. In our opinion, the CaII absorption towards the star HD 175754 can be attributed to this cloud complex.

In a similar vein, we have tried to understand the possible origin of some of the rather high velocity absorption features in the catalog of Siluk and Silk, 1974. Our conclusions are summarized in Table 3.4. In brief, some of the absorption at the high

Table 3.4 The lines of sight from Siluk & Silk (1974), wherein the large velocity optical absorption line features are identified as arising from various large scale features.

Star	l (deg)	b (deg)	d (pc)	V_r (km s^{-1}	Comments
HD14134	135	–4	2100	–56.6	Perseus Spiral arm
HD14143	135	–4	2000	–55.1	Perseus Spiral arm
HD14818	136	–4	2200	–40.1	Perseus Spiral arm
HD93521	183	+62	2000	–35.3	Halo gas - large scale feature
HD166937	10	–2	1100	+39.1	These two are arising from the
HD167294	10	–2	1380	+40.6	same feature.
HD169454	18	–1	1000	+94.5	HVC complex GCP
HD175754	16	–10	2000	–74.6	HVC complex GCP
HD190429	73	+3	1450	–65.2	Perseus Spiral arm
HD193322	78	+3	870	–26.6	Large scale Galactic feature
HD214680	97	–17	600	–24.7	These two are arising from the
HD214993	98	–16	500	–25.6	same feature
HD216411	108	0	1900	–47.1	Perseus Spiral arm
HD225094	118	+1	2080	–45.8	Perseus Spiral arm

velocity end may not represent large peculiar velocities of diffuse HI clouds; they could either be due to large systematic motions superimposed on random motions or from the so called High Velocity Clouds.

If the absorptions listed in table 3.4 are excluded from the dataset of Siluk and Silk, then the reconstructed histogram is shown in Fig. 3.18.

Excluding the features discussed above, we have re-constructed the histogram of optical absorption line velocities from the data of Siluk & Silk (Fig 3.18). We would like to mention that there is one direction, towards the star HD212978, where the CaII absorption line velocity coincides with that of a Galactic spiral arm at –77.9 km s^{-1}. However, given the distance to this star as 450 pc, this is only a chance coincidence. The modified histogram from Siluk & Silk is in a better agreement with the HI absorption velocity histogram, though the velocity spread of CaII lines are definitely more than that of the HI features.

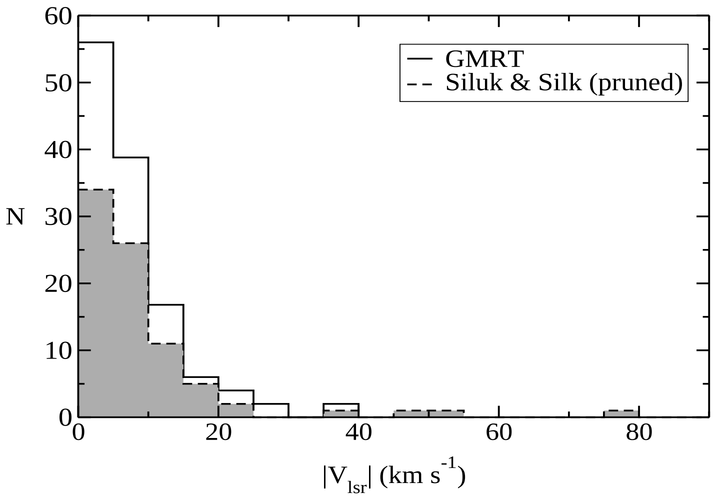

Fig. 3.18 The frequency distribution of the radial velocities of HI absorption features identified from the present study along with that of optical absorption line data from Siluk & Silk, 1974, excluding the CaII absorption lines arising in large scale features and HVCs (dashed line).

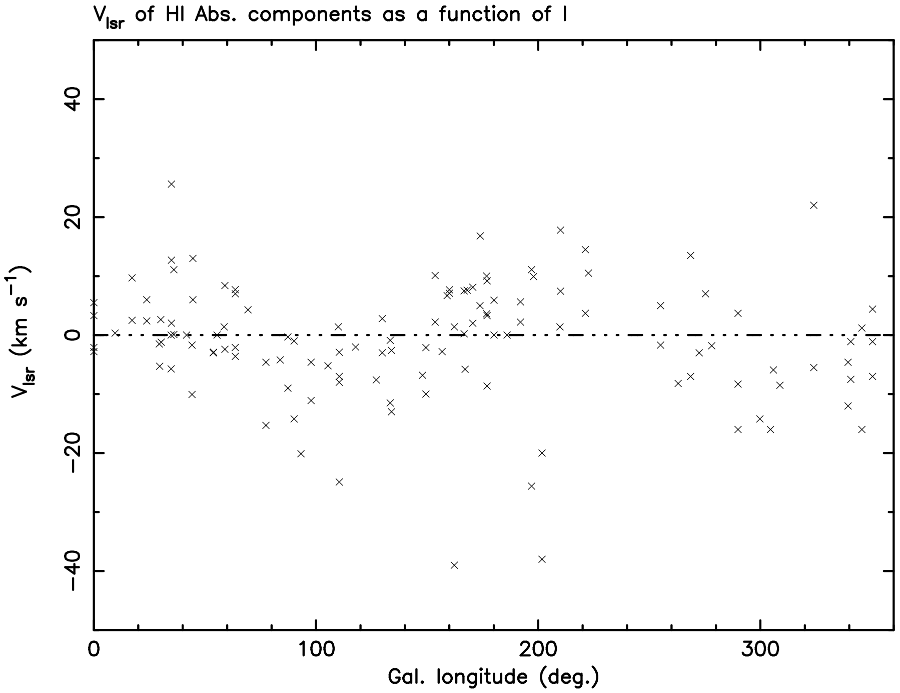

Fig. 3.19 The Radial velocity (in the LSR frame) of the HI absorption features plotted as a function of Galactic longitude

3.6.3 Differential Galactic rotation

In Figure 3.19 we have plotted the radial velocities with respect to the LSR of the various HI absorption features as a function of the Galactic longitude. If the contribution to radial velocities from the Galactic differential rotation is dominant, then there should be pronounced signature of a "sine wave" in such a plot. As may be seen, it is rather difficult to conclude anything definitive from this figure. There is a suggestion that absorption at $|V_{lsr}| \lesssim 15$ km s^{-1} may have significant contribution from the differential rotation. The larger velocity features have a larger scatter. This would point to the larger velocities being due to peculiar or random motions.

For a given Galactic longitude "l" and latitude "b", the observed radial component of differential Galactic rotation for objects in the Solar neighbourhood is (Burton, 1988)

$$v_{\rm r} = Ar \; sin \; 2l \;\; cos \; b \tag{3.12}$$

where, A = 14 km s^{-1} Kpc^{-1} is the Oort's constant and r is the heliocentric distance to the object. Including an additional term for the random motion of the cloud, the above equation becomes

$$v_{\rm r} = v_{\rm random} \ + \ Ar \ sin \ 2l \ \ cos \ b \tag{3.13}$$

It would appear that this function can be fitted to the observed distribution (Fig 3.19) to estimate the systematic component. However, the distances to the absorbing features are unknown. Consider a collection of interstellar clouds, each with its own random motion and distance. The random motions can be considered as a gaussian distribution with a velocity dispersion around zero mean. The distances for a distribution of clouds in the Galaxy can be assumed to be an exponential deviate with a scale height. Adding these two terms, the above equation can be re-written as

$$v_{\rm r} = a_1 v_{\rm gauss} \ + \ a_2 \left(\frac{z_{\rm exp}}{|sin \ b|} \right) \ sin \ 2l \ \ cos \ b \tag{3.14}$$

Where $z_{\rm exp}$ is an Exponential distribution and $v_{\rm gauss}$ is a Gaussian distribution. The term $z_{\rm exp}/|sin \ b|$ is to take into account the variation of pathlength through the disk as a function of the Galactic latitude "b''. We have carried out a monte-carlo simulation to generate such a distribution and compare with the observed values given in Fig. 3.19. The simulation used the monte carlo routines discussed by Press et al (1992). A non-linear least square fit was carried out on the simulated data to extract the best fit values for a_1 and a_2 (Levenberg-Marquardt method; Press et al, 1992). Such an exercise will provide a value for the random velocity distribution as well as the scale height of the absorbing gas, the two very important unknown parameters. The fitted values were:

a_1 = 9.8 ± 0.1 km $\rm s^{-1}$
a_2 = 0.7 ± 0.9 km $\rm s^{-1}$

The best fit simulated data and the observed data are shown in Fig. 3.20. Notice that the best fit parameter for the systematic feature a_2, is small, with large error bar in the estimate. To validate the fit results one has to check if the two sets (the best fit obtained by simulating the data and the observed data) can be drawn from the same distribution. We used the $F - test$ (Press et al, 1992) to check this hypothesis. The results from this test are shown in Fig. 3.21. The figure shows the iso-probability ellipses for the two sets to be derived from the same distribution, as a function of the two parameters a_1 and a_2. The plus sign mark the best fit values of the two parameters, from the least-square fit. The cross sign marks the values of the two parameters for the highest probability event. However, notice that the figure indicates clearly that there is no well defined peak for the probability distribution. The 3σ level indicate that similar confidence levels can be achieved even with a_1 or a_2 = 0.0. Therefore, the $F - test$ results imply that a systematic pattern in the distribution is negligible. Hence, we have not applied any correction for differential Galactic rotation velocity for the data to study the random velocity distribution.

It may be recalled that in the pioneering study by Blaauw (1952), he was able to estimate the contribution due to the differential rotation and subtract it to obtain the random velocities. This was possible because one knew the distance to the star, and hence make a guess about the distance to the absorbing cloud. In our study, since the

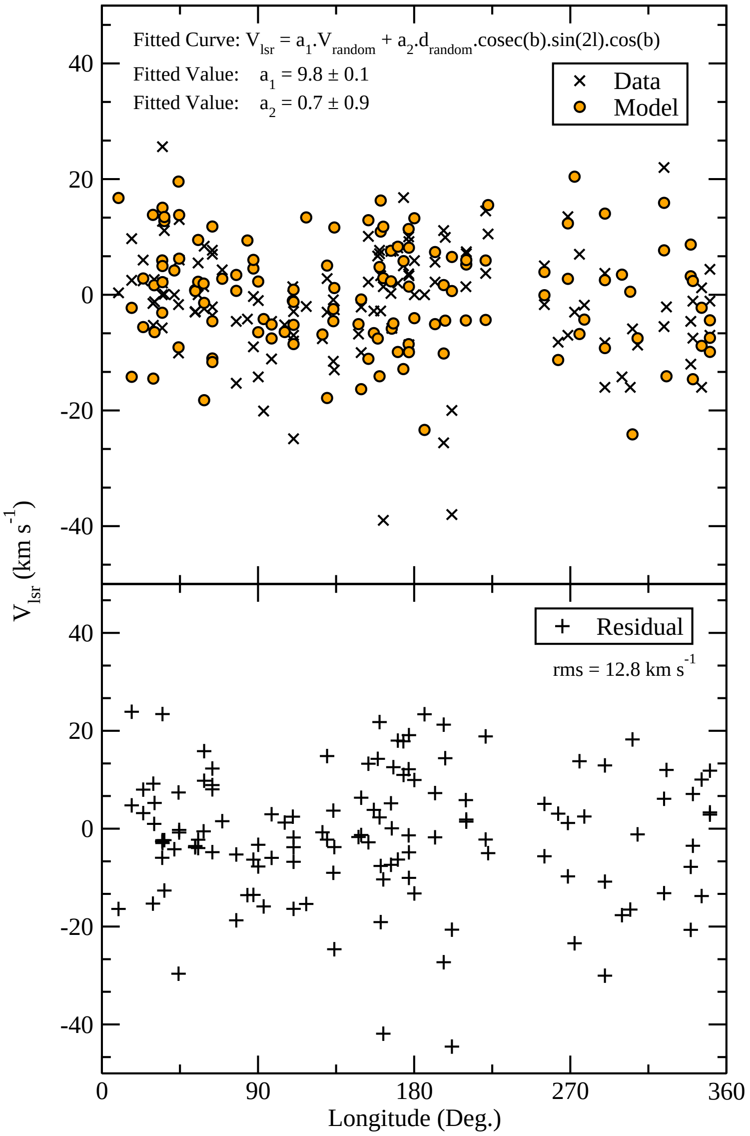

Fig. 3.20 The radial velocity (in the LSR frame) of the HI absorption features plotted as a function of Galactic longitude. The crosses denote the observed data points and the circles are from the best fit function from the simulated data.

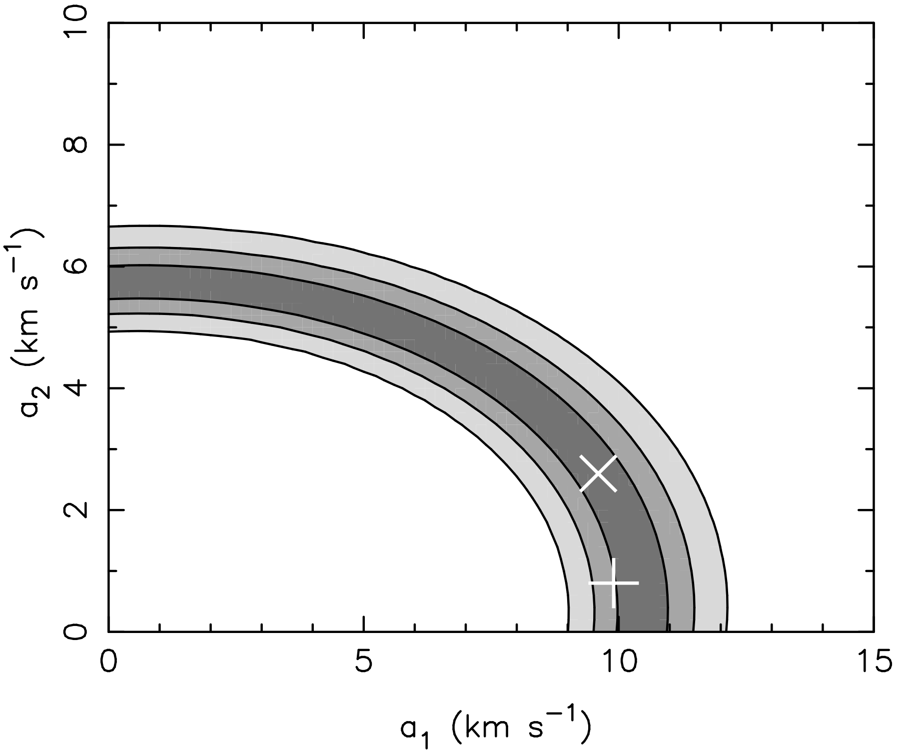

Fig. 3.21 The iso-probability ellipses from the $F - test$. The cross marks the point of highest probability (From $F - test$), and the plus mark the best fit values of a_1 and a_2 (from the least square fit) for the simulated distribution in Fig. 3.20. There is no well defined peak for the probability distribution. The 3σ level indicate that similar confidence levels can be achieved even with a_1 or a_2 = 0.0.

radio sources are extragalactic, there is no simple way to estimate the distances to the clouds.

3.6.4 The High velocity HI absorption features

The basic motivation for the observations discussed in the present chapter is the search for higher velocity ($|v| \gtrsim$ 15 km s^{-1}) HI absorption features in the ISM. We have detected 13 such features (Table 3.5) The mean value for the derived spin temperature is $\sim$ 126K. However, the estimates for HI spin temperatures are prone to uncertainties because of the different resolutions used for the HI absorption data (GMRT) and the HI emission data (Obtained from the LDS, using the Dwingeloo telescope).

The mean value of the spin temperatures of the clouds we have detected in absorption is $\sim$120 K. This would suggest that there isn't much difference between the slower and faster clouds at least as far as their spin temperatures are concerned. The tentative conclusion one can draw at this stage is that the much smaller optical depths of the faster clouds might be solely due to their smaller column densities.

We have carried out a gaussian fit to the observed frequency distribution of radial velocities of the HI absorption features detected in the present study. A non-linear least square fit method was used to fit gaussians to this cumulative histogram. A single gaussian fit was not adequate and the resulting reduced chi-square value was 2.498. The fitted gaussian had a dispersion of $\sim$8 km s^{-1}. Infact it is evident from Figure 3.8 that a single gaussian model is not sufficient for this distribution. A two gaussian model was found to be a good fit for the distribution, with a reduced chi-square value 1.375. The low velocity features were found to form a gaussian distribution with dispersion, σ $\sim$7.6 $\pm$ 0.3 km s^{-1}, which agrees well with the available values. For eg., Belfort & Crovisier, (1984) had performed a statistical analysis of radial velocities of HI clouds observed by surveys using the Arecibo (Dickey et al, 1978), and Efelesberg & Greenbank (Mebold et al, 1982). The value for the velocity dispersion of HI clouds were found to be $\sim$6.9 km s^{-1}. In addition, the higher velocity features in the present survey seem to form a distribution with velocity dispersion, σ_v = 21 $\pm$ 4 km s^{-1} (Fig. 3.22).

Recent HI emission studies using the Greenbank telescope (GBT) by Lockman (2002) has led to the discovery of a population of discrete HI clouds in the lower Galactic halo. The HI column density of these clouds were estimated to be a few times 10^{19} cm^{-2}, with considerable scatter around the mean value. He concludes that a cloud population with a line of sight velocity dispersion, $\sigma_v \sim$ 15 – 20 km s^{-1} is capable of explaining the observed velocity spread of these features. An upper limit for the temperature of these features can be obtained from the HI emission line widths. Lockman (2002) finds that many clouds in the halo have narrow line widths implying temperatures below 1000K. The GBT Observations also gives clear indication that higher spatial resolution (GBT is a 110 meter single dish, as compared to

Table 3.5 The higher velocity ($|v| \gtrsim 15$ km s^{-1}) HI absorption features detected in the present study. The mean value for the derived spin temperature is $\sim$ 126K.

Source	l (deg)	b (deg)	τ_{HI}	V$_{lsr}$ (km s^{-1})	FWHM (km s^{-1})	T$_B$ (K)	V$_{lsr}$ (km s^{-1})	FWHM (km s^{-1})	N$_{HI}$ $\times 10^{19}$ cm^{-2}	T$_{Spin}$ (K)
J0459+024	197.01	–23.34	0.026(0.004)	–25.6(0.5)	4.6(0.8)	0.21(0.08)	–28(1)	6(3)	0.2	8(4)
J0541–056	210.05	–18.11	0.069(0.007)	+17.8(0.9)	3.2(0.5)	—	—	—	—	
J0814+459	173.90	+33.17	0.035(0.002)	+16.8(0.9)	4(2)	9.5(0.5)	+15.4(0.1)	3.8(0.1)	6.6	276
J1154–350	289.93	+26.34	0.016(0.003)	–16(2)	13(5)	—	—	—	—	
J1221+282	201.74	+83.29	$\sim$0.01	–20	–	0.47(0.04)	–13.9(0.4)	11(1)	0.9	47
J1221+282	201.74	+83.29	$\sim$0.02	–38	–	1.06(0.04)	–34.8(0.1)	6.1(0.3)	1.2	53
J1257–319	304.55	+30.93	0.108(0.006)	–16.0(0.2)	3.8(0.3)	—	—	—	—	
J1351–148	324.03	+45.56	0.020(0.004)	+22.0(0.6)	5(1)	5.7(0.1)	+22.9(0.1)	10.5(0.2)	10.9	285
J1554–270	345.68	+20.27	0.04(0.02)	–16(8)	8(5)	—	—	—	—	
J1638+625	93.22	+39.01	0.028(0.004)	–20.1(0.4)	5(1)	4.50(0.06)	–21.05(0.02)	5.05(0.07)	4.1	161
J1751+096	34.92	17.65	0.066(0.003)	+25.6(0.2)	4.6(0.2)	3.9(0.1)	+25.1(0.1)	7.1(0.3)	5.0	61
J2005+778	110.46	22.73	0.05(0.01)	–25(4)	2(2)	7.2(0.3)	–23.59(0.08)	7.4(0.2)	9.7	148
J2232+117	77.44	–38.58	0.040(0.004)	–15.3(0.3)	2.9(0.7)	3.83(0.07)	–13.88(0.03)	3.92(0.08)	2.7	96

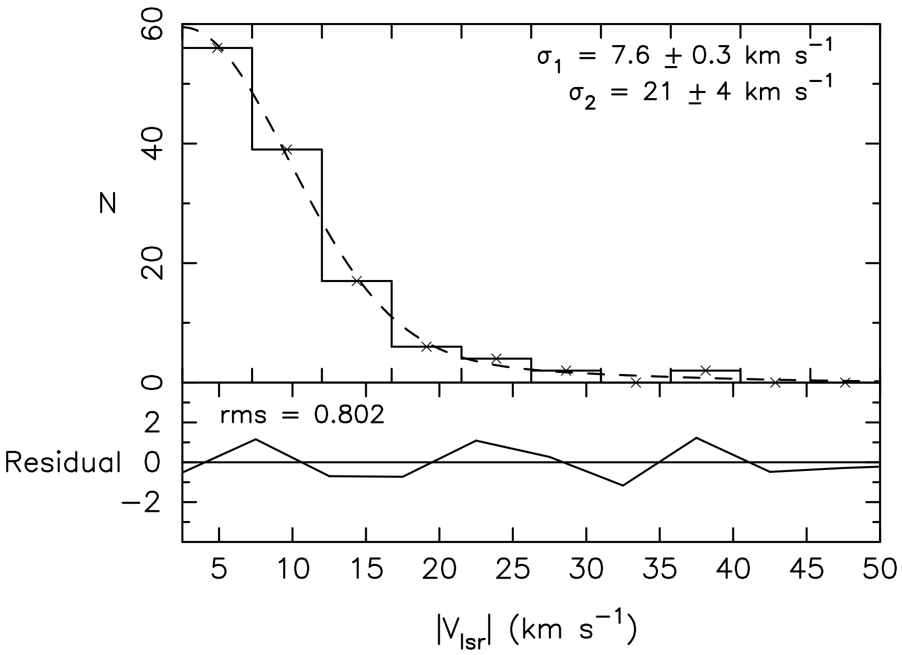

Fig. 3.22 The frequency distribution of LSR velocities of HI absorption components towards radio continuum sources from the present survey. The dashed line is the fitted distribution, two gaussian components with σ_1 = 7.6 ± 0.3 km s^{-1} and σ_2 = 21 ± 4 km s^{-1}, overlapped on the histogram. The lower panel shows the residual after subtracting the fitted model from the observed distribution.

the 25 meter Dwingeloo telescope) is required to obtain a better estimate for the HI brightness temperature and thereby the column density. In addition, indications for a core-halo structure for these clouds was also found. Therefore, it is possible for these clouds to have a cold core surrounded by a warmer halo.

The estimate of velocity dispersion of the higher velocity features detected in the present survey is in agreement with the results from Lockman (2002). Therefore, we conclude that these features with large peculiar motions form a subset of the HI cloud population discovered by Lockman. Our HI absorption study has picked up the low temperature clouds from a much larger population of high velocity dispersion HI clouds in the lower Galactic halo.

The peak value for the gaussian corresponding to the higher velocity features was found to be ∼4 and that of the low velocity features was found to be ∼55. From the area under the respective curves, this data imply that ∼20% of the clouds belong to the second population, with larger velocity dispersion. We wish to point out that HI observations of several nearby galaxies reveal the presence of a faint, extended, and kinematically anomalous component. This shows up in the HI line profiles as extended wings of emission toward the systemic velocity. In the central regions these wings are very broad (up to 150 km s^{-1}) and often indicate large deviations from circular motion. The anomalous gas component is distinct and separate from the cold disk and follows a separate rotation curve. The mass of the anomalous component ranges from ∼10% to 20% of the total HI mass. The picture emerging from these observations is that in many galaxies, a cold HI disk is surrounded by a thick and clumpy HI layer characterized by slower rotation. The origin of this anomalous gas layer is, however, unclear. (See Sancisi, 2001 and the references therein). The last few years have in fact brought new insight into the disk-halo connection in spiral galaxies. Chandra and HI observations of nearly edge-on galaxies have shown that the halo is far from empty, but it contains, compared to the disk, a substantial amount of gas (Fraternali et al., 2002). It is still unclear how exactly this gas is brought into the halo.

3.6.5 The HI Column density of the high velocity features

As we mentioned earlier, the Dwingeloo data has an angular resolution of $\sim 36^{'}$, as compared to the synthesized beam width of few arc seconds for the GMRT data (HI absorption). Hence, there are obvious uncertainties in the correspondence between HI emission and absorption spectra. In addition, some of the high velocity features were seen towards southern sources, towards which the Dwingeloo data is not available (Table 3.5). Therefore we have decided to estimate the HI column density of the higher velocity clouds independently, without using the Dwingeloo HI emission data. Recall that in the previous chapter, the mean spin temperature of the high random velocity clouds detected in HI absorption is $\sim$ 70K. The mean value for the HI spin temperature derived from the data obtained in the present survey is $\sim$ 126K, both are consistent with the inferred temperatures of the cold diffuse clouds. We have calculated the expected HI line brightness temperature assuming a temperature of 80K (Using equation 3.10), which is the median value for the observed spin temperature of the cold neutral gas (Spitzer, 1978) and thus obtain an estimate of the column density of the absorbing gas using the relation

$$N_{HI} = 1.823 \times 10^{18} \int T_B dV cm^{-2} \tag{3.15}$$

The estimated HI column density as a function of the LSR velocity is shown in fig. 3.23. The scatter in the column density is significantly lower for the large velocity features, as compared to the lower velocity clouds. All the HI absorption features at velocities above 20 km s^{-1} seem to have a column density below $\sim 3 \times 10^{19}$ cm^{-2} (assuming a spin temperature of 80K). Figure 3.24 displays the velocities of all the low column density features detected from the present survey, as a function of Galactic longitude. Interestingly, there is no signature of Galactic differential rotation, reinforcing our earlier conclusion that the higher velocities we have measured do represent random motions.

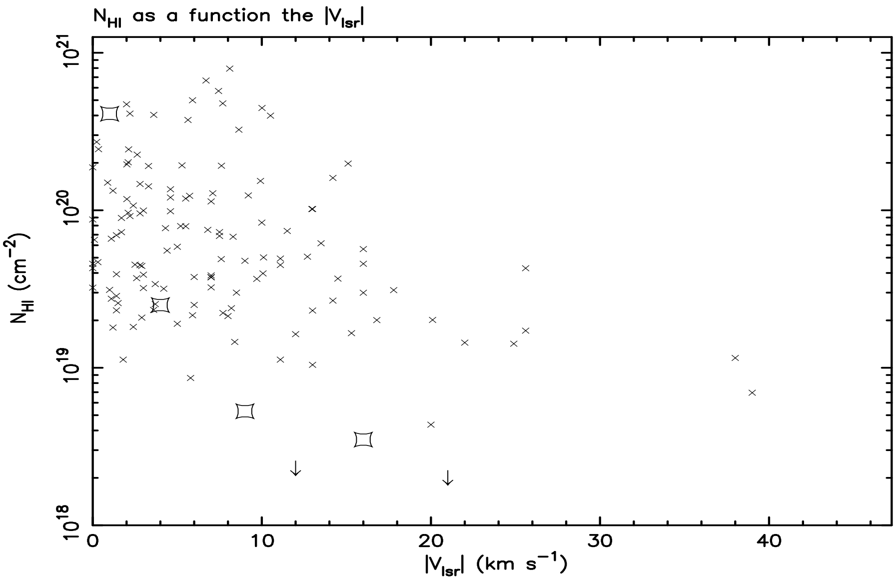

Fig. 3.23 The derived column density of the HI absorption features, assuming a spin temperature of 80K. The squares are the HI column density estimates from the UV absorption line data from Martin and York (1982). The arrows indicate the upper limit for the estimate of N_{HI} from the UV spectral line data.

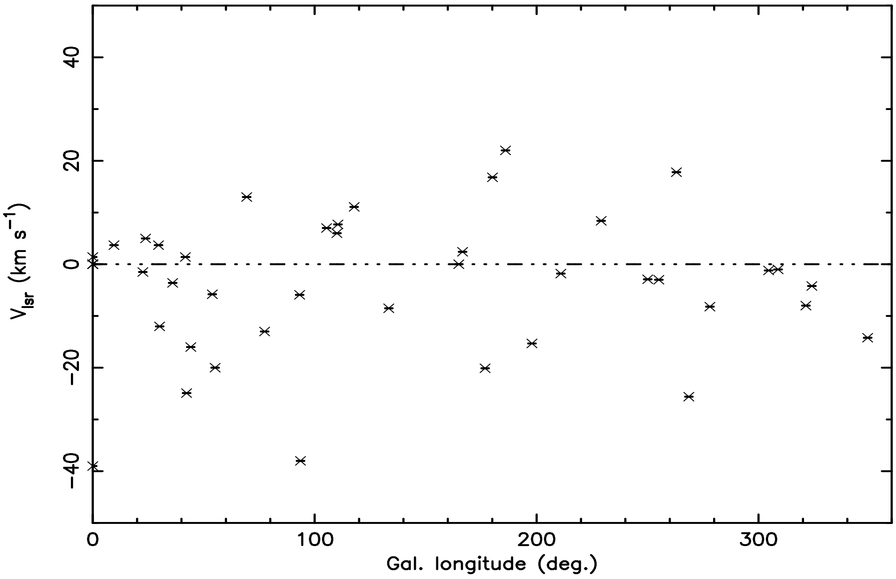

Fig. 3.24 The radial velocities of only the low column density features ($N_{HI} < 3 \times 10^{19}$, for T_S = 80K) as a function of Galactic longitude.

3.6.6 The UV spectral line studies of low HI column density features

As we mentioned earlier, the weak UV absorption lines from the interstellar space yield more reliable estimates of the HI column densities as compared to the NaI and CaII lines in the optical region. Also, since the UV absorption lines have larger oscillator strengths, they can probe smaller column densities. As for the possible correlation between higher velocities of clouds and lower HI column densities, conclusive evidence is found from the UV studies (Hobbs, 1984). Martin & York (1982) used the Copernicus data to study the radial velocity distribution of Interstellar UV absorption lines (PII, SII, ArI and NI) towards the stars ϵ and δ persei. In these two lines of sight, they find clear evidence for lower HI column density at higher velocities. For speeds above 15 km s^{-1}, the estimated HI column density was found to be below 1.0 $\times$ 10^{19} cm^{-2}. We have included the N$_{HI}$ column density estimates from Martin and York in Figure 3.23; these are marked by squares. While the UV data shows a systematic decrease in the HI column density with increasing velocity, the column density estimates from our HI absorption data shows more scatter at smaller velocities. The IUE study of interstellar absorption lines by Albert (1983) convincingly demonstrated that for high latitude lines of sight virtually all the absorption components with radial velocities $|V_{lsr}| > 10$ km s^{-1} are observed towards the more distant **halo stars**, and are not seen towards the nearby stars. All these components have lower HI column densities. This result also supports the hypothesis that the large velocity components are part of the lower Galactic halo, rather than the disk of the Galaxy.

3.6.7 Interstellar clouds in the forbidden temperature range

The diffuse atomic gas in the interstellar medium is observed to exist in different phases. These phases are believed to be in pressure equilibrium. In the widely accepted two phase model, cold diffuse clouds with a temperature $<$300 K are in pressure equilibrium with a neutral intercloud medium (the WNM), at a temperature of $\sim 10^4$ K. The warm intercloud gas is assumed to pervade the interstellar space. The mass of the HI gas is almost equally distributed into the two phases. Recently, Wolfire et al (1995) have carried out a comprehensive study of the two phase equilibrium in the interstellar medium. In short, the two phase models predict the diffuse Interstellar clouds to be at temperatures lower than $\sim$ 300 K and the warm Intercloud medium at temperatures $\gtrsim$ 5000K. In 1977, McKee & Ostriker extended the two phase model of Field, Goldsmith & Habing to a three phase model: a cold (T $\sim$80 K) neutral medium (the CNM), a warm (T $\sim$8000 K) medium, both neutral (WNM) and ionized (WIM) and a hot (T $\sim$10^6 K) ionized medium (HIM). The ISM was modelled as a dynamic system governed by supernova explosions, with a large fraction of volume filled with hot, tenuous gas. The different phases are expected to be in rough pressure equilibrium with P/k$_B$ $\sim$ 10^3 - 10^4 K cm^{-3}. The multiphase models also predict the temperatures of the cold diffuse clouds to be below $\sim$ 300K and the warm HI gas at temperatures above $\sim$ 8000K. Any gas in a temperature range between these two values ($\sim$ 300K – $\sim$5000K) will be unstable according to both the two phase model as well as the multiphase model. This temperature range would, for example, imply absence of pressure equilibrium.

As we discussed earlier, A combination of HI absorption and emission data can be used to estimate the spin temperature of the gas (equation 3.16).

$$T_s(\nu) = \frac{T_B(\nu)}{(1 - e^{-\tau_\nu})} \tag{3.16}$$

If HI absorption is not detected from a cloud, the above equation provides a lower limit for the spin temperature of the gas.

An upper limit for the kinetic temperature of the gas can be obtained from the line width, using the Doppler formula (equation 3.17). For the case of HI 21cm-line, the observed line width is primarily due to turbulence and thermal broadening. Hence if the turbulence is assumed to be minimum, **the width of the line** is entirely due to thermal broadening, which gives **the maximum possible temperature for a cloud**.

$$T_k \leq \frac{m}{2k_B}\left[\frac{\Delta v}{2\sqrt{ln2}}\right]^2 \tag{3.17}$$

Where m is the mass of the emitting ion/atom, Δv is the width of the spectral line and k_B is the Boltzmann's constant. It is evident from Appendix B that the number of discrete components identified in the HI emission profiles are much larger than those in the HI optical depth profiles. The present survey has a mean rms optical depth limit of $\sim$ 0.003, which is not adequate to detect HI absorption in the intercloud medium (we shall discuss in chapter 5 a separate attempt to detect this). The HI emission from this warm gas is prominent in almost all the directions. We have used the above two equations to estimate the temperature range of those features which are detected in HI emission, but **not** seen in absorption. **A lower limit for spin temperature is obtained from the absence of HI absorption in the GMRT data, and the upper limit for kinetic temperature is calculated from the emission line widths**.

There are 18 HI emission features, with no corresponding HI absorption, implying spin temperatures above $\sim$ 350K. The HI emission line widths imply kinetic temperatures below $\sim$ 5000K (Table 3.6). We would like to emphasize that this analysis only provides weak limits for the temperature of the gas. The fact that HI emission and absorption data were obtained at different spatial resolution adds more uncertainty to the analysis. However, the existence of such features, though a small fraction of the entire dataset (18 out of the $\sim$ 500 discrete HI emission features, $\sim$4%) indicate the possible existence of gas in the unstable phase of the ISM. No information about the distance to these clouds can be obtained from the present dataset. The gas is known to exist at such temperatures in the Galactic halo (Giovanelli & Brown, 1973).

Table 3.6 The HI emission features in the "forbidden temperature range", identified from the present study. The lower limit for spin temperature is obtained from the lack of HI absorption in the GMRT data and the upper limit for kinetic temperature is calculated from the line widths.

Source	l (deg)	b (deg)	T_B (K)	FWHM (km s^{-1})	T_{Spin} (K)	T_K (K)
J0025–260	42.27	–84.17	2.8(0.1)	13.3(0.3)	> 311	< 3866
J0059+001	127.11	–62.70	5.14(0.08)	14.9(0.2)	> 428	< 4852
J0119+321	129.83	–30.31	5.7(0.1)	15.3(0.4)	> 633	< 5116
J0240–231	209.79	–65.13	4.9(0.1)	9.5(0.1)	> 544	< 1972
J0453–281	229.09	–37.02	4.3(0.2)	11.9(0.4)	> 358	< 3095
J0854+201	206.81	+35.82	4.7(0.1)	14.1(0.3)	> 783	< 4345
J1057–245	272.47	+31.51	5.9(0.3)	14.4(0.4)	> 492	< 4532
J1120–251	278.09	+33.30	4.9(0.9)	6.9(0.4)	> 544	< 1040
J1344+141	349.16	+72.09	3.20(0.06)	12.7(0.2)	> 356	< 3525
J1445+099	5.79	+58.17	3.44(0.04)	5.14(0.07)	> 573	< 577
J1554–270	345.68	+20.27	3.7 (0.4)	9(1)	> 411	< 1770
J1602+334	53.73	+48.71	3.11(0.06)	16.0(0.2)	> 518	< 4595
J1634+627	93.61	+39.38	2.73(0.05)	6.1(0.1)	> 455	< 813
J1751+096	34.92	+17.65	3.4(0.1)	8.3(0.3)	> 378	< 1505
J1800+784	110.04	+29.07	4.41(0.06)	7.7(0.2)	> 404	< 1295
J1845+401	69.36	+18.21	3.2(0.1)	9.2(0.4)	> 356	< 1850
J2232+117	77.44	–38.58	6.4(0.4)	5.9(0.3)	> 711	< 761
J2250+143	83.89	–39.20	2.01(0.05)	5.20(0.2)	> 335	< 591

Recent HI absorption/emission measurements using the Arecibo Radio Telescope by Heiles & Troland (2002a, 2002b) has also indicated gas in the 'forbidden temperature' range. They found at least 48% of the Warm neutral medium to exist in the thermally unstable phase. One should keep in mind that a large single dish telescope like the Arecibo is far superior for such an experiment, where the HI emission and absorption data are available at the same spatial resolution.

3.7 SUMMARY AND CONCLUSIONS

In this chapter, we have described the results of our absorption studies at high Galactic latitudes using the GMRT. This is the most sensitive survey to date. In all, HI absorption was measured towards 104 radio sources. An rms of 0.003 was achieved in optical depth.

We have separately compared our results with those obtained in earlier studies, in particular the distribution of radial velocities of the absorbing clouds with respect to the local standard of rest. Unfortunately, there is no simple way to remove the contribution to the radial velocity due to galactic differential rotation.

The main results and conclusions of this study are summarized below:

- **We have studied the distribution of radial velocities, optical depths and line widths of the absorbing clouds.**
- **The present survey is at least a factor of 5 more sensitive than the earlier interferometric absorption studies.**
- **We detected approximately 120 absorption features.**
- **of these, 13 were at velocities greater than 15 km s^{-1}. If these truly represent *random velocities* then this is a significant contribution.**
- **We find that the higher velocity absorptions have smaller optical depths, as suspected by Rajagopal et al. (1998b).**
- **The (inverse) correlation between the velocity and column density is also clearly seen in the ultraviolet absorption studies.**
- **The histogram of velocities cannot be fit with a single gaussian, as was noted long ago by Blaauw.**
- **But the two gaussians, one with a dispersion of $\sim$7 km s^{-1} and another with a dispersion of $\sim$21 km s^{-1}, will account for the high velocity tail.**
- **While the significance of the wider gaussian is not clear, it is consistent with the recent conclusion by Lockman (2002).**

- **It might be that the narrow gaussian corresponds to the clouds in the disk of the Galaxy, and the wider gaussian represents a population of clouds in the galactic halo (as conjectured by Lockman, 2002).**

To conclude, the results from our observations clearly show the presence of a higher velocity tail for the velocity dispersion of radial velocities of Interstellar clouds. Although it is difficult to estimate the distance to these clouds, there is an indication that these clouds are located in the lower Galactic halo. In the light of this results, we wish to address one longstanding and important problem. The controversial detection of a wide HI absorption line towards the Galactic center by Radhakrishnan and Sarma (1980), followed by the non-detection by Schwarz et al., (1982). The next chapter of this thesis address this issue, where we discuss the results of our observations using the Australia Telescope Compact Array to image the Galactic center and the Westerbork Synthesis Radio Telescope to measure HI absorption towards the Galactic anticenter.

REFERENCES

1. Adams, W. A., 1949, Astrophys. J., 109, 354.
2. Albert, C.E., 1983, Astrophys. J., 272, 509.
3. Anantharamaiah, K.R., Radhakrishnan, V., Shaver, P.A., 1984, Astron. Astrophys., 138, 131.
4. Blaauw, A., 1952, Bull. Astr. Inst. Netherland., 11, 459.
5. Brand, J., Blitz, L., 1993, Astr. Astrophys., 275, 67.
6. Burton, W.B., 1988 in Galactic and Extragalactic Radio Astronomy,
7. eds. G.L. Verschuur & K.I. Kellermann (New York: Springer-Verlag), 295.
8. Clark, B.G., 1965, Astrophys. J., 142, 1398.
9. Crovisier, J., 1978, Astron. Astrophys., 70, 43.
10. Belfort, P., Crovisier, J., Astron. Astrophys., 136, 368.
11. Dickey, J.M., Terzian, Y., Salpeter, E.E., 1978, Astrophys. J. Suppl., 36, 77.
12. Dickey, J. M., Kulkarni, S.R., Heiles, C.E., van Gorkom, J. H., 1983, Astrophys. J. Suppl., 53, 591.
13. English, J., et al., 1998, Publ. Astron. Soc. Aus., 15, 56.
14. Field, G.B., Goldsmith, D.W., Habing, H.J., 1969, Astrophys. J.Lett., 155, L149.

15. Fraternali, F., van Moorsel, G., Sancisi, R., Oosterloo, T., 2002, Astron. J., 123, 3124.
16. Gibson, S.J., Taylor, A.R., Higgs, L.A., Dewdney, P.E., 2000, Astrophys. J., 540, 851.
17. Giovanelli, R., Brown, R.L., 1973, Astrophys. J., 182, 755.
18. Goldstein, S. J., MacDonald, D. D., 1969, Astrophys. J., 157, 1101.
19. Habing, H. J., 1968, Bull. Astr. Inst. Netherland., 20, 120.
20. Habing, H. J., 1969, Bull. Astr. Inst. Netherland., 20, 171.
21. Hartmann, D., Burton, W. B., 1995, An Atlas of Galactic Neutral Hydrogen, Cambridge Univ. Press.
22. Heiles, C., Troland, T.H., 2002, eprint arXiv:astro-ph/0207104
23. Heiles, C., Troland, T.H., 2002, eprint arXiv:astro-ph/0207105
24. Hobbs, L.M., 1969, Astrophys. J., 157, 135.
25. Hobbs, L.M., 1984, Astrophys. J. Suppl., 56, 315.
26. Mckee, C.F., Ostriker, J.P., 1977, Astrophys. J., 218, 148.
27. Kalberla, P.M.W., Westphalen, G., Mebold, U., Hartmann, D., Burton, W.B., 1998, Astron. Astrophys. Lett. 332, L61.
28. Kulkarni, S. R., Fich, M., 1985, Astrophys. J., 289, 792.
29. Lockman, F.J., 2002, Astrophys. J. Lett., 580, L47.
30. Martin, E.R., York, D.G., 1982, Astrophys. J., 257, 135.
31. Mebold, U., Winnberg, A., Kalberla, P.M.W., Goss, W.M., 1981, Astron. Astrophys. Suppl., 46, 389.
32. Mebold, U., Winnberg, A., Kalberla, P.M.W., Goss, W.M., 1982, Astron. Astrophys., 115, 223.
33. Münch, G., 1957, Astrophys. J., 125, 42.
34. Münch, G., Zirrin, H., 1961, Astrophys. J., 133, 11.
35. Press, W.H., Teukolsky, S.A., Vetterling, W.T., Flannery, B.P., 192,
36. Numerical Recipes, The Art of Scientific Computing, Cambridge Univ. Press,
37. Cambridge.

38. Radhakrishnan, V., Goss, W.M., Murray, J.D., Brooks, J.W., 1972, Astrophys. J. Suppl., 24, 49.

39. Radhakrishnan, V., Sarma, N. V. G., 1980, Astron. Astrophys., 85, 249.

40. Radhakrishnan, V., Srinivasan, G., 1980, J. Astrophys. Astr., 1, 47.

41. Rajagopal J., Srinivasan, G., Dwarakanath, K. S., 1998a, J. Astrophys. Astr., 19, 97.

42. Rajagopal J., Srinivasan, G., Dwarakanath, K. S., 1998b, J. Astrophys. Astr., 19, 117.

43. Routly, P. M., Spitzer, L. Jr., 1952, Astrophys. J., 115, 227.

44. Sancisi, R., Fraternali, F., Oosterloo, T., van Moorsel, G., 2001, in Gas and Galaxy Evolution, ASP Conf. Proc., Vol. 240, eds. J.E. Hibbard, M. Rupen and J.H. VanGorkhom, San Francisco: Astron. Soc. of Pacific., pp. 241

45. Siluk, R.S., Silk, J., 1974, Astrophys. J., 192, 51.

46. Spitzer, L. Jr., 1956, Astrophys. J., 124, 20.

47. Spitzer, L. Jr., 1968, in Nebulae and Interstellar matter, Vol. 7, eds. B.M. Middlehurst and L.H. Aller, Chicago:Univ. of Chicago Press., pp. 1-64.

48. Spitzer, L. Jr., 1978, Physical Processes in the Interstellar Medium., New York:Wiley Interscience.

49. Schwarz, U. J., Ekers, R. D., Goss, W. M., 1982, Astron. Astrophys., 110, 100.

50. Swarup, G., Ananthakrishnan, S., Kapahi, V. K., Rao, A. P., Subrahmanya, C. R., Kulkarni, V. K., 1991, Current Science, 60, 95.

51. Wakker, B.P., van Woerden, H., 1991, Astron. Astrophys., 250, 509.

52. Welty, D. E., Hobbs, L. M., Kulkarni, V.P., 1994, Astrophys. J., 436, 152.

53. Welty, D. E., Morton D. C., Hobbs, L. M., 1996, Astrophys. J.Suppl., 106, 533.

54. Wolfire, M.G., Hollenbach, D., McKee, C.F., Tielens, A.G.G.M., Bakes, E.L.O., 1995, Astrophys. J., 443, 152.

Appendix A: The Spectra

In this Appendix, we present the HI optical depth profiles obtained from the high latitude Galactic HI absorption survey using the GMRT along with the HI emission profiles in the respective lines of sight from the Leiden-Dwingeloo survey of Galactic Neutral hydrogen (if available). The figures are arranged in order of increasing Right Ascension. The spectra are labeled by the radio continuum source name in J2000.0 co-ordinates (top left) and its Galactic co-ordinates (top right).

For each of the figures, the HI emission profile from the Leiden-Dwingeloo Survey is shown in the top panel and the HI optical depth profile from the GMRT is shown in the middle panel. The lower panel is the Galactic rotation curve for the given line of sight. The heliocentric distance as a function of radial velocity is labelled on the left of the panel and the corresponding height above the mid-plane of the Galaxy is labelled on the right side.

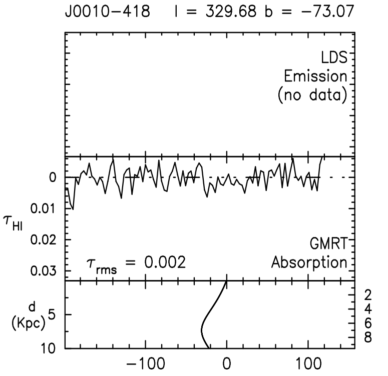

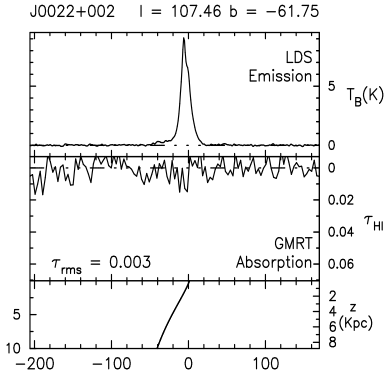

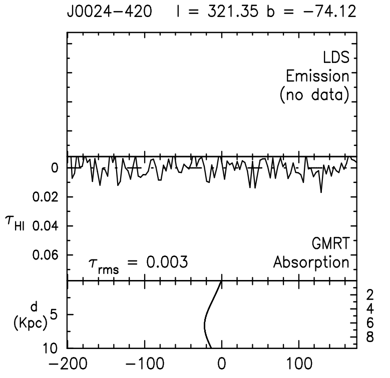

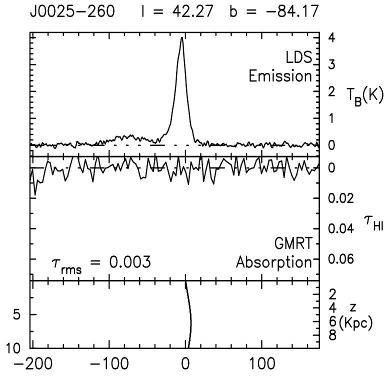

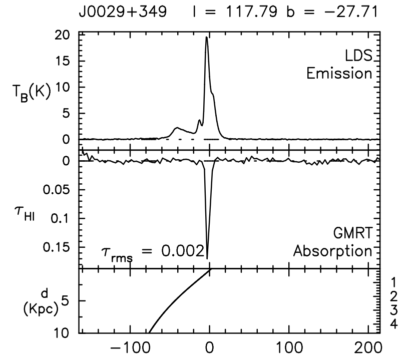
J0029+349 l = 117.79 b = −27.71
T_B(K)
LDS Emission
τ_{HI}
GMRT Absorption
τ_{rms} = 0.002
d (Kpc)
−100 0 100 200

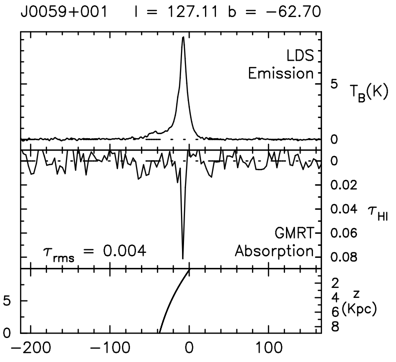
J0059+001 l = 127.11 b = −62.70
T_B(K)
LDS Emission
τ_{HI}
GMRT Absorption
τ_{rms} = 0.004
z (Kpc)
−200 −100 0 100

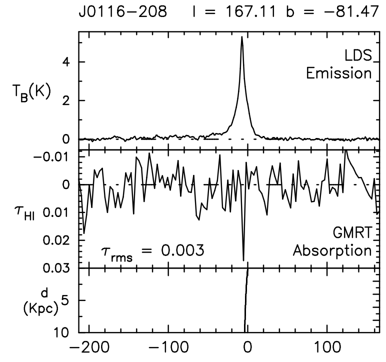
J0116−208 l = 167.11 b = −81.47
T_B(K)
LDS Emission
τ_{HI}
GMRT Absorption
τ_{rms} = 0.003
d (Kpc)
−200 −100 0 100

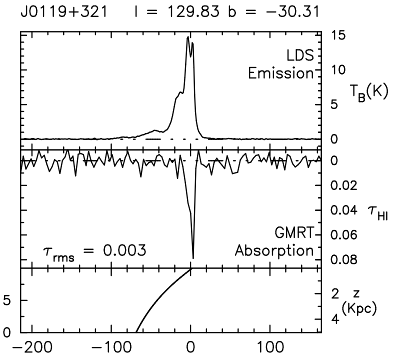
J0119+321 l = 129.83 b = −30.31
T_B(K)
LDS Emission
τ_{HI}
GMRT Absorption
τ_{rms} = 0.003
z (Kpc)
−200 −100 0 100

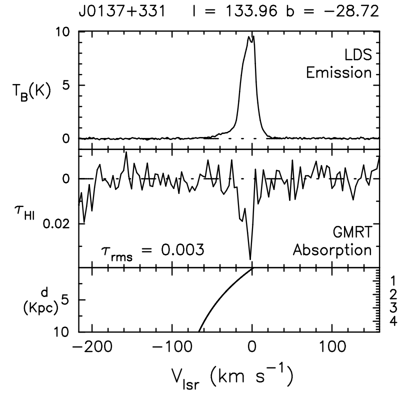
J0137+331 l = 133.96 b = −28.72
T_B(K)
LDS Emission
τ_{HI}
GMRT Absorption
τ_{rms} = 0.003
d (Kpc)
−200 −100 0 100
V_{lsr} (km s^{-1})

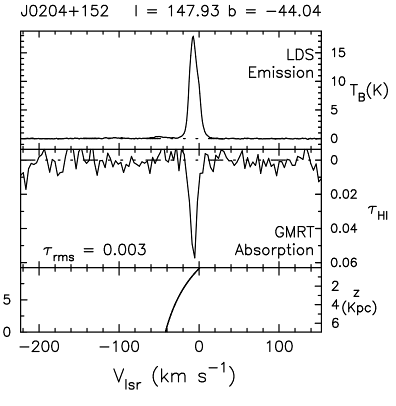
J0204+152 l = 147.93 b = −44.04
T_B(K)
LDS Emission
τ_{HI}
GMRT Absorption
τ_{rms} = 0.003
z (Kpc)
−200 −100 0 100
V_{lsr} (km s^{-1})

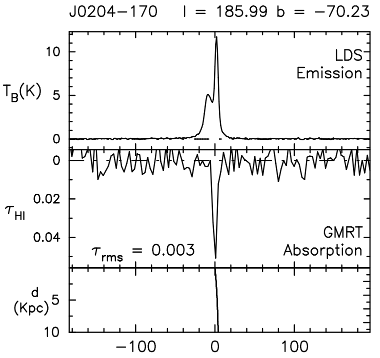
J0204−170 l = 185.99 b = −70.23
LDS Emission
T_B(K)
0
5
10
τ_{HI}
0
0.02
0.04
GMRT Absorption
τ_{rms} = 0.003
d (Kpc)
5
10
2
4
6
8
−100
0
100

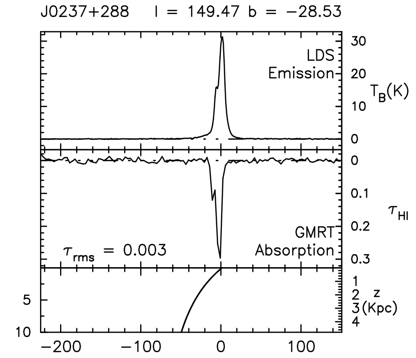
J0237+288 l = 149.47 b = −28.53
LDS Emission
T_B(K)
0
10
20
30
τ_{HI}
0
0.1
0.2
0.3
GMRT Absorption
τ_{rms} = 0.003
5
10
1
2
3
4
z (Kpc)
−200
−100
0
100

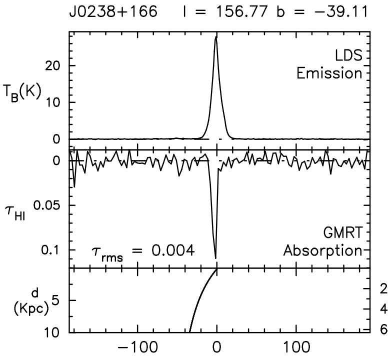
J0238+166 l = 156.77 b = −39.11
LDS Emission
T_B(K)
0
10
20
τ_{HI}
0
0.05
0.1
GMRT Absorption
τ_{rms} = 0.004
d (Kpc)
5
10
2
4
6
−100
0
100

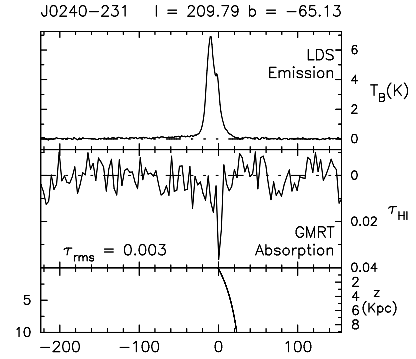
J0240−231 l = 209.79 b = −65.13
LDS Emission
T_B(K)
0
2
4
6
τ_{HI}
0
0.02
0.04
GMRT Absorption
τ_{rms} = 0.003
5
10
2
4
6
8
z (Kpc)
−200
−100
0
100

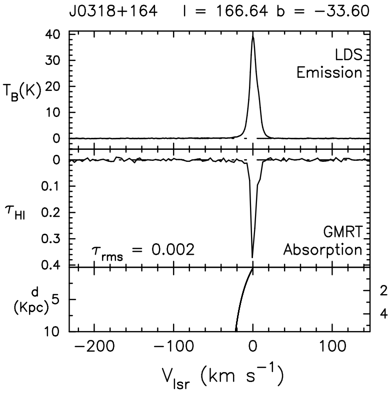
J0318+164 l = 166.64 b = −33.60
LDS Emission
T_B(K)
0
10
20
30
40
τ_{HI}
0
0.1
0.2
0.3
0.4
GMRT Absorption
τ_{rms} = 0.002
d (Kpc)
5
10
2
4
−200
−100
0
100
V_{lsr} (km s^{-1})

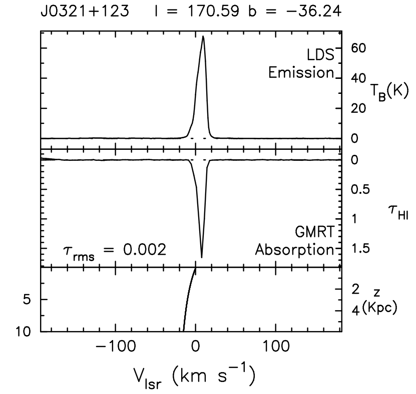
J0321+123 l = 170.59 b = −36.24
LDS Emission
T_B(K)
0
20
40
60
τ_{HI}
0
0.5
1
1.5
GMRT Absorption
τ_{rms} = 0.002
5
10
2
4
z (Kpc)
−100
0
100
V_{lsr} (km s^{-1})

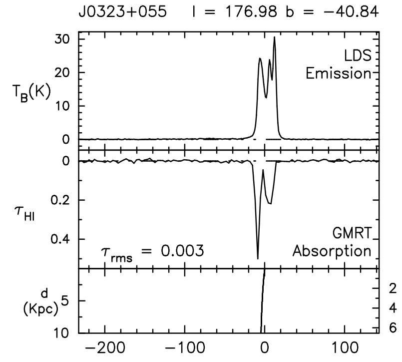
J0323+055 l = 176.98 b = −40.84
T_B(K)
LDS Emission
τ_{HI}
GMRT Absorption
τ_{rms} = 0.003
d (Kpc)
z (Kpc)
−200 −100 0 100

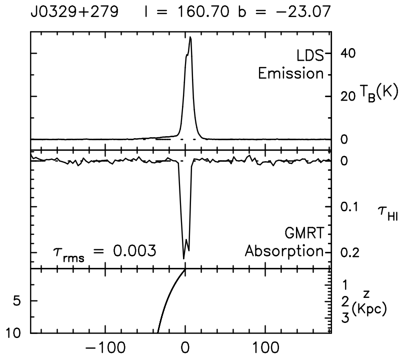
J0329+279 l = 160.70 b = −23.07
T_B(K)
LDS Emission
τ_{HI}
GMRT Absorption
τ_{rms} = 0.003
d (Kpc)
z (Kpc)
−100 0 100

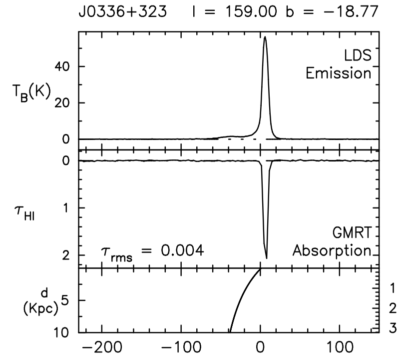
J0336+323 l = 159.00 b = −18.77
T_B(K)
LDS Emission
τ_{HI}
GMRT Absorption
τ_{rms} = 0.004
d (Kpc)
−200 −100 0 100

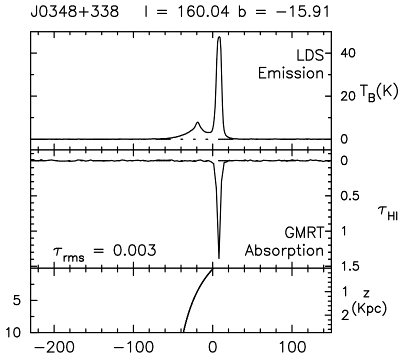
J0348+338 l = 160.04 b = −15.91
T_B(K)
LDS Emission
τ_{HI}
GMRT Absorption
τ_{rms} = 0.003
z (Kpc)
−200 −100 0 100

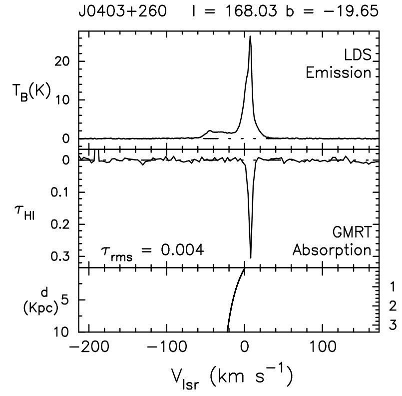
J0403+260 l = 168.03 b = −19.65
T_B(K)
LDS Emission
τ_{HI}
GMRT Absorption
τ_{rms} = 0.004
d (Kpc)
−200 −100 0 100
V_{lsr} (km s^{-1})

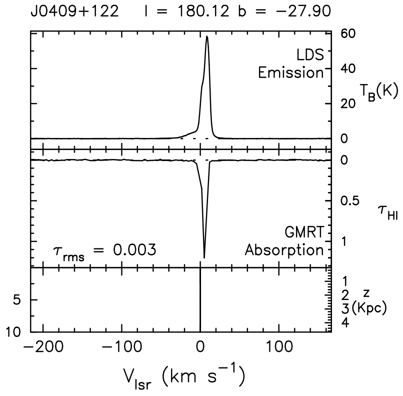
J0409+122 l = 180.12 b = −27.90
T_B(K)
LDS Emission
τ_{HI}
GMRT Absorption
τ_{rms} = 0.003
z (Kpc)
−200 −100 0 100
V_{lsr} (km s^{-1})

J0410+769 l = 133.41 b = +18.33

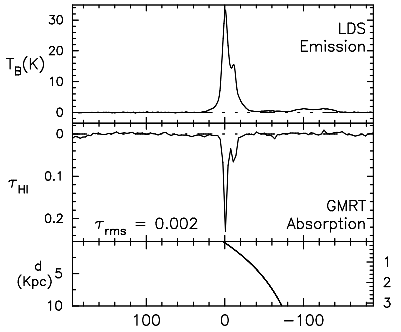

J0424+020 l = 192.04 b = −31.10

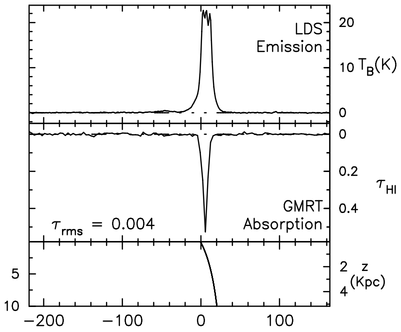

J0431+206 l = 176.81 b = −18.56

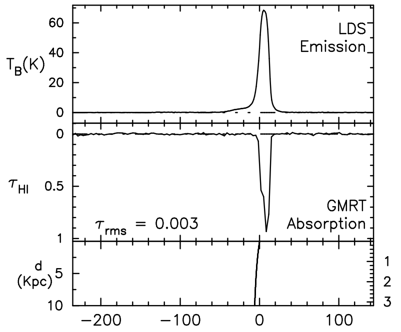

J0440−435 l = 248.41 b = −41.57

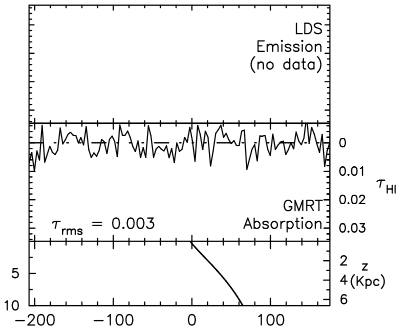

J0453−281 l = 229.09 b = −37.02

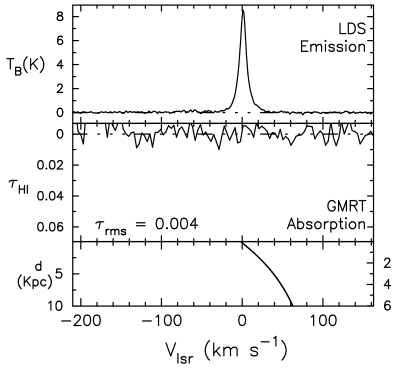

J0459+024 l = 197.01 b = −23.34

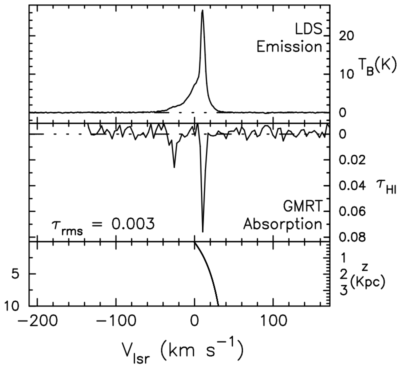

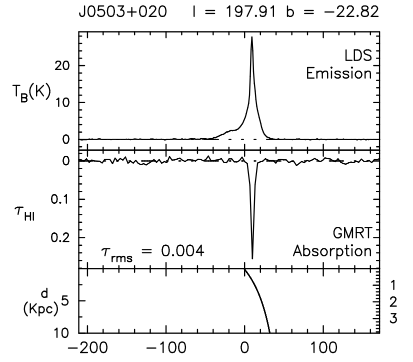
J0503+020 l = 197.91 b = −22.82
LDS Emission
T_B(K)
0
10
20
GMRT Absorption
τ_{HI}
0
0.1
0.2
τ_{rms} = 0.004
d (Kpc)
5
10
1
2
3
−200
−100
0
100

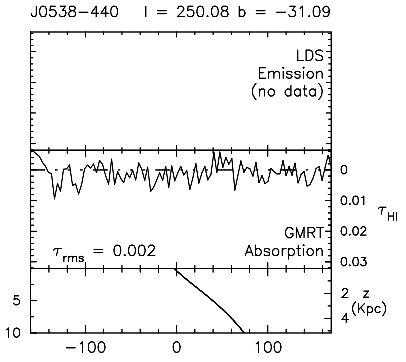
J0538−440 l = 250.08 b = −31.09
LDS Emission (no data)
GMRT Absorption
τ_{HI}
0
0.01
0.02
0.03
τ_{rms} = 0.002
5
10
2
4
z (Kpc)
−100
0
100

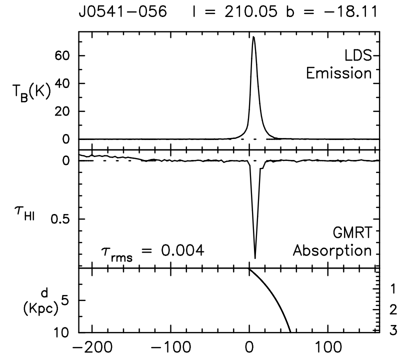
J0541−056 l = 210.05 b = −18.11
LDS Emission
T_B(K)
0
20
40
60
GMRT Absorption
τ_{HI}
0
0.5
τ_{rms} = 0.004
d (Kpc)
5
10
1
2
3
−200
−100
0
100

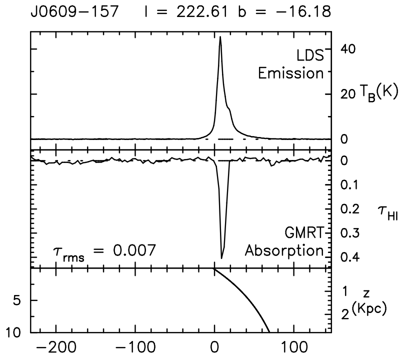
J0609−157 l = 222.61 b = −16.18
LDS Emission
T_B(K)
0
20
40
GMRT Absorption
τ_{HI}
0
0.1
0.2
0.3
0.4
τ_{rms} = 0.007
5
10
1
2
z (Kpc)
−200
−100
0
100

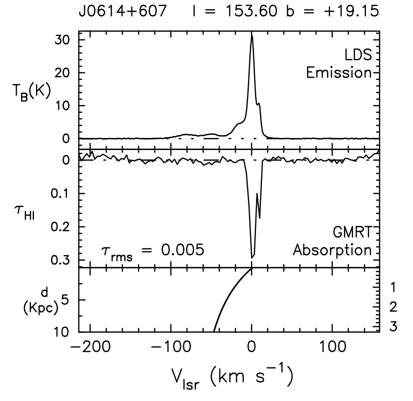
J0614+607 l = 153.60 b = +19.15
LDS Emission
T_B(K)
0
10
20
30
GMRT Absorption
τ_{HI}
0
0.1
0.2
0.3
τ_{rms} = 0.005
d (Kpc)
5
10
1
2
3
−200
−100
0
100
V_{lsr} (km s^{-1})

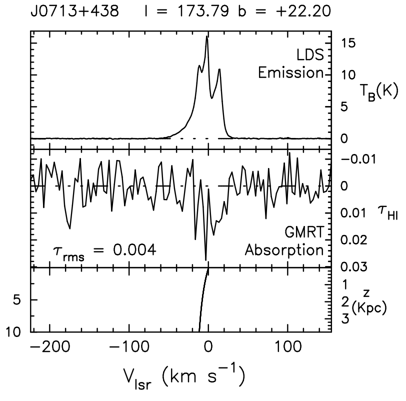
J0713+438 l = 173.79 b = +22.20
LDS Emission
T_B(K)
0
5
10
15
GMRT Absorption
τ_{HI}
−0.01
0
0.01
0.02
0.03
τ_{rms} = 0.004
5
10
1
2
3
z (Kpc)
−200
−100
0
100
V_{lsr} (km s^{-1})

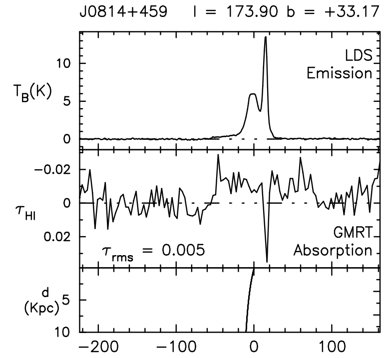
J0814+459 l = 173.90 b = +33.17
T_B(K)
LDS Emission
τ_HI
GMRT Absorption
τ_rms = 0.005
d (Kpc)
−200 −100 0 100

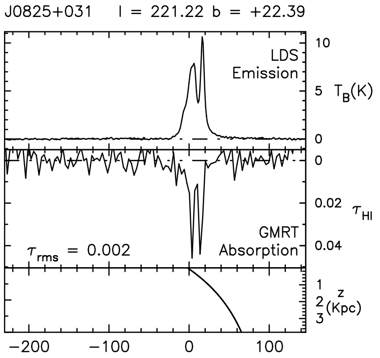
J0825+031 l = 221.22 b = +22.39
T_B(K)
LDS Emission
τ_HI
GMRT Absorption
τ_rms = 0.002
z (Kpc)
−200 −100 0 100

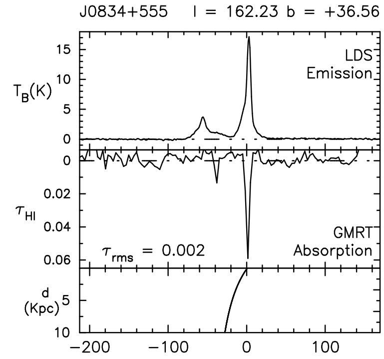
J0834+555 l = 162.23 b = +36.56
T_B(K)
LDS Emission
τ_HI
GMRT Absorption
τ_rms = 0.002
d (Kpc)
−200 −100 0 100

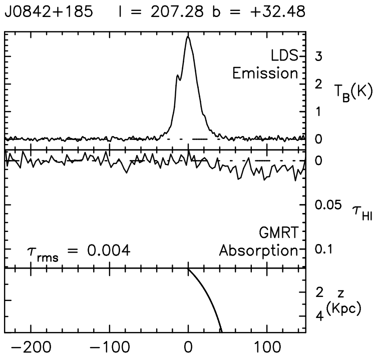
J0842+185 l = 207.28 b = +32.48
T_B(K)
LDS Emission
τ_HI
GMRT Absorption
τ_rms = 0.004
z (Kpc)
−200 −100 0 100

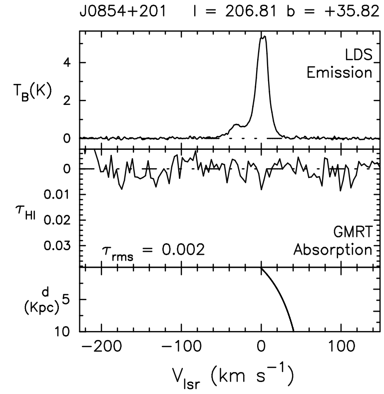
J0854+201 l = 206.81 b = +35.82
T_B(K)
LDS Emission
τ_HI
GMRT Absorption
τ_rms = 0.002
d (Kpc)
−200 −100 0 100
V_lsr (km s^−1)

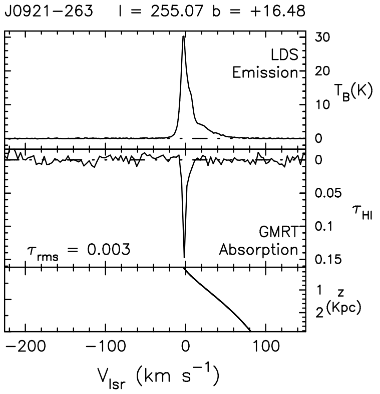
J0921−263 l = 255.07 b = +16.48
T_B(K)
LDS Emission
τ_HI
GMRT Absorption
τ_rms = 0.003
z (Kpc)
−200 −100 0 100
V_lsr (km s^−1)

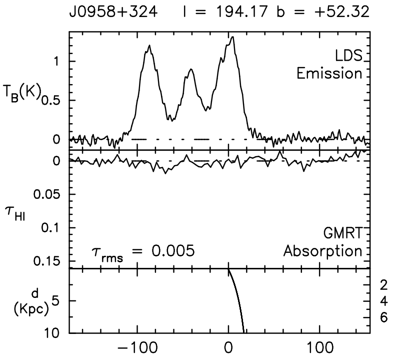
J0958+324 l = 194.17 b = +52.32
LDS Emission
$T_B(K)$
GMRT Absorption
τ_{HI}
τ_{rms} = 0.005
d (Kpc)
−100
0
100

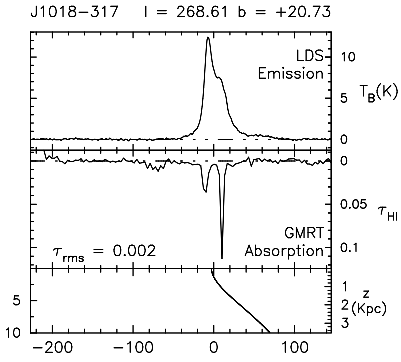
J1018−317 l = 268.61 b = +20.73
LDS Emission
$T_B(K)$
GMRT Absorption
τ_{HI}
τ_{rms} = 0.002
z (Kpc)
−200
−100
0
100

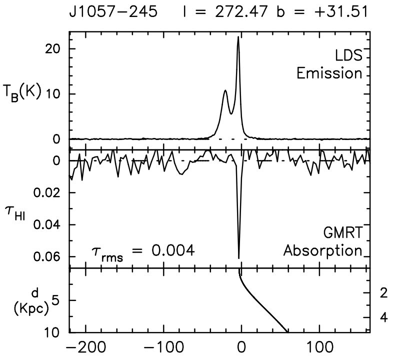
J1057−245 l = 272.47 b = +31.51
LDS Emission
$T_B(K)$
GMRT Absorption
τ_{HI}
τ_{rms} = 0.004
d (Kpc)
−200
−100
0
100

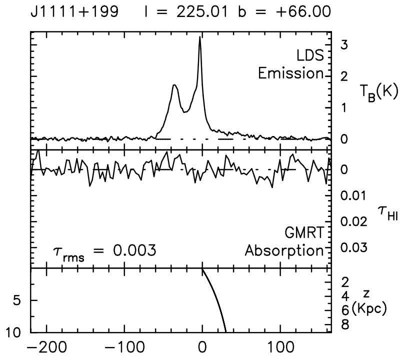
J1111+199 l = 225.01 b = +66.00
LDS Emission
$T_B(K)$
GMRT Absorption
τ_{HI}
τ_{rms} = 0.003
z (Kpc)
−200
−100
0
100

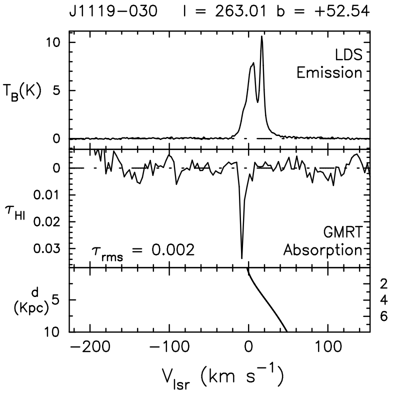
J1119−030 l = 263.01 b = +52.54
LDS Emission
$T_B(K)$
GMRT Absorption
τ_{HI}
τ_{rms} = 0.002
d (Kpc)
−200
−100
0
100
V_{lsr} (km s^{-1})

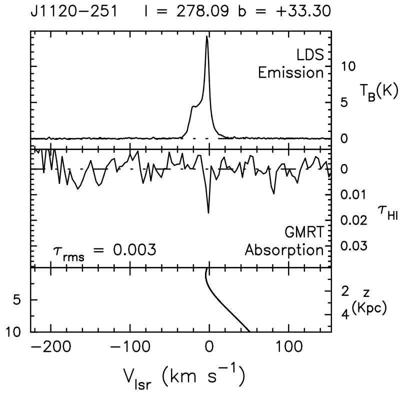
J1120−251 l = 278.09 b = +33.30
LDS Emission
$T_B(K)$
GMRT Absorption
τ_{HI}
τ_{rms} = 0.003
z (Kpc)
−200
−100
0
100
V_{lsr} (km s^{-1})

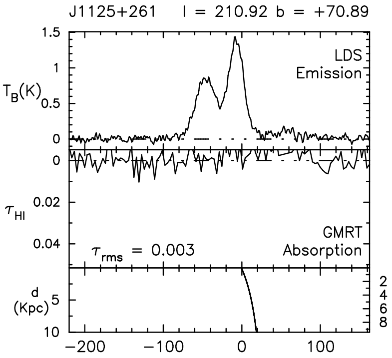
J1125+261 l = 210.92 b = +70.89
LDS Emission
T_B(K)
GMRT Absorption
τ_{HI}
τ_{rms} = 0.003
d (Kpc)
−200 −100 0 100

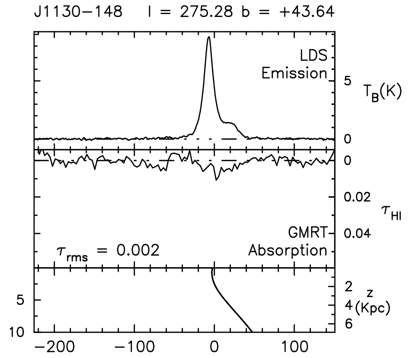
J1130−148 l = 275.28 b = +43.64
LDS Emission
T_B(K)
GMRT Absorption
τ_{HI}
τ_{rms} = 0.002
z (Kpc)
−200 −100 0 100

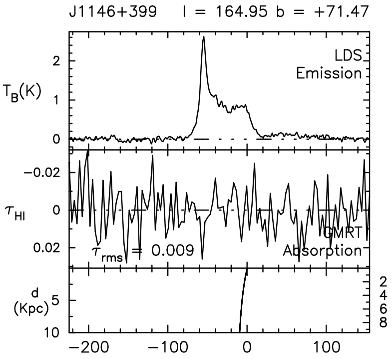
J1146+399 l = 164.95 b = +71.47
LDS Emission
T_B(K)
GMRT Absorption
τ_{HI}
τ_{rms} = 0.009
d (Kpc)
−200 −100 0 100

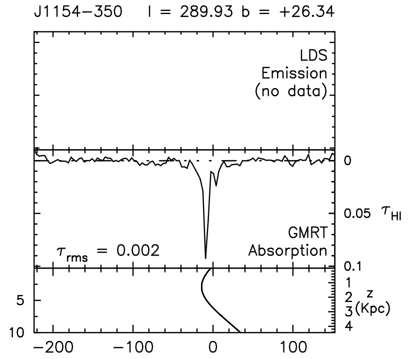
J1154−350 l = 289.93 b = +26.34
LDS Emission (no data)
GMRT Absorption
τ_{HI}
τ_{rms} = 0.002
z (Kpc)
−200 −100 0 100

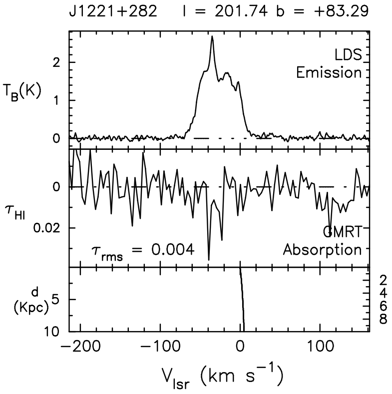
J1221+282 l = 201.74 b = +83.29
LDS Emission
T_B(K)
GMRT Absorption
τ_{HI}
τ_{rms} = 0.004
d (Kpc)
−200 −100 0 100
V_{lsr} (km s^{-1})

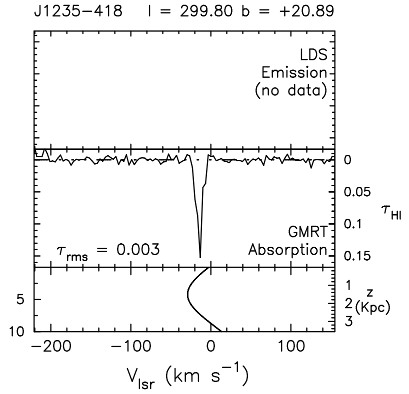
J1235−418 l = 299.80 b = +20.89
LDS Emission (no data)
GMRT Absorption
τ_{HI}
τ_{rms} = 0.003
z (Kpc)
−200 −100 0 100
V_{lsr} (km s^{-1})

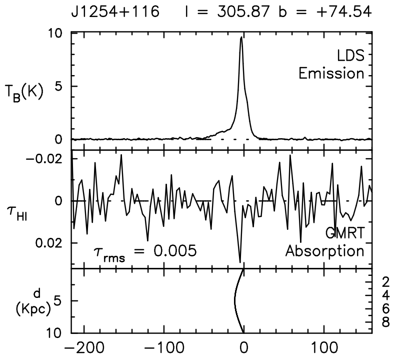
J1254+116 l = 305.87 b = +74.54
T_B(K)
10
5
0
LDS
Emission
τ_{HI}
−0.02
0
0.02
τ_{rms} = 0.005
GMRT
Absorption
d (Kpc)
5
10
2
4
6
8
−200
−100
0
100

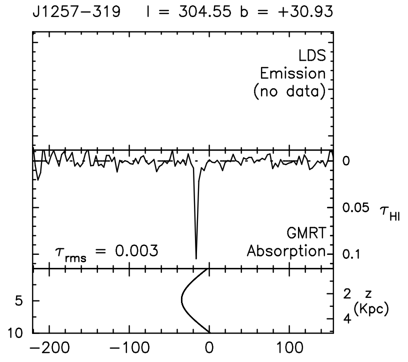
J1257−319 l = 304.55 b = +30.93
LDS
Emission
(no data)
0
0.05 τ_{HI}
0.1
τ_{rms} = 0.003
GMRT
Absorption
5
10
2 z
4 (Kpc)
−200
−100
0
100

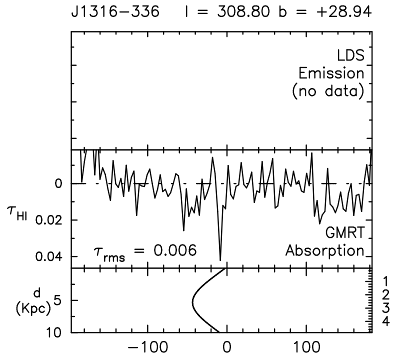
J1316−336 l = 308.80 b = +28.94
LDS
Emission
(no data)
τ_{HI}
0
0.02
0.04
τ_{rms} = 0.006
GMRT
Absorption
d (Kpc)
5
10
1
2
3
4
−100
0
100

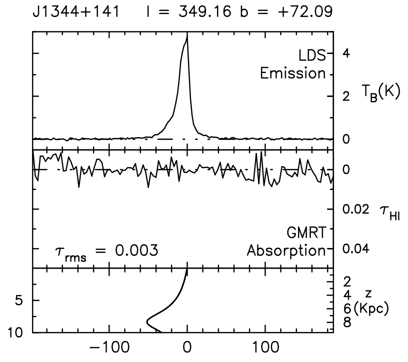
J1344+141 l = 349.16 b = +72.09
LDS
Emission
4
2 T_B(K)
0
0
0.02 τ_{HI}
0.04
τ_{rms} = 0.003
GMRT
Absorption
5
10
2
4 z
6 (Kpc)
8
−100
0
100

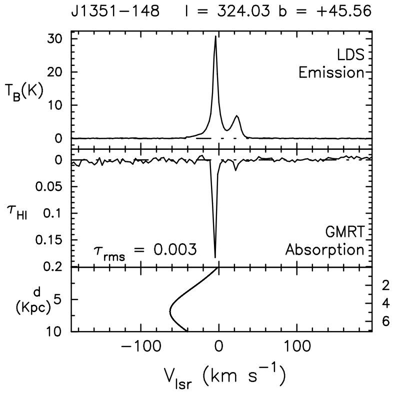
J1351−148 l = 324.03 b = +45.56
T_B(K)
30
20
10
0
LDS
Emission
τ_{HI}
0
0.05
0.1
0.15
0.2
τ_{rms} = 0.003
GMRT
Absorption
d (Kpc)
5
10
2
4
6
−100
0
100
V_{lsr} (km s^{-1})

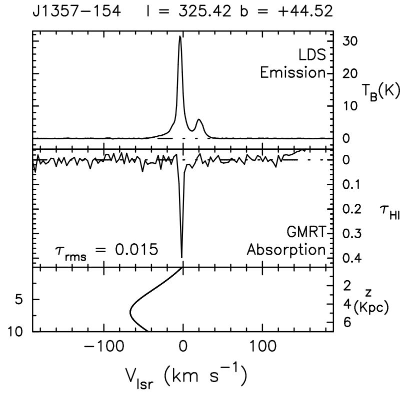
J1357−154 l = 325.42 b = +44.52
LDS
Emission
30
20
10 T_B(K)
0
0
0.1
0.2 τ_{HI}
0.3
0.4
τ_{rms} = 0.015
GMRT
Absorption
5
10
2 z
4 (Kpc)
6
−100
0
100
V_{lsr} (km s^{-1})

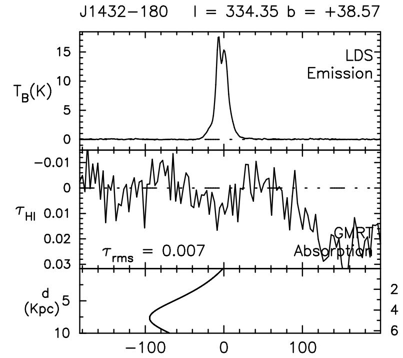
J1432−180 l = 334.35 b = +38.57
LDS
Emission
T_B(K)
GMRT
Absorption
τ_{HI}
τ_{rms} = 0.007
d (Kpc)
−100
0
100

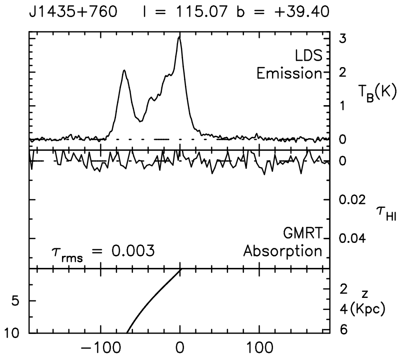
J1435+760 l = 115.07 b = +39.40
LDS
Emission
T_B(K)
GMRT
Absorption
τ_{HI}
τ_{rms} = 0.003
z (Kpc)
−100
0
100

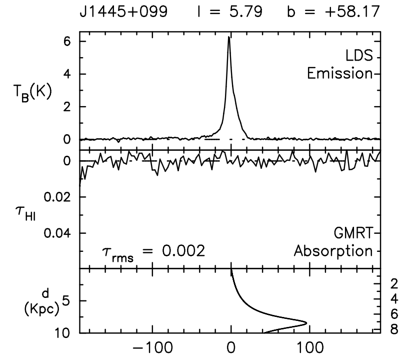
J1445+099 l = 5.79 b = +58.17
LDS
Emission
T_B(K)
GMRT
Absorption
τ_{HI}
τ_{rms} = 0.002
d (Kpc)
−100
0
100

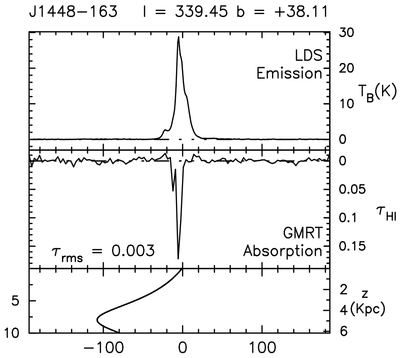
J1448−163 l = 339.45 b = +38.11
LDS
Emission
T_B(K)
GMRT
Absorption
τ_{HI}
τ_{rms} = 0.003
z (Kpc)
−100
0
100

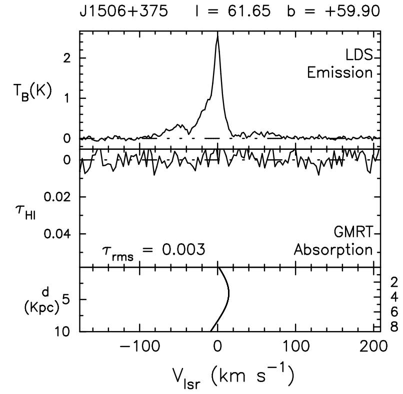
J1506+375 l = 61.65 b = +59.90
LDS
Emission
T_B(K)
GMRT
Absorption
τ_{HI}
τ_{rms} = 0.003
d (Kpc)
−100
0
100
200
V_{lsr} (km s^{-1})

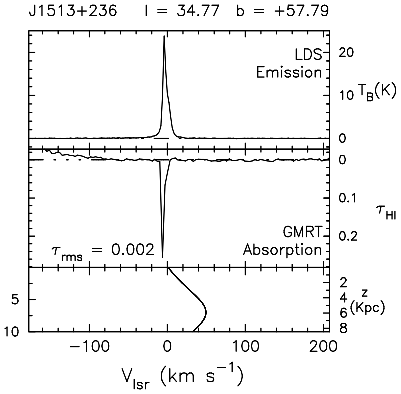
J1513+236 l = 34.77 b = +57.79
LDS
Emission
T_B(K)
GMRT
Absorption
τ_{HI}
τ_{rms} = 0.002
z (Kpc)
−100
0
100
200
V_{lsr} (km s^{-1})

J1517−243 l = 340.68 b = +27.58

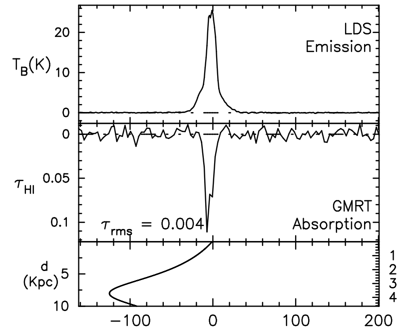

J1520+202 l = 29.64 b = +55.42

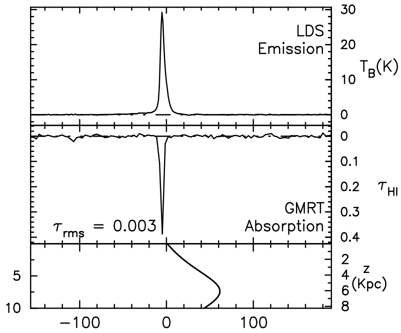

J1526−138 l = 350.48 b = +34.29

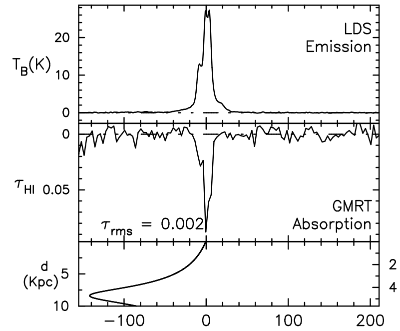

J1553+129 l = 23.79 b = +45.22

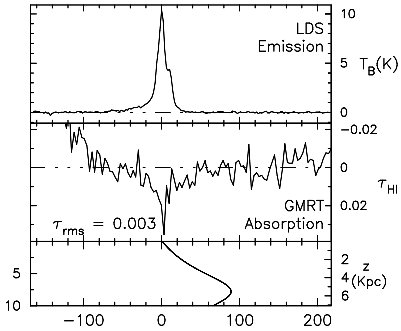

J1554−270 l = 345.68 b = +20.27

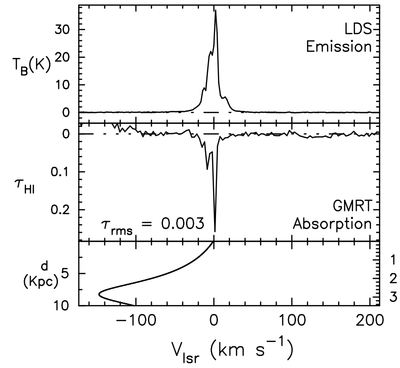

J1557−000 l = 9.58 b = +37.68

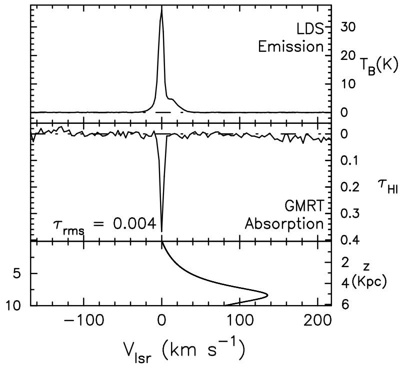

J1602+334 l = 53.73 b = +48.71

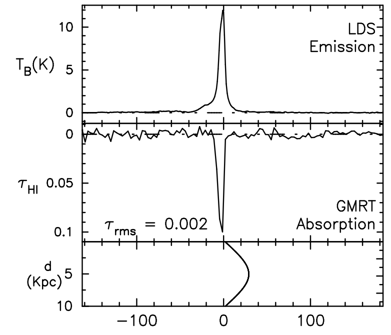

J1609+266 l = 44.17 b = +46.20

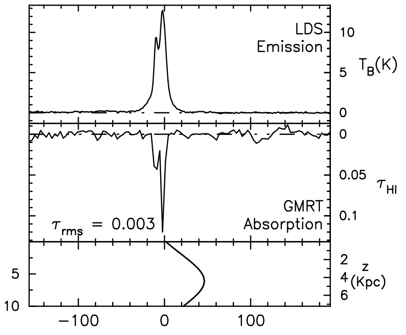

J1613+342 l = 55.15 b = +46.38

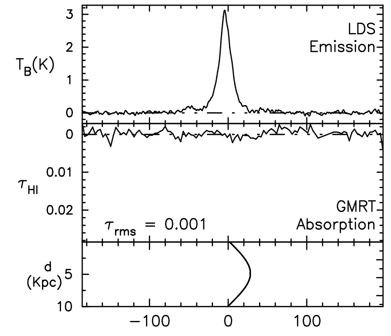

J1634+627 l = 93.61 b = +39.38

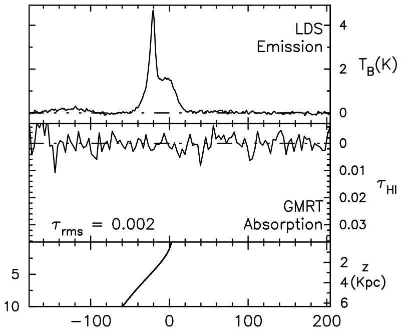

J1635+381 l = 61.09 b = +42.34

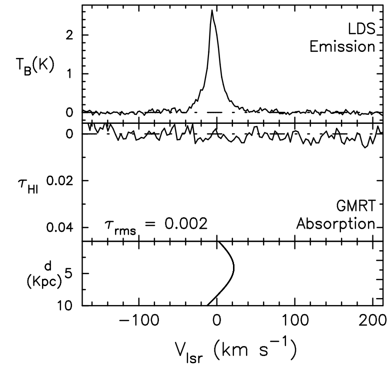

J1638+625 l = 93.22 b = +39.01

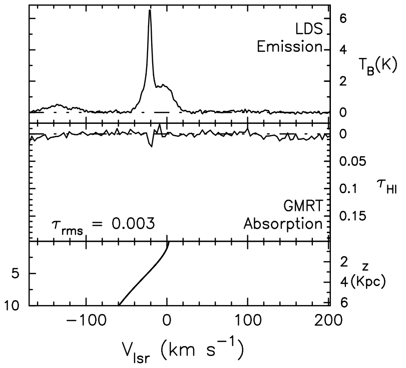

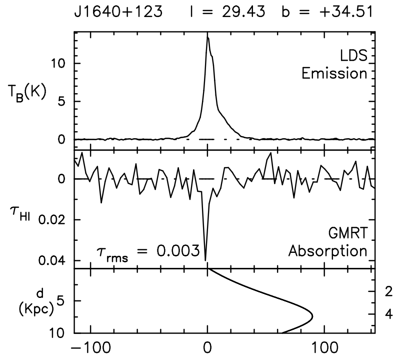
J1640+123 l = 29.43 b = +34.51
T_B(K)
LDS Emission
τ_{HI}
GMRT Absorption
τ_{rms} = 0.003
d (Kpc)
−100
0
100

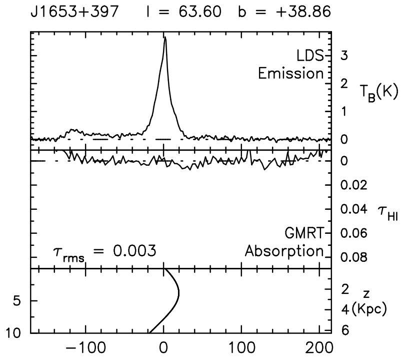
J1653+397 l = 63.60 b = +38.86
LDS Emission
T_B(K)
GMRT Absorption
τ_{HI}
τ_{rms} = 0.003
z (Kpc)
−100
0
100
200

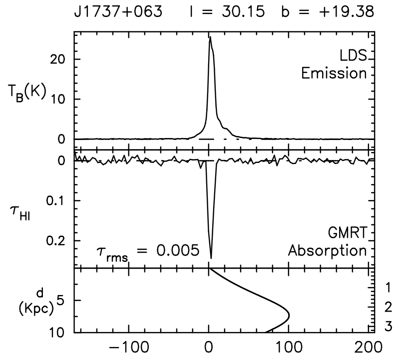
J1737+063 l = 30.15 b = +19.38
T_B(K)
LDS Emission
τ_{HI}
GMRT Absorption
τ_{rms} = 0.005
d (Kpc)
−100
0
100
200

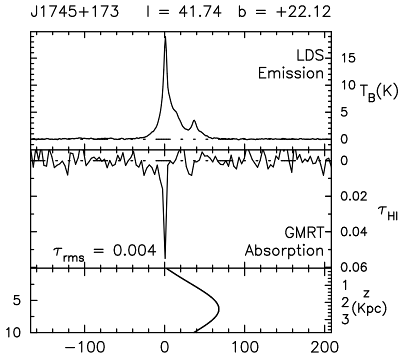
J1745+173 l = 41.74 b = +22.12
LDS Emission
T_B(K)
GMRT Absorption
τ_{HI}
τ_{rms} = 0.004
z (Kpc)
−100
0
100
200

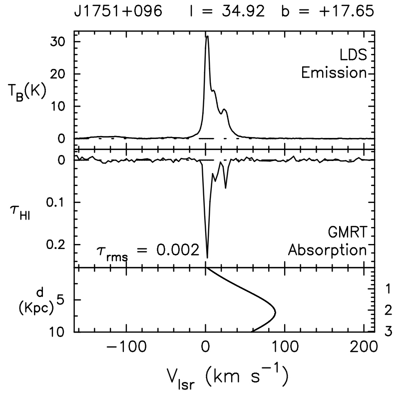
J1751+096 l = 34.92 b = +17.65
T_B(K)
LDS Emission
τ_{HI}
GMRT Absorption
τ_{rms} = 0.002
d (Kpc)
−100
0
100
200
V_{lsr} (km s^{-1})

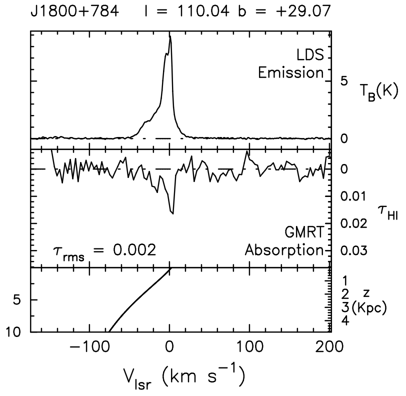
J1800+784 l = 110.04 b = +29.07
LDS Emission
T_B(K)
GMRT Absorption
τ_{HI}
τ_{rms} = 0.002
z (Kpc)
−100
0
100
200
V_{lsr} (km s^{-1})

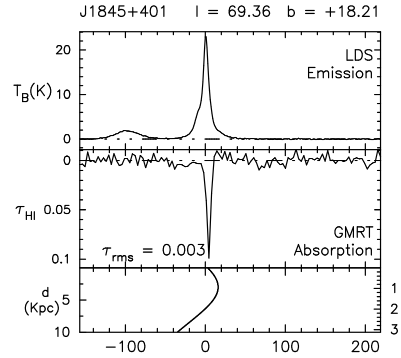
J1845+401 l = 69.36 b = +18.21
LDS
Emission
T_B(K)
GMRT
Absorption
τ_{HI}
τ_{rms} = 0.003
d (Kpc)
0
20
10
0.05
0.1
5
1
2
3
−100
0
100
200

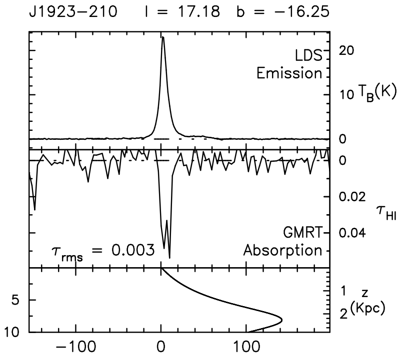
J1923−210 l = 17.18 b = −16.25
LDS
Emission
T_B(K)
GMRT
Absorption
τ_{HI}
τ_{rms} = 0.003
z (Kpc)
20
10
0
0.02
0.04
1
2
5
10
−100
0
100

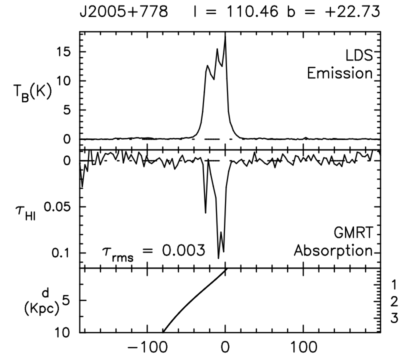
J2005+778 l = 110.46 b = +22.73
LDS
Emission
T_B(K)
GMRT
Absorption
τ_{HI}
τ_{rms} = 0.003
d (Kpc)
15
10
5
0
0.05
0.1
1
2
3
−100
0
100

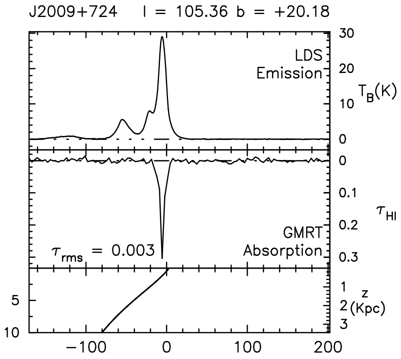
J2009+724 l = 105.36 b = +20.18
LDS
Emission
T_B(K)
GMRT
Absorption
τ_{HI}
τ_{rms} = 0.003
z (Kpc)
30
20
10
0
0.1
0.2
0.3
1
2
3
5
10
−100
0
100
200

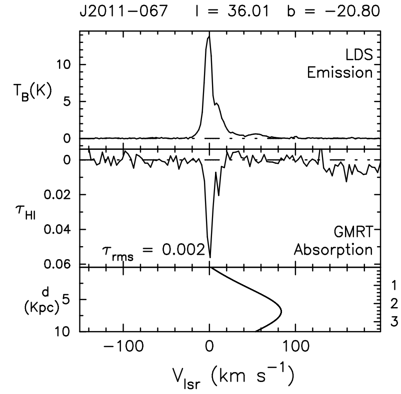
J2011−067 l = 36.01 b = −20.80
LDS
Emission
T_B(K)
GMRT
Absorption
τ_{HI}
τ_{rms} = 0.002
d (Kpc)
10
5
0
0.02
0.04
0.06
1
2
3
−100
0
100
V_{lsr} (km s^{-1})

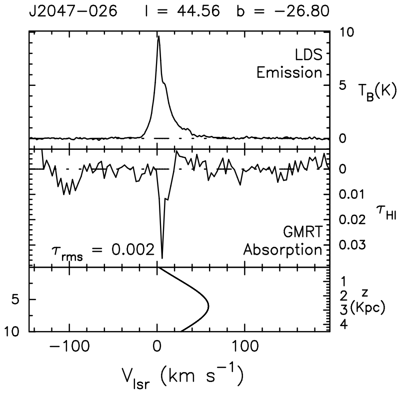
J2047−026 l = 44.56 b = −26.80
LDS
Emission
T_B(K)
GMRT
Absorption
τ_{HI}
τ_{rms} = 0.002
z (Kpc)
10
5
0
0.01
0.02
0.03
1
2
3
4
−100
0
100
V_{lsr} (km s^{-1})

J2130+050 l = 58.65 b = −31.81

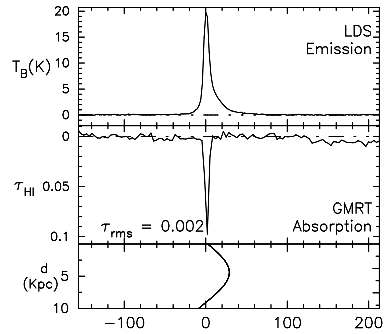

J2136+006 l = 55.47 b = −35.58

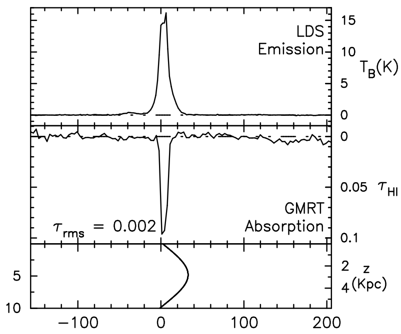

J2137−207 l = 30.35 b = −45.56

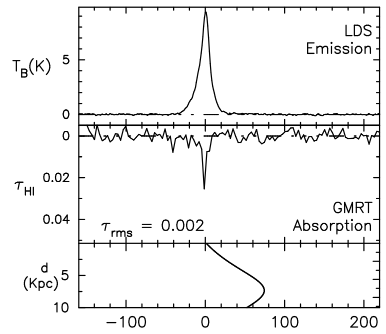

J2148+069 l = 63.66 b = −34.07

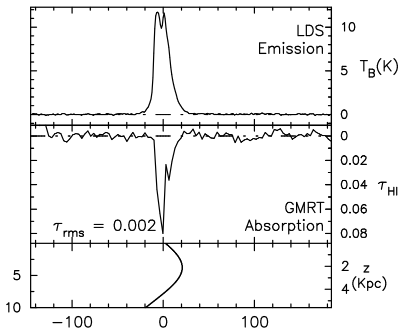

J2212+018 l = 63.68 b = −42.02

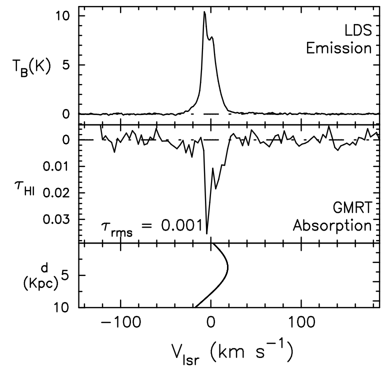

J2214−385 l = 3.47 b = −55.44

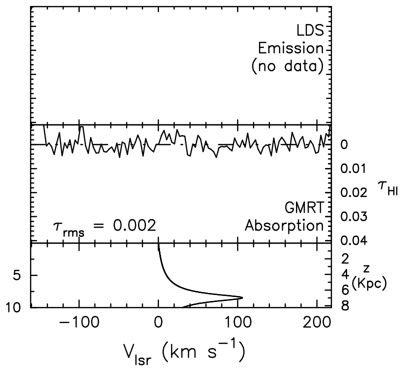

J2219−279 l = 22.57 b = −56.48

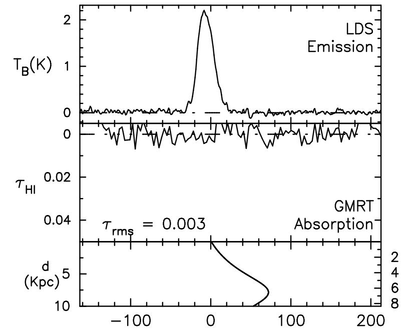

J2225−049 l = 58.96 b = −48.84

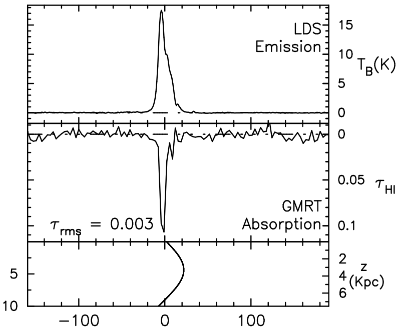

J2232+117 l = 77.44 b = −38.58

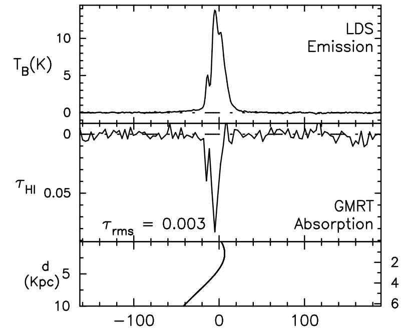

J2236+284 l = 90.12 b = −25.65

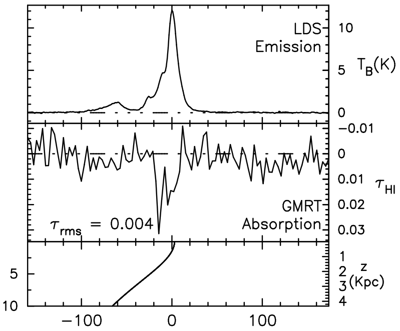

J2246−121 l = 53.87 b = −57.07

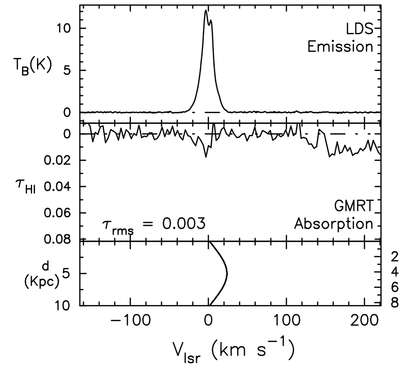

J2250+143 l = 83.89 b = −39.20

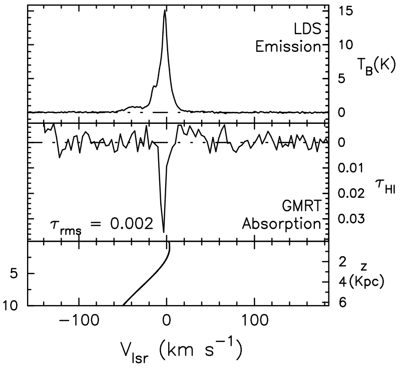

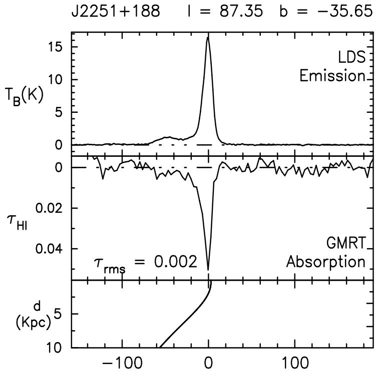
J2251+188 l = 87.35 b = −35.65
LDS
Emission
T_B(K)
15
10
5
0
τ_{HI}
0
0.02
0.04
GMRT
Absorption
τ_{rms} = 0.002
d
(Kpc)
5
10
2
4
−100
0
100

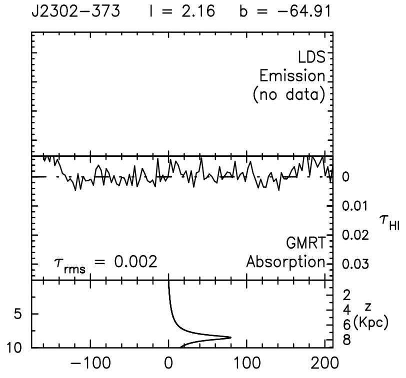
J2302−373 l = 2.16 b = −64.91
LDS
Emission
(no data)
0
0.01
0.02
0.03
τ_{HI}
GMRT
Absorption
τ_{rms} = 0.002
5
10
2
4
6
8
z
(Kpc)
−100
0
100
200

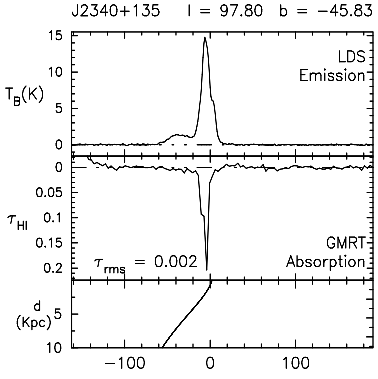
J2340+135 l = 97.80 b = −45.83
LDS
Emission
T_B(K)
15
10
5
0
τ_{HI}
0
0.05
0.1
0.15
0.2
GMRT
Absorption
τ_{rms} = 0.002
d
(Kpc)
5
10
2
4
6
−100
0
100

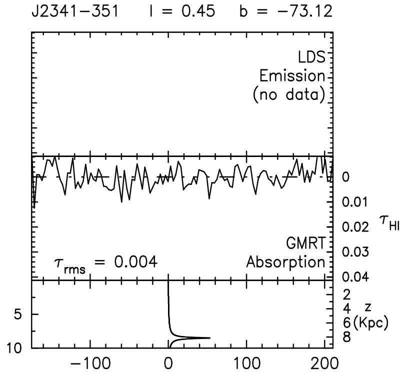
J2341−351 l = 0.45 b = −73.12
LDS
Emission
(no data)
0
0.01
0.02
0.03
0.04
τ_{HI}
GMRT
Absorption
τ_{rms} = 0.004
5
10
2
4
6
8
z
(Kpc)
−100
0
100
200

Appendix B: The Gaussian Components

In this Appendix, we list the discrete HI features identified from the high latitude Galactic HI absorption survey using the GMRT. In the following table, the first column lists the number corresponding to the background source (As per Table 3.2), towards which the absorption was measured using the GMRT. Columns 2, 3 and 4 list the peak optical depth, the mean LSR velocity and the FWHM respectively of discrete components identified using the gaussian fitting. The value of FWHM is deconvolved for a channel width of 3.26 km s^{-1}. The unresolved lines are marked with a "–" . Columns 5, 6 and 7 list the same for the HI emission profile along the same line of sight, obtained from the Leiden-Dwingeloo survey of Galactic neutral hydrogen (Hartman & Burton, 1995) The formal 1σ errors estimated in the last digit of the fitted parameters are given within brackets. An HI emission component with a similar central velocity (within the velocity range corresponding to the channel width, $\sim$3.3 km s^{-1}) and comparable width as the absorption component are assumed to arise from the same cloud. Column 8 lists the spin temperature, calculated using the absorption and emission data.

	HI Absorption (GMRT)			**HI Emission** (LDS)			
No.	$\tau_{\rm HI}$	$V_{\rm lsr}$ (km s^{-1})	FWHM (km s^{-1})	T_B (K)	$V_{\rm lsr}$ (km s^{-1})	FWHM (km s^{-1})	T_S (K)
1.		HI absorption was not detected			No data		
2.		HI absorption was not detected		2.5(2)	–1.1(2)	6.2(4)	>278
				3.8(2)	–2.2(2)	17.4(4)	>422
				3.4(9)	–5.89(6)	3.8(3)	∼340
				2.3(6)	–8(1)	7(1)	>256
				0.40(3)	–17(1)	47(2)	>44
3.		HI absorption was not detected			No data		

	HI Absorption (GMRT)			**HI Emission** (LDS)			
No.	$\tau_{\rm HI}$	$V_{\rm lsr}$ (km s^{-1})	FWHM (km s^{-1})	$T_{\rm B}$ (K)	$V_{\rm lsr}$ (km s^{-1})	FWHM (km s^{-1})	$T_{\rm S}$ (K)
4.	HI absorption was not detected			2.8(1)	–5.21(8)	13.3(3)	>311
				1.1(1)	–8.7(5)	28(1)	>122
				0.31(1)	–74(1)	55(3)	>34
5.				8.27(7)	+2.7(1)	10.9(2)	>827
	0.193(5)	–2.02(6)	3.3(2)	16.1(2)	–3.68(1)	5.11(5)	29
				2.58(7)	–12.68(5)	4.5(1)	>430
				1.23(3)	–20.2(8)	55(1)	>205
				1.35(4)	–39.8(2)	14.1(6)	>225
6.	0.09(1)	–7.6(4)	–	3.59(9)	–7.50(3)	5.1(1)	42
				5.14(8)	–7.60(4)	14.9(2)	>428
				0.78(2)	–21.4(8)	51(1)	>65
				0.24(3)	–46.2(5)	9(1)	>20
7.				2.48(5)	–6.57(8)	15.1(3)	>276
	0.030	–5.79	–	2.32(5)	–7.15(3)	3.7(1)	78
				0.44(4)	–14(1)	38(2)	>49
				0.118(9)	–69(7)	127(11)	>13
8.	0.08(4)	+2.8(8)	–	8.0(2)	+2.81(1)	3.62(5)	104
				5.9(5)	–0.4(4)	12.5(3)	>656
	0.034(7)	–3(3)	7(5)	7.9(5)	–3.41(4)	6.0(1)	236
				5.7(1)	–14.6(2)	15.3(4)	>633
				0.93(7)	–29.9(7)	66(2)	>103
				0.40(4)	–46.6(6)	17(2)	>44
				0.17(2)	–86.6(7)	11(2)	>19
9.				2.99(9)	+2.46(3)	3.9(1)	>322
	0.037(5)	–2.6(5)	6(1)	0.6(2)	–3.3(2)	4.6(9)	17
				8.2(2)	–3.7(1)	17.5(2)	$\gtrsim$400
	0.020(4)	–13(1)	7(3)	1.7(2)	–13.1(2)	6.9(5)	86
				0.82(4)	–15.0(7)	49(1)	>91

	HI Absorption (GMRT)			**HI Emission** (LDS)			
No.	$\tau_{\rm HI}$	$V_{\rm lsr}$ (km s^{-1})	FWHM (km s^{-1})	$T_{\rm B}$ (K)	$V_{\rm lsr}$ (km s^{-1})	FWHM (km s^{-1})	$T_{\rm S}$ (K)
10.				4.8(1)	–0.37(6)	6.0(1)	>533
				4.0(3)	–5.0(1)	18.4(3)	>444
	0.057(4)	–6.8(3)	9(7)	14.0(3)	–7.61(5)	8.4(2)	253
				1.7(2)	–12.21(6)	4.0(3)	>189
				0.31(1)	–48.7(4)	23(1)	>34
				0.104(9)	–111(2)	45(4)	>12
11.	0.054(6)	0.0(3)	5(1)	8.90(4)	+2.05(1)	4.43(3)	169
				3.81(5)	–4.47(8)	18.4(1)	>423
				1.91(5)	–9.73(6)	6.5(2)	>212
				0.136(9)	–20(2)	117(6)	>15
12.				7(1)	+4.5(9)	8.7(8)	>778
				14(2)	+3.25(7)	3.8(1)	>280
	0.347(7)	–2.12(5)	4.7(2)	21(2)	–0.01(9)	4.9(2)	72
				2.56(7)	–3.9(2)	27.8(4)	>284
	0.127(7)	–10.0(2)	3.5(3)	12.6(2)	–5.78(5)	5.28(7)	106
				0.16(1)	–10(3)	140(9)	>18
13.				17.1(1)	–0.38(2)	15.46(6)	>1425
	0.122(8)	–2.8(1)	4.7(4)	10.6(1)	–1.49(1)	5.52(5)	92
				0.14(1)	–22(5)	115(10)	>12
14.	0.04(1)	+1.4(5)	4(1)	1.83(6)	–1.13(4)	5.01(1)	47
				2.1(1)	–5.2(2)	21.4(4)	>233
				4.9(1)	–10.51(3)	9.5(1)	>544
				0.152(7)	–33(2)	124(5)	>17
15.	0.095(8)	+7.5(2)	4.0(7)	2.7(1)	+7.86(6)	3.7(2)	30
				23.9(3)	+1.49(2)	13.06(8)	>3983
	0.404(5)	+0.23(4)	4.6(1)	14.9(3)	–0.17(2)	5.63(6)	45
				1.5(1)	–1.1(4)	31(1)	>250
				0.11(1)	–57(8)	85(17)	>18
16.	1.5(1)	+8.1(1)	6.2(1)	47(2)	+10.74(4)	6.71(7)	60
	0.39(5)	+2(1)	9(1)	44.4(6)	+4.5(1)	10.5(2)	137
				1.6(3)	+2.2(7)	30(3)	>267
				3.6(2)	–6.5(1)	4.4(3)	>600
				0.17(3)	–111(7)	80(16)	>28

	HI Absorption (GMRT)			**HI Emission** (LDS)			
No.	$\tau_{\rm HI}$	$V_{\rm lsr}$ (km s^{-1})	FWHM (km s^{-1})	$T_{\rm B}$ (K)	$V_{\rm lsr}$ (km s^{-1})	FWHM (km s^{-1})	$T_{\rm S}$ (K)
17.	0.21(2)	+9.2(2)	–	23.8(4)	+12.51(1)	4.22(4)	126
				10(2)	+6.4(6)	14.4(8)	$>$1111
	0.229(9)	+3.3(2)	5.5(4)	12.7(5)	+6.29(3)	4.33(8)	62
				17.9(7)	–4.65(8)	7.8(1)	$>$1989
				2(1)	–5(9)	21(7)	$>$222
	0.500(5)	–8.64(3)	4.62(6)	6.6(4)	–7.35(3)	3.9(1)	17
				0.176(8)	–57(4)	117(7)	$>$20
18.	0.25(2)	+3.3(2)	–	22.1(3)	+6.96(1)	4.12(4)	100
				25.7(5)	+4.57(3)	12.91(9)	$>$2855
	0.23(2)	–2.8(3)	3.7(8)	15.7(4)	+1.18(3)	6.04(8)	76
				1.24(2)	–14.9(6)	56(1)	$>$138
19.	2.62(1)	+6.698(8)	3.7(3)	33.7(4)	+8.36(4)	5.57(4)	36
				9.8(2)	+5.30(6)	15.3(2)	$>$817
				33.2(5)	+4.42(3)	4.96(3)	$>$36
				2.6(2)	–20.4(6)	48.2(8)	$>$217
20.				15.3(5)	+10.30(2)	3.29(5)	$\gtrsim$170
	1.33(2)	+7.69(2)	–	38.76(7)	+7.52(6)	6.22(7)	53
	0.07(2)	+7.1(5)	13(2)	3.5(2)	+7.5(1)	15.1(6)	52
				7.1(9)	+5.57(3)	2.7(1)	$\gtrsim$50
				1.2(3)	+1.5(2)	2.6(3)	$>$133
				2.73(6)	–18.81(3)	5.5(1)	$>$303
				3.0(1)	–19.1(6)	44.0(5)	$>$333
				2.2(1)	–19.8(2)	17.0(7)	$>$244
21.	0.305(5)	+7.61(6)	3.78(1)	13.8(1)	+7.61(7)	3.47(3)	52
				6.1(2)	+4.85(7)	21.6(3)	$>$508
				9.8(2)	+3.94(6)	9.3(1)	$>$817
				0.31(5)	–20(2)	99(7)	$>$26
				1.42(5)	–29.9(5)	25(2)	$>$118
				1.19(9)	–45.9(2)	11.3(6)	$>$99
22.				11.0(2)	+11.41(6)	3.4(1)	$\gtrsim$367
				28(1)	+8.9(1)	4.9(2)	$\gtrsim$50
	1.25(1)	+5.9(1)	3.5(2)	30.9(8)	+6.40(3)	9.68(4)	43
	0.22(2)	0.0(6)	5.6(7)	8.7(3)	+1.43(4)	3.97(7)	44
				0.14(2)	–21(4)	75(6)	$>$16

	HI Absorption (GMRT)			**HI Emission** (LDS)			
No.	$\tau_{\rm HI}$	$V_{\rm lsr}$ (km s^{-1})	FWHM (km s^{-1})	$T_{\rm B}$ (K)	$V_{\rm lsr}$ (km s^{-1})	FWHM (km s^{-1})	$T_{\rm S}$ (K)
23.				0.5(2)	+18(1)	13.2(4)	$>$56
				3.9(3)	+3.62(7)	3.3(1)	$\gtrsim$98
	0.230(3)	–0.88(5)	3.78(8)	17.4(8)	–0.40(2)	5.4(1)	85
				9.8(8)	–2.3(3)	11.6(7)	$\gtrsim$65
				8.2(4)	–7.0(6)	24.9(5)	$>$911
	0.069(3)	–11.5(2)	6.9(5)	6.6(2)	–11.85(4)	4.9(1)	99
				0.52(2)	–57.4(6)	34(2)	$>$58
				1.14(2)	–99.4(4)	23.5(9)	$>$127
				1.20(2)	–127.5(4)	24.7(8)	$>$133
24.				8.9(5)	+11.92(5)	3.8(1)	$\gtrsim$90
	0.523(5)	+5.63(3)	5.4(7)	12.4(8)	+7.96(9)	12.5(3)	30
				5.8(7)	+6.93(3)	3.1(2)	$\gtrsim$12
				4.4(2)	+3.7(2)	24.4(3)	$>$367
	0.5(3)	+2.2(9)	–	10.9(4)	+2.36(4)	4.36(7)	28
				0.37(1)	–46.3(6)	30(2)	$>$31
25.				8.4(7)	+11.92(2)	2.84(9)	$\gtrsim$14
	1.19(3)	+10.01(2)	–	27.1(6)	+9.47(5)	5.32(9)	39
				29(1)	+4.27(4)	14.5(2)	$>$3222
	0.70(1)	+3.61(4)	4.4(1)	34(1)	+4.09(4)	8.2(1)	68
				3.7(1)	–6.3(8)	41(1)	$>$411
				0.5(1)	–31.9(5)	16(2)	$>$56
				0.14(1)	–98(4)	74(9)	$>$16
26.	HI absorption was not detected				No data		
27.	HI absorption was not detected			3.3(1)	+1.19(7)	19.0(3)	$>$275
				5.1(1)	+1.14(3)	7.1(1)	$>$425
				0.11(1)	–25(5)	136(11)	$>$9
28.	0.080(5)	+11.1(2)	–	19.2(1)	+10.44(1)	5.40(4)	250
				7.1(4)	+6.7(1)	22.7(6)	$>$789
				1.9(2)	–12(3)	40(3)	$>$211
	0.026(4)	–25.6(5)	–	0.21(8)	–28(1)	6(3)	8

	HI Absorption (GMRT)			**HI Emission** (LDS)			
No.	$\tau_{\rm HI}$	V$_{\rm lsr}$ (km s^{-1})	FWHM (km s^{-1})	T$_{\rm B}$ (K)	V$_{\rm lsr}$ (km s^{-1})	FWHM (km s^{-1})	T$_{\rm S}$ (K)
29.				6.1(2)	+10.53(7)	6.0(1)	$>$508
				10.0(1)	+10.25(5)	18.0(1)	$>$833
	0.26(9)	+9.92(6)	–	12.0(2)	+9.03(1)	2.98(4)	52
				2.40(3)	–12.8(4)	31.6(8)	$>$200
				0.08(2)	–31(8)	131(18)	$>$7
30.	HI absorption was not detected				No data		
31.				37.8(1)	+4.19(4)	5.97(3)	$\gtrsim$95
	0.842(5)	+7.44(2)	6.06(5)	16(2)	+7.5(1)	6.1(2)	28
				12.6(2)	+8.23(3)	23.3(2)	$>$1050
				23(2)	+8.9(2)	9.6(2)	$>$
				0.48(4)	+9.9(8)	74(3)	$>$40
	0.069(7)	+17.8(9)	–				
32.				6.7(2)	+3.10(2)	2.97(6)	$\gtrsim$95
				18.6(3)	+7.057(9)	3.71(4)	$\gtrsim$75
	0.432(9)	+10.51(8)	7.1(2)	20.3(4)	+8.37(5)	10.2(1)	58
				6.6(2)	+12.2(1)	26.6(6)	$>$314
				4.8(1)	+18.89(5)	5.9(1)	$>$229
				1.7(1)	+25.5(9)	52.5(8)	$>$81
33.	0.09(2)	+10.1(8)	–	7.96(5)	+9.40(1)	4.69(4)	88
				1.4(1)	+1.34(6)	2.5(2)	$>$93
	0.29(1)	+02.2(2)	10.7(6)	25.9(1)	+0.410(8)	7.72(2)	103
				5.17(4)	–7.1(1)	29.3(2)	$>$345
				0.68(5)	–18.6(2)	7.9(6)	$>$45
				1.30(2)	–49.1(2)	20.8(6)	$>$87
				1.21(2)	–79.9(3)	30.0(7)	$>$81
34.				3.1(2)	+14.57(3)	4.1(1)	$\gtrsim$238
				6.3(1)	+12.9(2)	11.0(3)	$\gtrsim$485
	0.015(3)	+5(3)	27(6)	6.5(3)	–1.57(2)	4.03(9)	433
				3.6(4)	–4.7(2)	9.3(3)	$\gtrsim$129
				7.5(2)	–6.6(4)	29.0(4)	$\gtrsim$625
				3.9(1)	–12.27(4)	5.5(1)	$>$325
				0.66(5)	–36(1)	22(1)	$>$55

	HI Absorption (GMRT)			**HI Emission** (LDS)			
No.	$\tau_{\rm HI}$	$V_{\rm lsr}$ (km s^{-1})	FWHM (km s^{-1})	T_B (K)	$V_{\rm lsr}$ (km s^{-1})	FWHM (km s^{-1})	T_S (K)
35.	0.035(2)	+16.8(9)	–	9.5(5)	+15.4(1)	3.8(1)	276
				3.4(2)	+12.8(3)	12.6(7)	$>$226
				4.0(6)	+12.6(2)	3.5(2)	$>$267
				1.1(2)	+2.9(1)	5.0(5)	$>$73
				5.38(7)	–2.9(2)	13.5(3)	$>$359
				0.64(3)	–12(1)	55(2)	$>$43
36.				0.24(2)	+27(3)	84(5)	$>$40
				1.6(2)	+19(1)	15(1)	$>$267
	0.034(7)	+14.8(6)	4(1)	8.6(2)	+16.70(2)	4.93(8)	257
	0.043(7)	+4.9(7)	–	6.4(6)	+5.3(1)	9.7(5)	152
				3.1(3)	–3 (1)	13(1)	$>$207
37.				0.111(8)	+61(10)	123(20)	$>$19
				0.7(2)	+13(3)	15(3)	$>$117
	0.059(3)	+1.4(2)	3.4(3)	12.7(1)	+3.005(9)	4.89(4)	222
				5.4(2)	–1.0(4)	14.8(5)	$>$900
	0.016(4)	–39(1)	–	0.97(6)	–40(2)	30(4)	61
				1.74(7)	–55.44(8)	5.9(2)	$>$290
				1.6(2)	–58.7(5)	17.9(9)	$>$267
38.	HI absorption was not detected			0.21(2)	+29(2)	21(4)	$>$18
				3.54(2)	+0.3(1)	25.5(3)	$>$295
				0.84(5)	–14.5(1)	4.4(3)	$>$70
39.	HI absorption was not detected			0.7(2)	+11(2)	11(2)	$>$117
				1.2(1)	+6.15(8)	4.8(3)	$>$200
				4.7(1)	+0.4(3)	14.1(3)	$>$783
				0.70(2)	–12.6(8)	49(1)	$>$117
				0.30(2)	–32.9(3)	10.0(9)	$>$50
40.	0.15(1)	–1.7(8)	–	19.1(4)	–1.77(8)	10.1(2)	137
				9.4(5)	–3.00(2)	4.3(1)	$\gtrsim$125
	0.022(6)	+5(4)	5(9)	6.1(2)	+6.78(9)	6.4(1)	280
				3.4(2)	+11.0(5)	31(1)	$>$378
				1.3(1)	+23(2)	55(1)	$>$144

	HI Absorption (GMRT)			**HI Emission** (LDS)			
No.	$\tau_{\rm HI}$	$V_{\rm lsr}$ (km s^{-1})	FWHM (km s^{-1})	T_B (K)	$V_{\rm lsr}$ (km s^{-1})	FWHM (km s^{-1})	T_S (K)
41.	HI absorption was not detected			1.27(1)	+0.2(1)	28.0(4)	>85
				0.83(1)	–41.9(2)	25.6(6)	>55
				1.16(1)	–86.4(1)	24.9(3)	>77
42.				0.66(6)	+24(3)	80(3)	>73
	0.109(6)	+13.5(1)	–	5.0(3)	+6.3(2)	20.6(6)	48
				2.3(3)	–1(1)	36(2)	>256
	0.035(3)	–7.0(3)	5.7(8)	8.4(1)	–7.36(4)	9.5(1)	240
43.	0.063(7)	–3.0(4)	–	14.2(2)	–4.118(8)	3.82(3)	233
				7.7(2)	–5.65(9)	10.2(2)	>642
				1.3(1)	–14.6(4)	41(2)	>108
				3.7(3)	–20.84(7)	6.9(3)	>308
				5.9(3)	–21.2(1)	14.4(4)	>492
44.	HI absorption was not detected			0.23(1)	+12(3)	96(4)	>26
				0.70(2)	–2.1(4)	6.4(8)	>78
				1.2(2)	–3.21(8)	3.3(2)	>133
				1.35(6)	–7.2(6)	19(1)	>150
				0.4(1)	–23(1)	10(3)	>44
				1.2(8)	–34.2(4)	12(3)	>133
				0.7(5)	–41(8)	19(6)	>78
45.	0.034(3)	–8.2(3)	3.7(4)	3.1(3)	–3(1)	14(1)	93
				6.4(6)	+5.3(1)	9.7(5)	>1067
				8.6(2)	+16.70(2)	4.93(8)	>1433
				1.6(2)	+19(1)	15(1)	>267
				0.24(2)	+27(3)	84(5)	>40
46.				0.11(1)	+16(5)	105(10)	>12
	0.020(4)	–2(1)	–	5(1)	–2.74(3)	4.2(2)	253
				4.9(9)	–2.77(4)	6.9(4)	>544
				4.95(4)	–9.3(1)	23.4(2)	>550
				1.85(6)	–21.47(7)	7.3(2)	>206
47.	HI absorption was not detected			0.088(6)	+51(3)	74(8)	>10
				1.36(1)	–7.2(1)	22.5(3)	>151
				0.857(9)	–45.6(2)	30.9(5)	>95

	HI Absorption (GMRT)			**HI Emission** (LDS)			
No.	$\tau_{\rm HI}$	$V_{\rm lsr}$ (km s^{-1})	FWHM (km s^{-1})	$T_{\rm B}$ (K)	$V_{\rm lsr}$ (km s^{-1})	FWHM (km s^{-1})	$T_{\rm S}$ (K)
48.				0.21(2)	–9(2)	103(6)	>35
	0.007(1)	+7(3)	37(6)	3.9(1)	–7.13(4)	8.9(2)	557
				4.7(1)	–6.72(8)	20.3(4)	>783
				1.22(2)	+20.1(2)	19.8(5)	>203
49.	HI absorption was not detected			0.110(7)	+55(3)	75(8)	>4
				0.82(2)	–7.2(3)	25.4(8)	>30
				1.11(1)	–43.0(4)	33.7(7)	>41
				1.77(3)	–55.11(5)	7.7(1)	>66
50.	0.022(3)	+3.7(4)	8(1)				
	0.092(4)	–8.3(1)	4.2(4)	No	Data		
	0.016(3)	–16(2)	13(5)				
51.				0.77(3)	–1.4(2)	9.0(5)	>64
	$\sim$0.01	–20	–	0.47(4)	–13.9(4)	11(1)	47
				1.52(3)	–26.3(7)	43.2(7)	>127
	$\sim$0.02	–38	–	1.06(4)	–34.8(1)	6.1(3)	53
				0.89(4)	–46.9(3)	16.0(9)	>74
52.	0.132(7)	–14.2(2)	8.1(5)	No	Data		
53.				3.1(3)	+2.4(4)	8.7(3)	>207
	0.03(1)	–5.9(8)	4(2)	6.3(6)	–3.49(3)	5.1(1)	213
				2.3(5)	–6(1)	10(1)	>153
				0.92(2)	–14.7(5)	41.3(8)	>61
				0.082(9)	–80(3)	48(8)	>5
54.	0.108(6)	–16.0(2)	–	No	Data		
55.	0.042(9)	–8.5(7)	4(1)	No	Data		
56.	HI absorption was not detected			1.40(5)	+00.40(5)	3.9(1)	>156
				3.20(6)	–03.9(1)	12.7(2)	>356
				0.14(3)	–08(2)	93(9)	>11
				1.1(1)	–10.7(4)	30(1)	>122

	HI Absorption (GMRT)			**HI Emission** (LDS)			
No.	$\tau_{\rm HI}$	$V_{\rm lsr}$ (km s^{-1})	FWHM (km s^{-1})	T_B (K)	$V_{\rm lsr}$ (km s^{-1})	FWHM (km s^{-1})	T_S (K)
57.	0.19(3)	–05.5(1)	3.4(1)	17.2(5)	–04.52(2)	4.4(1)	90
				10.9(5)	–04.4(1)	11.0(3)	>1211
				3.1(1)	–02.8(5)	41(1)	>344
	0.020(4)	+22.0(6)	4(1)	5.7(1)	+22.9(1)	10.5(2)	285
58.	0.40(2)	–2.1(2)	–	25.1(1)	–3.779(7)	5.75(3)	76
				6.6(5)	–2.6(2)	18.5(7)	>147
				5(2)	+20.2(3)	10.0(9)	>111
				1.2(3)	–18(5)	30(5)	>27
				0.9(1)	+26(12)	15(9)	>20
59.	HI absorption was			10.6(1)	–7.11(2)	5.36(5)	>505
	not detected			8.4(2)	+1.11(3)	8.1(1)	>400
				7.2(2)	–2.31(6)	23.7(2)	>343
60.	HI absorption was			0.08(1)	+9(10)	146(15)	>9
	not detected			1.51(3)	+0.42(8)	11.0(2)	>168
				1.82(2)	–12.3(3)	39.0(6)	>202
				0.60(4)	–38.5(5)	11(1)	>67
				0.26(3)	–51(1)	12(3)	>29
				1.94(2)	–69.8(1)	18.6(3)	>216
				0.08(1)	–137(2)	16(4)	>9
61.	HI absorption was			2.68(5)	+0.36(9)	17.3(3)	>447
	not detected			3.44(4)	–2.81(2)	5.14(7)	>573
				0.35(4)	–8(1)	46(3)	>58
62.	HI absorption was			0.29(3)	+10(2)	77(4)	>32
	not detected			3.1(2)	+6.03(4)	4.7(2)	>344
				11.3(5)	–1.63(5)	19.8(3)	>1256
	0.203(8)	–4.60(7)	–	12.1(4)	–3.37(4)	7.9(2)	66
	0.05(3)	–12(2)	–	8.9(1)	–6.00(1)	3.08(4)	182
				1.91(4)	–22.6(1)	6.7(2)	>212
63.	HI absorption was			0.28(2)	–53(1)	33(3)	>33
	not detected			0.98(3)	–07.1(5)	31(1)	>111
				1.64(4)	+00.2(1)	8.9(3)	>177
				0.13(1)	+57(2)	44(6)	>11

	HI Absorption (GMRT)			**HI Emission** (LDS)			
No.	τ_{HI}	$\mathrm{V_{lsr}}$ (km s^{-1})	FWHM (km s^{-1})	$\mathrm{T_B}$ (K)	$\mathrm{V_{lsr}}$ (km s^{-1})	FWHM (km s^{-1})	$\mathrm{T_S}$ (K)
64.	0.15(3)	00.0(1)	–	9.5(1)	–00.9(1)	9.2(1)	63
				1.1(1)	–03.4(4)	23(1)	$>$183
	0.26(5)	–05.73(5)	–	15.8(1)	–04.06(1)	3.23(2)	61
				0.22(2)	–19(4)	84(8)	$>$33
65.				13.2(6)	+2.3(2)	5.2(2)	$>$667
				6.2(1)	–1.1(2)	29.0(2)	$>$517
	0.071(5)	–1.1(3)	5.7(6)	14(1)	–1.3(1)	4.0(3)	204
	0.105(6)	–7.5(6)	3.8(3)	16(1)	–4.92(8)	3.9(3)	161
				5.8(9)	–8.3(3)	4.0(4)	$\gtrsim$73
				2.1(1)	–14.7(2)	10.0(1)	$>$175
66.				8.7(6)	–2.7(1)	6.9(2)	$\gtrsim$290
				3.7(4)	–2.78(9)	13.8(5)	$>$411
	0.409(7)	–5.28(5)	–	19.4(5)	–5.331(8)	3.83(4)	58
				0.49(2)	–17(1)	52(1)	$>$54
67.				1.32(4)	+18.6(1)	8.5(4)	$>$220
	0.073(9)	+4.4(3)	4.3(9)	15.6(3)	+4.07(1)	4.51(4)	222
				11.7(5)	0.0(1)	15.4(3)	$>$1950
	0.092(8)	–1.1(7)	–	13.3(5)	–0.76(2)	4.02(8)	151
				1.90(9)	–3.3(4)	44.5(9)	$>$317
				0.8(2)	–5.9(2)	2.3(5)	$>$133
	0.029(5)	–7(3)	9(5)	6.4(2)	–9.15(5)	4.8(1)	224
				0.16(1)	–82(2)	45(5)	$>$27
68.	0.010(1)	+6(4)	26(5)	3.1(1)	+11.0(2)	7.3(4)	312
	0.021(5)	+2.4(7)	5(3)	3.1(3)	+1.0(1)	4.6(4)	148
				6.8(3)	–0.7(2)	7.3(4)	$\gtrsim$340
				0.94(5)	–9(1)	51(2)	$>$104
69.				3.7(4)	+15.1(7)	9(1)	$>$411
	0.259(6)	+1.2(2)	–	28.5(9)	+2.68(4)	4.4(1)	125
				10.8(9)	–4.1(7)	21(1)	$>$1200
				11.1(9)	–4.2(1)	6.3(5)	$\gtrsim$222
				0.8(3)	–5(5)	73(17)	$>$89
	0.04(2)	–16(8)	8(5)				

	HI Absorption (GMRT)			**HI Emission** (LDS)			
No.	$\tau_{\rm HI}$	$V_{\rm lsr}$ (km s^{-1})	FWHM (km s^{-1})	$T_{\rm B}$ (K)	$V_{\rm lsr}$ (km s^{-1})	FWHM (km s^{-1})	$T_{\rm S}$ (K)
70.	0.371(8)	+0.34(7)	5.4(1)	28.0(3)	–1.19(4)	6.88(6)	90
				5.1(3)	+0.2(6)	22.6(5)	$>$425
				10.5(2)	+1.37(3)	2.6(2)	$\gtrsim$53
				1.3(4)	+13.8(3)	9(1)	$>$108
				1.8(3)	+19(2)	19(2)	$>$150
71.				7.5(2)	–0.03(3)	3.65(4)	$\gtrsim$70
				3.11(6)	–2.77(7)	16.0(2)	$>$518
	0.111(4)	–3.0(1)	5.6(3)	6.14(9)	–3.49(6)	4.51(8)	58
				0.143(7)	–19(2)	149(5)	$>$24
				0.66(2)	–21.1(2)	12.7(5)	$>$110
72.				0.11(2)	+43(1)	13(3)	$>$12
	0.123(5)	–1.7(2)	–	9.39(8)	–1.90(1)	7.79(5)	81
				3.36(8)	–5.42(8)	23.8(3)	$>$373
	0.056(9)	–10(2)	4(1)	5.86(6)	–9.99(2)	4.26(4)	108
				0.152(6)	–63(5)	133(10)	$>$17
73.	HI absorption was not detected			2.14(6)	–3.48(8)	19.9(4)	$>$713
				0.80(6)	–4.5(1)	7.4(5)	$>$267
				0.18(2)	–7(2)	83(5)	$>$60
				0.10(2)	–49.9(8)	9(2)	$>$33
74.	HI absorption was not detected			1.51(2)	–1.6(4)	22.2(7)	$>$252
				2.73(5)	–20.91(4)	6.1(1)	$>$455
				1.72(7)	–23.2(4)	19.4(5)	$>$287
				0.19(1)	–128(1)	44(3)	$>$32
75.	HI absorption was not detected			0.09(2)	+2(5)	105(15)	$>$15
				0.92(8)	–0.3(6)	7.7(9)	$>$153
				1.03(5)	–4.7(3)	29(1)	$>$172
				1.3(1)	–6.7(3)	6.4(5)	$>$217
76.				1.64(3)	–1.6(4)	22.6(7)	$>$182
	0.028(4)	–20.1(4)	4(1)	4.50(6)	–21.05(2)	5.05(7)	161
				1.97(7)	–23.1(3)	19.0(5)	$>$219
				0.40(1)	–133.0(7)	46(2)	$>$44

	HI Absorption (GMRT)			**HI Emission** (LDS)			
No.	$\tau_{\rm HI}$	$V_{\rm lsr}$ (km s^{-1})	FWHM (km s^{-1})	$T_{\rm B}$ (K)	$V_{\rm lsr}$ (km s^{-1})	FWHM (km s^{-1})	$T_{\rm S}$ (K)
77.	0.040(5)	–1.5(4)	–	3.7(5)	+0.13(4)	3.1(2)	94
				6.6(6)	+0.9(2)	8.1(2)	$\gtrsim$600
				3.1(4)	+4.7(1)	3.7(3)	$>$344
				3.76(5)	+5.49(9)	26.5(2)	$>$418
78.	HI absorption was not detected			1.22(4)	+2.17(6)	4.6(2)	$>$136
				2.33(3)	–0.19(8)	22.0(3)	$>$259
				0.19(1)	–14(3)	114(9)	$>$21
				0.12(2)	–87(2)	23(5)	$>$13
				0.32(2)	–115.1(8)	21(2)	$>$36
79.	0.258(7)	+2.63(9)	6.0(2)	19.8(1)	+1.62(3)	4.65(4)	87
				14.6(1)	+6.02(3)	4.41(5)	$\gtrsim$150
				4.69(6)	+6.8(1)	26.1(3)	$>$313
				0.59(5)	+20(2)	64(3)	$>$39
80.	0.060(8)	0.0(4)	–	11.2(1)	+0.80(1)	4.27(4)	192
				5.7(1)	+3.3(1)	20.2(4)	$>$475
				2.2(1)	+14.7(9)	48(1)	$>$183
				2.0(2)	+36.9(2)	6.0(4)	$>$167
				0.6(1)	+44(2)	12(3)	$>$50
81.	0.066(3)	+25.6(2)	3.3(2)	3.9(1)	+25.1(1)	7.1(3)	61
				0.32(8)	+25(7)	91(13)	$>$53
				7.5(2)	+13.1(2)	29.9(5)	$>$1250
	0.051(3)	+12.7(2)	6.2(6)	7.0(2)	+10.54(6)	7.4(3)	141
	0.235(3)	+2.02(5)	5.5(1)	27.6(1)	+1.91(2)	6.43(4)	132
				0.28(5)	–47(2)	22(6)	$>$47
				0.56(9)	–112(4)	28(6)	$>$93
				0.5(1)	–137(5)	26(6)	$>$83
82.	0.016(2)	+1.4(7)	9(2)	5.3(1)	+1.58(3)	4.23(6)	334
				4.41(6)	–4.04(7)	7.7(2)	$>$735
				3.04(6)	–6.3(3)	27.5(6)	$>$507
				0.98(5)	–30.3(5)	18.9(7)	$>$163

	HI Absorption (GMRT)			**HI Emission** (LDS)			
No.	$\tau_{\rm HI}$	$V_{\rm lsr}$ (km s^{-1})	FWHM (km s^{-1})	T_B (K)	$V_{\rm lsr}$ (km s^{-1})	FWHM (km s^{-1})	T_S (K)
83.	0.099(5)	+4.3(1)	4.6(3)	11.0(3)	+1.3(1)	10.4(1)	117
				2.93(7)	+1.3(1)	36.1(4)	$>$326
				9.5(3)	+0.36(2)	4.84(8)	$>$320
				3.2(1)	–9.0(2)	9.2(4)	$>$356
				1.81(1)	–97.4(1)	36.3(3)	$>$201
84.	0.053(7)	+2.5(6)	5(2)	10.2(2)	+2.24(5)	4.66(9)	192
				11.7(2)	+3.78(3)	12.7(2)	$\gtrsim$400
	0.055(8)	+9.7(6)	3.4(7)	1.9(2)	+5.7(1)	3.2(3)	35
				1.8(1)	+7.4(4)	35(1)	$\gtrsim$80
				0.58(2)	+47.4(6)	22(1)	$>$64
85.	0.07(2)	–3(1)	–	9.3(1)	0.07(2)	3.90(5)	138
	0.05(3)	–7(2)	16(3)	5.1(6)	–5.0(3)	11.5(7)	105
	0.08(3)	–8(3)	–	4.0(2)	–10.71(5)	3.3(1)	52
				8.8(7)	–11.8(1)	26.9(5)	$>$978
				0.11(2)	–17(9)	141(31)	$>$12
				1.8(4)	–17.6(2)	5.0(7)	$>$200
	0.05(1)	–25(4)	–	7.2(3)	–23.59(8)	7.4(2)	148
				0.18(2)	–113(2)	34(5)	$>$20
86.	0.20(2)	–5.2(1)	–	22.8(1)	–5.11(1)	9.54(5)	126
				7.0(1)	–10.1(2)	29.2(3)	$>$778
				3.4(1)	–22.23(8)	8.3(3)	$>$378
				3.9(2)	–52.9(2)	21.5(5)	$>$433
				1.7(2)	–55.1(1)	8.7(6)	$>$189
				0.83(2)	–123.6(4)	35(1)	$>$92
87.				0.57(2)	+53.6(7)	27(2)	$>$95
				0.40(4)	+30.6(6)	11(1)	$>$44
	0.020(3)	+11.1(6)	–	0.8(1)	+9.9(2)	4.9(8)	40
				4.4(2)	+4.4(1)	23.9(4)	$>$733
	0.058(1)	+0.1(2)	7.2(4)	5.9(3)	+1.25(4)	3.7(1)	105
				9.7(1)	–2.93(7)	6.5(1)	$\gtrsim$243

	HI Absorption (GMRT)			**HI Emission** (LDS)			
No.	τ_{HI}	V_{lsr} (km s^{-1})	FWHM (km s^{-1})	T_B (K)	V_{lsr} (km s^{-1})	FWHM (km s^{-1})	T_S (K)
88.				1.1(4)	–2(1)	5(1)	$>$183
	0.035(3)	+6(1)	4(2)	4.7(5)	+2.0(2)	4.4(2)	134
				4.2(3)	+3.9(0.2)	19(1)	$>$700
	0.012(4)	+13(3)	5(7)	0.8(1)	+9.4(3)	4.9(9)	67
				1.1(0.3)	+18(5)	33(5)	$>$183
				0.30(4)	+35.5(3)	4.7(8)	$>$50
				0.10(1)	+48(8)	50(5)	$>$17
89.	0.10(1)	+01.40(7)	3.8(1)	16.3(2)	+00.60(3)	6.7(1)	163
				4.1(2)	+06.1(4)	18.1(8)	$>$683
				1.3(2)	+14(2)	50(3)	$>$216
90.	0.14(2)	0(2)	–	8.6(1)	+00.8(4)	6.0(1)	61
	0.10(5)	+05.5(1)	4.7(4)	8.5(1)	+06.20(3)	4.0(1)	85
				6.9(1)	+04.80(6)	19.6(2)	$>$1150
				0.40(2)	–36.0(8)	23(2)	$>$67
91.	0.025(2)	–1.2(3)	3.8(5)	3.7(2)	+1.03(4)	7.1(1)	150
				3.6(1)	–0.6(1)	15.7(6)	$>$600
				2.4(2)	–3.7(2)	29.3(6)	$>$400
92.				7.8(1)	–7.62(4)	5.92(9)	$\sim$173
	0.079(3)	–2.1(2)	8.0(4)	6.7(3)	+0.63(9)	11.2(3)	88
				4.3(3)	+2.3(2)	23.6(5)	$>$717
	0.040(4)	+7.7(2)	–				
93.				0.08(1)	+35(8)	109(12)	$>$27
	0.016(1)	+7.0(9)	14(2)	4.5(1)	+0.32(8)	11.2(3)	284
				3.4(1)	–1.7(1)	24.2(4)	$>$1133
	0.037(4)	–3.6(2)	–	6.05(8)	–7.23(2)	4.64(6)	167
94.		HI absorption was not detected			No data		
95.		HI absorption was not detected		0.7(4)	–13.2(4)	11(2)	$>$78
				1.4(5)	–4(2)	18(4)	$>$156
				0.6(4)	–3.9(7)	32(4)	$>$67

	HI Absorption (GMRT)			**HI Emission** (LDS)			
No.	$\tau_{\rm HI}$	V$_{\rm lsr}$ (km s^{-1})	FWHM (km s^{-1})	T$_{\rm B}$ (K)	V$_{\rm lsr}$ (km s^{-1})	FWHM (km s^{-1})	T$_{\rm S}$ (K)
96.				0.15(2)	–10(3)	60(6)	$>$17
				9.2(2)	–5.24(9)	5.09(1)	$\gtrsim$95
				2.8(4)	–2.50(5)	2.8(2)	$\gtrsim$31
	0.124(4)	–2.4(1)	5.4(3)	10.15(7)	+0.15(7)	15.2(1)	87
	0.029(4)	+8(2)	–	1.25(8)	+8.77(6)	3.4(2)	44
				0.68(4)	+16.8(1)	4.8(4)	$>$76
97.				9.87(8)	+0.6(1)	14.1(2)	$>$1097
				0.77(5)	–3.4(0.6)	50(2)	$>$86
	0.079(3)	–4.6(2)	8.3(5)	7.4(2)	–5.81(2)	5.3(1)	94
	0.040(4)	–15.3(3)	–	3.83(7)	–13.88(3)	3.92(8)	96
98.				4(1)	+5(2)	14(2)	$>$333
	0.018(4)	–1(1)	12(4)	8(2)	–0.16(4)	8.7(4)	448
				0.6(1)	0(3)	51(4)	$>$50
	0.031(5)	–14.2(6)	5(1)	3.6(2)	–11.0(2)	10.1(3)	118
				1.5(1)	–24.3(2)	12.3(7)	$>$125
				0.64(5)	–61.0(3)	13.5(9)	$>$53
				0.61(4)	–68(2)	40(2)	$>$51
99.				4.36(6)	+3.84(3)	4.67(6)	$>$484
				7.33(9)	–1.31(3)	21.6(1)	$>$814
	0.016(3)	–2.9(9)	8(2)	4.93(8)	–3.46(3)	7.05(9)	308
100.	0.037(3)	–4.2(3)	5.0(6)	5.7(1)	–2.02(2)	4.06(7)	157
				8.6(1)	–2.52(3)	13.9(1)	$>$1433
				0.91(3)	–13.2(9)	53(2)	$>$152
				2.01(5)	–15.34(6)	5.2(2)	$>$335
				0.38(4)	–40.7(5)	13(2)	$>$63
101.	0.041(4)	–0.3(3)	7.3(9)	14.74(8)	–0.27(2)	10.51(6)	367
				1.88(8)	–7.5(4)	30.0(9)	$>$313
	0.015(3)	–9(3)	22(3)	1.47(8)	–8.6(1)	5.4(3)	99
102.		HI absorption was not detected			No data		

	HI Absorption (GMRT)			**HI Emission** (LDS)			
No.	$\tau_{\rm HI}$	$V_{\rm lsr}$ (km s^{-1})	FWHM (km s^{-1})	T_B (K)	$V_{\rm lsr}$ (km s^{-1})	FWHM (km s^{-1})	T_S (K)
103.				2.12(9)	+4.84(7)	4.4(2)	$>$353
				2.3(2)	–2.20(6)	3.0(2)	$\gtrsim$50
	0.216(5)	–4.60(7)	3.5(1)	9.1(2)	–4.58(7)	15.5(1)	47
	0.098(5)	–11(3)	–	5.8(1)	–6.27(5)	5.6(1)	62
				1.41(2)	–36.2(2)	27.9(5)	$>$235
104.		HI absorption was not detected			No data		